

TISSUE CHARACTERIZATION USING H-SCAN ULTRASOUND IMAGING

by

Haowei Tai

APPROVED BY SUPERVISORY COMMITTEE:

Kenneth Hoyt, Chair

John H.L. Hansen

Katherine Brown

Lakshman Tamil

Copyright 2022

Haowei Tai

All Rights Reserved

TISSUE CHARACTERIZATION USING H-SCAN ULTRASOUND IMAGING

by

HAOWEI TAI, BS, MS

DISSERTATION

Presented to the Faculty of
The University of Texas at Dallas
in Partial Fulfillment
of the Requirements
for the Degree of

DOCTOR OF PHILOSOPHY IN
ELECTRICAL ENGINEERING

THE UNIVERSITY OF TEXAS AT DALLAS

December 2022

ACKNOWLEDGMENTS

Firstly, I would like to thank my advisor, Dr. Kenneth Hoyt. Your ambition for research inspired me and will benefit me forever. Your willingness to explore and approach innovative projects in a critical manner, all while maintaining an easygoing view on life, gives me a better idea about how to be a good scientist. I have learned a lot from you since I first joined the lab. I am so grateful for the opportunities you provided me during my time as a student. I also appreciate the support of my committee members: Dr. Katherine Brown, Dr. John H.L. Hansen, and Dr. Lakshman Tamil. Thank you for the guidance and valuable suggestions aimed towards improving my scientific method. It is you all who make my research more convincing. I would also like to thank my knowledgeable and friendly lab mates; your support and help made my PhD journey more manageable. To my tissue characterization team: Swapnil Dolui and Dr. Mawia Khairalseed, I cannot count how many discussions we had during the past years, I gained tremendous knowledge from you two. And I also cannot definitively state how many times I went to Arvin Honari, Aditi Bellary, Kathy Brown, Hassan Jahanandish, and Chastity Chavez to ask for suggestions about my writing. I am appreciative of Frank Li, Shreya Reddy, Brian Trinh and Jane Song for preparing all of my animals and histology slices; your professional skill and help made my research way more straightforward. To my family: thank you for always supporting me, and it is your encouragement that made me go this far. A huge thanks to my wife, Wenjuan. I cannot imagine what would happen without you. And to my little girls, Hannah and Sarah, your singing and laughter will be with me and give me the power to overcome challenges.

October 2022

TISSUE CHARACTERIZATION USING H-SCAN ULTRASOUND IMAGING

Haowei Tai, PhD
The University of Texas at Dallas, 2022

Supervising Professor: Kenneth Hoyt, Chair

Breast cancer is the second leading cause of mortality among women and affects more women than any other type of cancer. Around 43,600 women in the U.S. died in 2021 from breast cancer. Clinical studies have demonstrated that an early neoadjuvant response is a better predictor of the patient's recurrence-free survival than pathological complete response. Therefore, mammography, ultrasound (US), and magnetic resonance imaging (MRI) have been widely used to determine tumor response by tracking changes in tumor size using guidelines provided by the Response Evaluation Criteria in Solid Tumors (RECIST). However, measurable changes in tumor size may not be detectable until after multiple cycles of chemotherapy. In the interim, high cost and unnecessary patient toxicity may be incurred for therapy regimens. Further, intratumor heterogeneity poses a fundamental treatment challenge because different tumor subregions might have different drug sensitivities. This implies that some therapeutic strategies might not be effective against the whole tumor. Therefore, the use of noninvasive US for quantitative tissue characterization has become an exciting research prospect. Herein the challenge is to find hidden patterns in the US data to reveal more information about tissue function and pathology that cannot be seen in the conventional US images. Circumventing some of the limitations associated with

traditional tissue characterization approaches, a new modality has been proposed for the US classification of acoustic scatterers, such as cancer cells. Termed H-scan US imaging, this technique relies on matching a model that describes US image formation to the mathematics of a class of Gaussian-weighted Hermite polynomials. In short, it reveals the local frequency dependence of different sized scatterers in soft tissue. In this dissertation work we demonstrate: (1) application of a novel frequency-dependent attenuation correction technique improves H-scan US imaging sensitivity to subtle changes at tissue depth. (2) propose 3-D H-scan imaging technique to capture data from the entire tumor burden, visualization of any heterogenous tissue patterns, and fundamentally improve any tissue characterization strategy and treatment response determination and (3) propose volumetric H-scan US imaging to visualize breast cancer changes during response to drug treatment including apoptotic activity, which is a hallmark feature of effective anticancer therapy.

Our overarching hypothesis is that volumetric H-scan US imaging can detect early response to chemotherapy in breast cancer tumors and provide vital prognostic data on treatment response and tumor progression. Consequently, this would provide a new and safe approach to exploring the tumor response to chemotherapy as early as possible and maximize effective therapy for an individual patient, reduce morbidity, and constrain escalating health care costs associated with overtreatment.

TABLE OF CONTENTS

ACKNOWLEDGMENTS	iv
ABSTRACT.....	v
LIST OF FIGURES	x
LIST OF TABLES	xvi
LIST OF ABBREVIATIONS.....	xvii
CHAPTER 1 INTRODUCTION	1
1.1 MOTIVATION	1
1.2 BACKGROUND	5
1.2.1 H-SCAN US IMAGING FRAMEWORK	5
1.2.2 LIMITATION OF H-SCAN US IMAGING FRAMEWORK	8
1.2.3 RESEARCH OBJECTIVES	9
1.3 REFERENCES	12
CHAPTER 2 3-D H-SCAN ULTRASOUND IMAGING OF RELATIVE SCATTERER SIZE USING SPARSE RANDOM APERTURE COMPOUNDING AND MATRIX ARRAY TRANSDUCER.....	17
2.1 INTRODUCTION	19
2.2 MATERIALS AND METHODS.....	21
2.3 RESULTS	31
2.4 DISCUSSION.....	37
2.5 CONCLUSION.....	40
2.6 ACKNOWLEDGEMENTS.....	40
2.7 REFERENCES	40
CHAPTER 3 ADAPTIVE ATTENUATION CORRECTION DURING H-SCAN ULTRASOUND IMAGING USING K-MEANS CLUSTERING	45
3.1 INTRODUCTION	47
3.2 THEORY	49
3.3 METHODOLOGY	53
3.4 RESULTS	54

3.4 DISCUSSION	59
3.6 CONCLUSION	61
3.7 ACKNOWLEDGEMENTS	61
3.8 REFERENCES	61
CHAPTER 4 THREE-DIMENSIONAL H-SCAN ULTRASOUND IMAGING AND USE OF A CONVOLUTIONAL NEURAL NETWORK FOR SCATTERER SIZE ESTIMATION	65
4.1 INTRODUCTION	67
4.2 MATERIALS AND METHODS.....	68
4.3 RESULTS	74
4.4 DISCUSSION	79
4.5 CONCLUSION.....	81
4.6 ACKNOWLEDGEMENTS	81
4.7 REFERENCES	81
CHAPTER 5 THREE-DIMENSIONAL H-SCAN ULTRASOUND IMAGING OF EARLY BREAST CANCER RESPONSE TO NEOADJUVANT THERAPY IN A MURINE MODEL.	85
5.1 PART 1	87
5.1.1 INTRODUCTION	87
5.1.2 MATERIALS AND METHODS.....	92
5.1.3 RESULTS	98
5.1.4 DISCUSSION	105
5.1.5 CONCLUSIONS.....	107
5.1.6 REFERENCES.....	108
5.2 PART 2	113
5.2.1 INTRODUCTION	113
5.2.2 MATERIALS AND METHODS.....	114
5.2.3 RESULTS AND DISCUSSION	117
5.2.4 CONCLUSION.....	120
5.2.5 ACKNOWLEDGEMENTS	120
5.2.6 REFERENCES.....	121
CHAPTER 6 CONCLUSIONS AND FUTURE WORK	123

6.1 CONCLUSIONS.....	123
6.2 FUTURE WORK.....	124
6.3 REFERENCES	129
BIOGRAPHICAL SKETCH	130
CURRICULUM VITAE	

LIST OF FIGURES

- Figure 1.1. Schematic for pulse-echo ultrasound (US) relations from (A) reflection from a boundary between two media with a small change in acoustic impedance, Z . The reflection R is modeled as a delta function. (B) A thin layer of elevated acoustic impedance is modeled as a reflection related to the derivative of the delta function. (C) A small Rayleigh scatterer has a reflection with the leading term related to the second derivative. If the transmitted pulse is a GH_4 function scaled by A_0 , then the three cases return a GH_4 , GH_5 , and a GH_6 , respectively. The classification task is then simplified to identification of these signal types.....6
- Figure 1.2. Comparison of a 2-way pulse-echo US pulse (center frequency of 6.25 MHz) and 4th order of Gaussian-weighted Hermite polynomial (GH_4).....7
- Figure 2.1. Layout of the 2-D sparse array (opti256) with red and black circles showing the selected elements. Random aperture compounding is performed by activating a sequence of four 256-element mutually exclusive random apertures in reception. The pitch between consecutive elements in the x and y directions is 0.3 mm. The rows at 9, 18, and 27 were intentionally left blank during manufacturing and are not related to the density-tapered 2-D spiral method.....23
- Figure 2.2. Pseudo-random distribution of US scatterers was used to simulate a simulated 3-D acoustic phantom (A) object with a pseudo-random arrangement. A representative 2-D arrangement of scatterers (B) in the simulated phantom material.....24
- Figure 2.3. Array geometry used for processing the radio frequency US signal. By calculating the distance between the acoustic scatterer and the receive elements, the weighted delay-and-sum beamforming was performed across all depth to provide the beamformed RF data.....26
- Figure 2.4. Schematic diagram highlighting the parallel processing strategy of 3-D volumetric H-scan US imaging. After local attenuation correction, a bandpass filter bank ($N = 256$) is applied to the US data for measuring relative strength of the received signals. Thereafter, an 8-bit color map is set for H-scan based on maximum matched filter output. Note that the color map is gradually shifting from red to blue as the filter index value changes from 1 to 256 (from low to high frequency). Array geometry used for processing the radio frequency US signal. By calculating the distance between the acoustic scatterer and the receive elements, the weighted delay-and-sum beamforming was performed across all depth to provide the beamformed RF data..... 29

- Figure 2.5. The simulated (top) and corresponding Hydrophone measured (bottom) 3-D US beam pattern from the same sparse array transmission and synthetic aperture are shown using plane wave propagation. Note that a self-defined pulse was simultaneously transmitted from 256 elements of the 2-D array. All the images are normalized to their respective maximum.....30
- Figure 2.6. Summary of the segmentation approach for quantitative measurement of acoustic scatterer size from the digitized microscope images (RGB color format) of different sized scatterers (column 1) from relatively small (top), moderate (middle), to large (bottom). After thresholding the image to identify pixels associated with the scatterer location, an active contour used for complete segmentation of each nucleus and area measurement (column 2). Next, morphological operations are used to improve the boundary definition (right column). Note that scatterers partially located outside of the image were not considered. Statistical analysis of the size estimation of different scatterers was performed thereafter. The estimated sizes of the scatterers were 42.6 (± 2.6), 70.8 (± 2.2), and 114.8 (± 4.1) μm after curve fitting with the Rayleigh function, which helps to simplify the phantom modeling procedure in simulations.....32
- Figure 2.7. Comparison of different apodization methods with different transmission and reception strategies (A) on H-scan US imaging, namely, synthetic, sparse, random, complimentary, sparseComp, and sparseTx apodization. The H-scan US image color is consistent across all different groups and the inspection of H-scan US image intensity indicates that there is no significant difference between the 6 groups.....34
- Figure 2.8. Comparison of simulated B-scan (row 1), H-scan (row 2), experimental B-scan (row 3) and H-scan (row 4) 3-D US images from a series of phantom materials containing different sized US scatterers, namely, 42.6 (± 2.6), 70.8 (± 2.2), and 114.8 (± 4.1) μm . The red hue (Lower frequency information) becomes dominant with the increase of scatterer size while the blue (Higher frequency information) diminishes...35
- Figure 2.9. Mean image intensity from co-registered B-scan and H-scan US images collected during simulation (left) and experiment (right). Note that changes in US scatterer size have a greater impact on H-scan US images compared to B-scan US results. Repeated measurements were obtained in both simulations and experiments, then the H-scan US image intensity captured from each phantom and the corresponding simulated data was computed. * indicates $p < 0.01$36
- Figure 3.1. An overview of H-scan US imaging technology, where normalized GH2 and GH8 are used as two kernels to isolate the low- and high-frequency information in echo signal $e(t)$, respectively. The low-frequency information is then color mapped as the red and the high-frequency information as the blue. A final RGB H-scan US image is the result of using the red and blue channels along with the B mode image as the green channel to increase its image resolution.....49

Figure 3.2 The raw RF signal and the frequency spectrum of low and high-frequency information isolated at different ROI windows, (A) RF signal collected from US imaging system. (B) Periodogram spectrum of RF signal in shallow and deep ROI window. The RF signal spectra changes especially its high-frequency information on lateral direction. (C) Frequency spectrum of the RF signal from the shallow ROI and its corresponding low- and high-frequency information isolated via GH2 and GH8 color mapped as red and blue, respectively (D) Frequency spectrum of the RF signal from the deep ROI and its corresponding red and blue signal information.....55

Figure 3.3. The initial pulses of GH2 and GH8 with the impact of different scaling factors on them. (A) The GH2 kernel for different factors (1, 2, 3 and 7) in time domain. (B) The frequency spectra of GH2 for different scaling factors. The center frequency of the kernel moving towards higher frequencies with the increase of scaling factor. (C) The GH8 kernel for the same scaling factors in time domain. (D) The corresponding frequency spectra for GH8 functions scaled via different scaling factors. The center frequency of GH8 kernels increases if we increase the scaling factor.....56

Figure 3.4. The centers of low- and high-frequency kernels in RF signal spectrum calculated via adaptive K-means clustering algorithm. (A) The spectrum of RF signal in deep ROI window, and the low and high-frequency centers calculated via adaptive K-means clustering. (B) The spectrum of low and high-frequency information (color mapped as red and blue, respectively) isolated by re-scaled GH2 and GH8 kernels.....57

Figure 3.5. The H-scan US images before and after frequency-dependent attenuation correction, the RF signals and the co-registered B-scan US images are provided for comparison (A) H-scan US image and its corresponding B mode image where the attenuation in the lateral direction (i.e. depth) is visible in the H-scan image as well as the RF signals. (B) Attenuation corrected H-scan US image. The image intensity is noticeably increased especially at deep part of the image. (C) H-scan US image with power-law transformation ($\gamma = 0.3$). (D) Attenuation corrected H-scan US image with power-law transformation. Image widths and depths are 30 and 44 mm, respectively. Note the uniform intensity of attenuation corrected H-scan US images. This trend also be observed in the cosigned H-scan US signal, especially when imaging depth is greater than 25mm.....58

Figure 4.1. Flowchart of three-dimensional (3D) H-scan ultrasound (US) imaging. (A) By processing the 3D US image data, the H-scan US volume is reconstructed. (B) An adaptive k-means clustering algorithm is used to adjust the Gaussian-weighted Hermite (GH) kernels to account for frequency dependent attenuation. (C) The H-scan US processing via two different order GH polynomials used as parallel convolution filters. The low and high frequency information are then color-coded as red (R) and blue (B) to make the contrast among different sized scatterers more pronounced. The envelope of the received US echo is assigned to the green (G) channel to complete the RGB map.....69

- Figure 4.2. The architecture of the deep convolutional neural network (CNN) and modified Visual Geometry Group (VGG) kernels with down sampling and feature extraction. Architecture consists of 13 convolutional with rectified linear unit (ReLU) layers and 3 fully connected layers. The input data includes H-scan US images of phantom materials embedded with US scatterers of various sizes (15 to 250 μm) and concentrations (0.1 to 1.0 %). All image data was down sampled to small patches for CNN training.....73
- Figure 4.3. 3D H-scan images from phantoms embedded with 15, 30, 40 or 250 μm scatterers at concentrations of 0.1, 0.3, 0.5 or 1.0 %. The red channel (lower frequency US signal information) becomes dominant as scatterer size progressively increases while the blue channel (higher frequency information) diminishes.....75
- Figure 4.4. Spatial analysis of the (A) red and (B) blue channel signals used to generate the H-scan US images acquired from different phantom materials. Note the blue channel intensity decreases while red image intensity increases when the scatterer size increases. (C) Mean voxel values of the H-scan US images. Average image intensity increases with corresponding increased scatterer size.....76
- Figure 4.5. Representative H-scan US slices with coregistered B-scan US images for comparison. Phantoms were prepared using either (A) 15 μm , (B) 30 μm , (C) 40 μm , or (D) 250 μm acoustic scatterers. (E) Mean image intensity and the corresponding percentage changes reveals that 3D H-scan US is more sensitive to scatterer size changes than traditional B-mode US imaging.....77
- Figure 4.6. Box and whisker plots representing the root mean square error (RMSE) of the (A) four predicted and actual scatterer sizes during the training process and the (B) scatterer size estimates produced by the trained CNN. Note that the scatterers used for testing were not used during CNN training. The mean (standard deviation, SD) of the RMSE was reported to show the robustness of our model, namely, -0.98 (0.40), -0.40 (0.34), 0.59 (0.79) and 0.94 (0.60). H-scan US-based scatterer size estimates in (B) are 59.7 (0.6) μm and 124.6 (0.6) μm78
- Figure 5.1. Apoptosis is a form of programmed cell death that leads to the physical change of cancer cells including considerable nuclear shrinkage (condensation) at the early stage after treatment with apoptosis-inducing chemotherapeutic drugs.....88
- Figure 5.2. Timeline of the *in vivo* imaging and drug treatment schedule timeline for both a shorter-term and longer-term study. At study conclusion or when tumor burden guidelines warranted, mice were sacrificed and tumors excised for *ex vivo* analysis...92

- Figure 5.3. Schematic diagram of the 3-D H-scan ultrasound image formation process. Using a pair of n th-order Gaussian-weighted Hermite polynomials (denoted GH_2 and GH_8 , respectively), parallel convolution filters were applied before normalization by the signal energy (E_n). After envelope detection, low and high frequency information is then color-coded as red and blue to describe larger and smaller ultrasound scatterers, respectively.....94
- Figure 5.4. Summary of the segmentation approach for measurement of nuclear size and location from the DAPI-stained histologic images. After nuclei localization using a directional filter bank, an initial global segmentation is performed. Nuclei edges were then processed to find the best contour with minimum calculated loss before calculating mean nuclear size from small subregions.....95
- Figure 5.5. 3-D H-scan US image reconstructions from breast cancer-bearing mice at baseline (day 0) and days 1, 2 and 3 after receiving a single dose of control or chemotherapeutic drug, namely, TRA-8, paclitaxel, or TRA-8 + paclitaxel (top). A summary of *in vivo* H-scan US image intensities reveals a marked early response and trend not found in the B-scan US measures (bottom).....99
- Figure 5.6. Comparison of matched H-scan US and histologic images depicting cell proliferation (Ki-67), apoptosis (AC3), and nuclear size (DAPI, top). Enlarged regions show breast tumor heterogeneity and a differential spatial response to neoadjuvant therapy as highlighted by the three distinct zoomed subregions. Bar plots summarize control tumor histologic measures and those administered a single dose of TRA-8, paclitaxel, or TRA-8 + paclitaxel (bottom left). A linear comparison of *in vivo* H-scan US image intensities and co-registered local measures of cancer cell nuclear size suggests that H-scan US imaging can detect increased apoptotic activity and cancer cell nuclear shrinkage in tumors administered neoadjuvant therapy. A * indicates $p < 0.05$ versus control data.....101
- Figure 5.7. 3-D H-scan US image reconstructions of breast cancer-bearing mice after receiving a single dose of sham or neoadjuvant therapy (top). A summary of *in vivo* H-scan US image intensities reveals a considerable change and longer-term treatment response (bottom).....103
- Figure 5.8. Whole body bioluminescent images of breast cancer-bearing mice at baseline (day 0) and days 3, 7, 10, and 14 after receiving a single dose of control or chemotherapeutic drug, namely, TRA-8, paclitaxel, or TRA-8 + paclitaxel (top). A summary of *in vivo* bioluminescent image intensities (bottom left) reveals a marked early response and trend comparable to that found using 3-D H-scan ultrasound imaging. Survival curves detail a general improvement in subject outcomes following neoadjuvant therapy compared to controls.....104

- Figure 5.9. Representative H-scan ultrasound (US) tumor volume reconstructions from breast cancer-bearing mice at baseline (day 0) and days 1, 3, and 7 after the start of control treatment or chemotherapy using 3 mg/kg (low dose) or 25 mg/kg (high dose) of cisplatin. A summary of H-scan US image intensities reveals marked intratumoral changes in the drug dosed animals versus those treated with sham drug.....117
- Figure 5.10. Representative diffusion-weighted magnetic resonance imaging (DW-MRI)-derived apparent diffusion coefficient (ADC) maps of breast cancer-bearing mice at baseline (day 0) and days 1, 3 and 7 after the start of control treatment or chemotherapy. A summary of ADC values reveals marked intratumoral changes in the drug dosed animals versus those treated with sham drug.....118
- Figure 5.11. Example histological images after staining for nuclear location (DAPI, top). A summary of cancer cell nuclear size measurements is provided for tumors administered control treatment or chemotherapy using 3 mg/kg (low dose) or 25 mg/kg (high dose) of cisplatin (bottom). No changes in tumor size were noted during the experimental period. A * indicates a p-value less than 0.05 versus controls.....119

LIST OF TABLES

Table 3.1. Attenuation parameter (dB/cm/MHz) calculated using adaptive K-means clustering algorithm for different order of GH functions with/without power-law correction at different depths.....	57
Table 4.1. Mean image intensity values calculated by averaging US data collected in phantom materials of varying concentrations.....	76

LIST OF ABBREVIATIONS

AC3	Activated Caspase-3
ADC	Apparent Diffusion Coefficient
B	Blue
CNN	Convolutional Neural Network
DR5	Death Receptor 5
DCE-US	Dynamic Contrast-Enhanced Ultrasound
ER	Estrogen Receptor
GH	Gaussian-Weighted Hermite
gLoG	Generalized Laplacian Of Gaussian
G	Green
HER2	Human Epidermal Growth Factor Receptor 2
IACUC	Institutional Animal Care And Use Committee
LABC	Locally Advanced Breast Cancer
MRI	Magnetic Resonance Imaging
mRLS	Multi-Scale Radial Line Scanning
NDV	Nondestructive Visualization
1D	One-Dimensional
PBS	Phosphate Buffered Saline
PR	Progesterone Receptor
QUS	Quantitative Ultrasound
RF	Radiofrequency
RFS	Recurrence-Free Survival
R	Red
ROI	Region-Of-Interest
RECIST	Response Evaluation Criteria In Solid Tumors
SWE	Shear Wave Elastography
3D	Three-Dimensional
TNBC	Triple-Negative Breast Cancer
2D	Two-Dimensional
US	Ultrasound
VGG	Visual Geometry Group

CHAPTER 1

INTRODUCTION

1.1 Motivation

Breast cancer is the most common type of malignant disease in women with the second highest mortality rate [1]. Over the last several decades, there has been a steady decline in cancer mortality due to improved screening and diagnosis. However, locally advanced breast cancer (LABC) remains a major clinical issue, and triple-negative breast cancer (TNBC) accounts for 15% of all LABC cases. TNBC is characterized by the insufficient expression of estrogen receptor (ER), progesterone receptor (PR), and human epidermal growth factor receptor 2 (HER2). Therefore, TNBC tends to grow and migrate fast and has less treatment options because of the lack of appropriate targets. More importantly, it has a higher recurrency rate compared to other types of breast cancer [2].

Studies have proven that TNBC is very sensitive to neoadjuvant chemotherapy, which made it becomes a standard of care for breast cancer treatment [3]. Application of systemic therapy before surgery benefits patients with decreased tumor bulk and improved long-term survival rates. Clinical studies have further demonstrated that an early neoadjuvant response is a better predictor of the patient's recurrence-free survival (RFS). However, TNBC is a dynamic disease, and the tumor becomes more heterogeneous during development [4]. Therefore, personalized medicine is becoming progressively important to maximize effective therapy for an individual patient [5]. Notwithstanding, the biggest challenge in monitoring neoadjuvant treatment is how to quantify response at an early stage of therapy accurately.

Early functional evaluation of treatments in oncology is of major importance. Clinical assessment, mammography, ultrasound (US), and magnetic resonance imaging (MRI) have been used to determine response. These methods of assessment involve tracking changes in tumor size which may not be detectable until after multiple cycles of chemotherapy. In the interim, significant cost and unnecessary patient toxicity may be incurred for therapy regimens that may not be effective. Moreover, although histology and other direct mechanical tests have been widely used in the characterization strategy. The use of ultrasonic systems for nondestructive visualization (NDV) of the tissue microstructure is increasingly important in the field of medical diagnostics for its noninvasive, relatively inexpensive and, most importantly, real-time [6]–[8]. Unfortunately, this imaging modality has good sensitivity but does not always provide comparable specificity, which means its ability to tissue characterization in the image is limited.

Apoptosis is a unique type of programmed cell death that kills cells in a quick and orderly fashion. This process involves a carefully orchestrated sequence of intracellular events that systematically dismantle the cell. Previous studies have demonstrated that a wide range of anticancer drugs, including chemotherapeutic agents, induce apoptosis in malignant cells *in vitro* [7], [9], [10]. Characteristic apoptotic changes have also been described in solid tumors after treatment. The first observable change in a cancer cell undergoing apoptosis is cell shrinkage [11]. Drug resistance often prevents cancer cells from undergoing sufficient levels of apoptosis, resulting in cancer cell survival and treatment failure. It is important to note that the induction of apoptosis also plays a pivotal role in other non-surgical cancer treatment regimens such as irradiation and hormones. Therefore, detecting acute apoptotic response after drug dosing may introduce a new prognostic biomarker for evaluating early treatment response.

The use of noninvasive US for quantitative tissue characterization has been the focus of research efforts. Several promising US-based tissue characterization methods have been introduced, namely, backscatter classification, spectral feature extraction and tissue elasticity imaging. These techniques examine the frequency content of backscatter US signals to extract quantitative parameters that are directly linked to the tissue microstructure. Shear wave elastography (SWE) was developed to predict therapy efficiency in treatment by measuring stiffness [12]–[14]. However, the estimation of Young's modulus can be significantly affected by respiratory and cardiac motion, loss of SWE signal, etc. Quantitative ultrasound (QUS) is another promising technique that examines the frequency content of the radiofrequency (RF) backscatter US signals from tissues [15]–[18]. Pioneer studies demonstrated that parameters (i.e., spectral slope, spectral intercept, and mid-band fit) related to the power spectrum are directly linked to the tissue microstructure [19]. It has shown a significant difference in the backscatter amplitudes which are correlated with different tissue morphology [20]. One study [3] has theoretically demonstrated nuclear condensation can produce a significant change in the backscattered signal amplitude. Additionally, a similar study [21] used an ultrasound spectral analysis method [11] to analyze measured ultrasound signals from cell ensembles treated with chemotherapeutics and also from healthy cells. They found that US backscatter intensity and spectral slope increased because of treatment and that was interpreted as a consequence of the decrease in effective scatterer size, which is also confirmed by a follow-up *in vivo* study which has successfully demonstrated the change of acoustic signal is in fact caused by the condensing of nuclear during cell apoptosis [22]. The accuracy of the QUS method is highly dependent on reference signal measurements, which can limit the accuracy of statistical approaches since the spectrum of US pulse is not uniform

throughout the acoustic field. In part, QUS techniques are too computationally intensive for existing hardware and not robust enough for all clinical use [23], [24]. Another hallmark of cancer is that glucose metabolism in tumor cells is more active than in normal tissue, which made assessing early changes in tumor perfusion another essential way to perform tissue characterization. Dynamic contrast-enhanced ultrasound (DCE-US) imaging, therefore, is developed to evaluate the perfusion parameters after antiangiogenic treatment uses contrast agents. But the approval of microbubble contrast agents for certain applications is still pending [25], [26].

Bypassing some of the limitations associated with traditional tissue characterization approaches, a new modality has recently emerged for the US classification of acoustic scatterers. Termed H-scan US (where the ‘H’ stands for Hermite or hue), this imaging approach links the mathematics of Gaussian-weighted Hermite (GH) functions to the physics of scattering and reflection from different tissue structures within a standard convolutional model of US pulse-echo systems [27]–[33]. Specific integer orders, termed GH_n , are related to the n th derivative of a Gaussian function. Matched filters employing specific orders of GH_n functions are then used to quickly analyze the spectral content of US backscattered echo signals and to colorize the display. This provides visual discrimination between the major tissue scattering classes at high resolution. In general, lower frequency spectral content is generated from larger scattering structures, whereas higher frequency echo content is produced by a US wave interacting with small scatterers of the scale below the wavelength of the US transmit pulse (i.e., Rayleigh scatterers). In short, H-scan US estimates the relative size and spatial distribution of cellular structures and has shown promise in applications ranging from characterization of thyroid nodules [13], [28] to monitoring cancer response to treatment [34], [35].

1.2 Background

1.2.1 H-scan US Imaging Framework

The backscattered US signal can be modeled as a convolution of an incident pulse with a sequence of tissue reflections [36]. In simplified one-dimensional (1D) derivations with an assumption of small spatial variations in density and compressibility, the received signal $R(x)$ can be related to the spatial derivative of the acoustic impedance, $Z = \rho c$, where x is the direction of pulse propagation and ρ and c denote tissue density and compressibility, respectively. Therefore, it can be shown that:

$$R(x) \approx \left(\frac{1}{2Z}\right) \frac{dZ(x)}{dx} \quad (1)$$

Here we consider three simple types of reflections in a 1D convolution model. First, a small step increase in acoustic impedance at position x_0 . An example of this would be the interface between venous blood and soft tissue. The reflection coefficient R_I at x_0 will be proportional to the spatial derivative of the acoustic impedance at that location:

$$R_I(x_0) \approx \frac{\Delta Z}{2Z} \delta(x - x_0) \quad (2)$$

where $\delta(\cdot)$ is the Dirac delta function and derivative of the unit step function. Next, we consider a thin material of higher acoustic impedance ΔZ , such as an arterial wall. In the limit, as the front and back walls are located closer together, the reflection function R_T is:

$$R_T(x_0) \approx \frac{\Delta Z}{2Z} \delta'(x - x_0) \quad (3)$$

where $\delta'(\cdot)$ is the derivative of the Dirac delta function. Finally, in more general scattering theory, the Born approximation for a small (subwavelength) spherical scatterer has a leading term for backscattered pressure that is proportional to $\omega^2(\Delta Z a^3)$, where ω and a are the signal frequency and scatterer radius, respectively. The ω^2 frequency weighting is an important analytical endpoint because by Fourier transform theorems, an ω^2 weighting corresponds to the second derivative of a function, equivalent to convolution with $\delta''(\cdot)$, the second derivative of the Dirac delta function. Given these three different results described in Figure 1.1, the next task is to identify US echoes

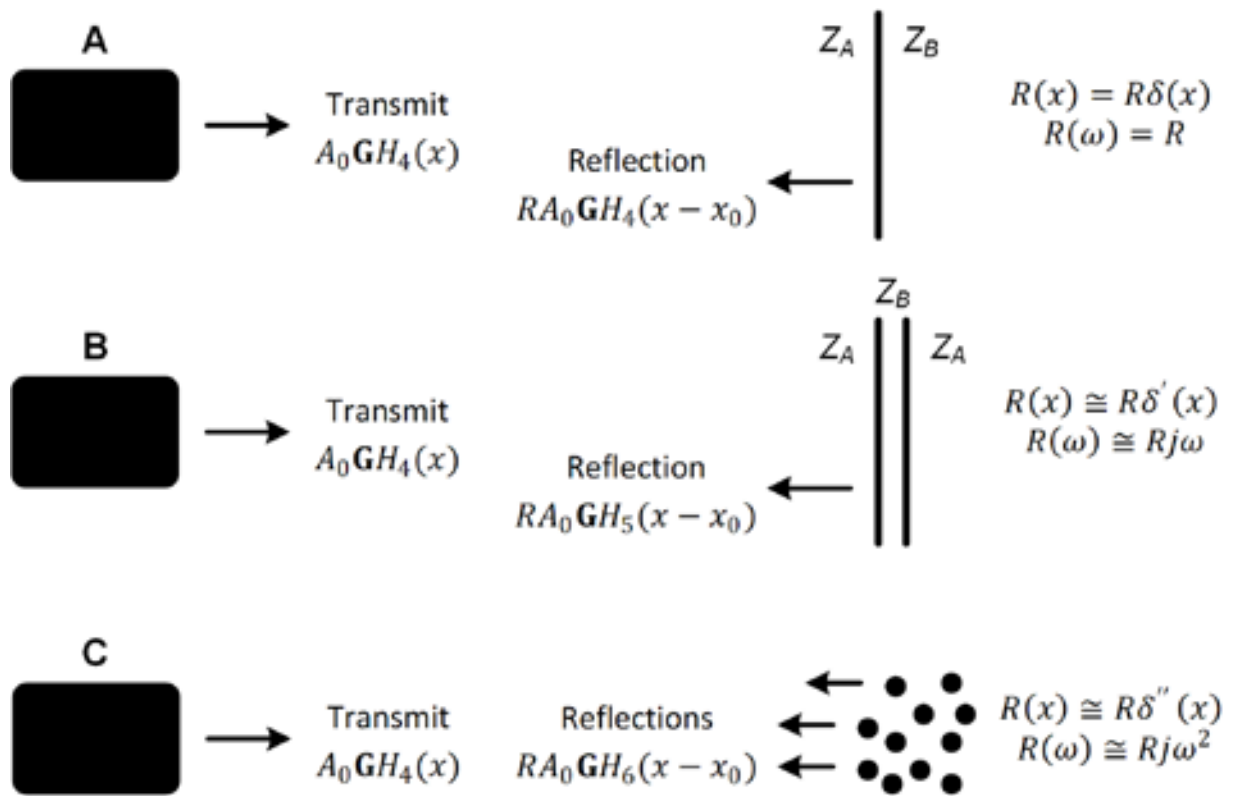


Figure 1.1. Schematic for pulse-echo ultrasound (US) relations from (A) reflection from a boundary between two media with a small change in acoustic impedance, Z . The reflection R is modeled as a delta function. (B) A thin layer of elevated acoustic impedance is modeled as a reflection related to the derivative of the delta function. (C) A small Rayleigh scatterer has a reflection with the leading term related to the second derivative. If the transmitted pulse is a GH_4 function scaled by A_0 , then the three cases return a GH_4 , GH_5 , and a GH_6 , respectively. The classification task is then simplified to identify these signal types.

by their relationship to the transmitted US pulse and its derivatives. A family of functions related to the Hermite polynomials is one solution.

Successive differentiation of a Gaussian pulse generates the n^{th} order Hermite polynomial. Here we use the notation GH_n to denote the Gaussian-weighted Hermite polynomial of order n and energy E_n . As illustrated in Figure 1.2, let us assume a pulse-echo US system with a round trip impulse response of $R(x) = A_0 GH_4(x)$, where A_0 is a scaling factor, then from our model and for the echoes e from the step, thin layer, and Rayleigh scatterer are:

$$e_l(t) = A_0 Z_0 GH_n(t)(t - t_o) \quad (6)$$

$$e_m(t) = A_0 Z_0 GH_{n+1}(t)(t - t_o) \quad (7)$$

$$e_s(t) = A_0 Z_0 GH_{n+2}(t)(t - t_o) \quad (8)$$

respectively, where the derivative identities of the GH_n functions are used. In the above formulation, the received echoes can be classified by similarity to either GH_4 , GH_5 , or GH_6 . A matched filter approach would suggest a convolution of the received signal with scaled versions

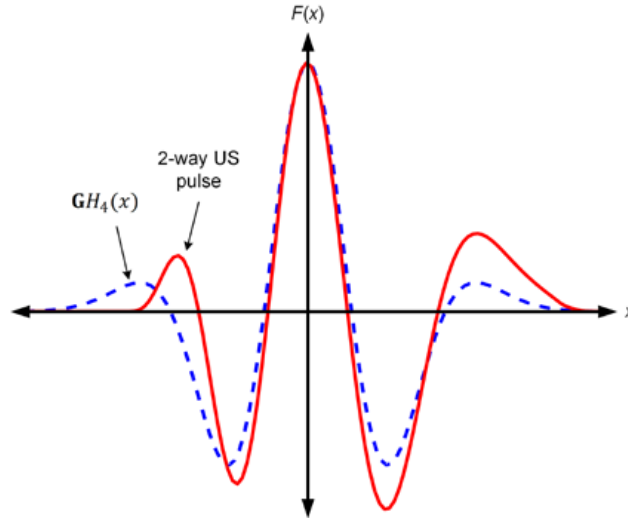


Figure 1.2. Comparison of a 2-way pulse-echo US pulse (center frequency of 6.25 MHz) and 4th order of Gaussian-weighted Hermite polynomial (GH_4).

of GH_4 , GH_5 , or GH_6 to form three postprocessed US signals. An intuitive classification approach would simply display the relative strength of the convolution results as colors. However, the correlation between GH_4 and GH_5 , and similarly for GH_5 and GH_6 , are substantial due to the significant overlap of spectra. To address this issue, some minor adjustments are warranted. One approach is to use the standard envelope as intensity with two parallel convolution filters applied to measure the relative strength of the US echoes with respect to GH_4 and GH_6 . To further minimize spectral overlap, we put more emphasis on the extremes of the spectra by employing GH_2 and GH_8 , to capture the low and high-frequency information, respectively. Thereafter, the lower and higher frequency convolution filter outputs are each assigned a red (R) and blue (B) color, respectively, after envelope detection.

1.2.2 Limitation of H-scan US Imaging Framework

During H-scan US imaging, frequency-dependent attenuation can significantly diminish the image quality and its ability of tissue characterization when imaging deep tissue [37]. Several studies have been done to address the frequency-dependent attenuation. One study [38] proposed a comprehensive correction method to measure and eliminate the effect of attenuation based on the Fourier transform of the tissue motion. But they need robust wave generation with the acoustic radiation force beam and motion detection methods to track waves that could be affected by phase aberration and attenuation in the first case. Another study [16] reported favorable attenuation correction achievements by investigating and comparing the reference US pulse received from a hydrophone with the attenuated signal. But their approach needs a complicated signal analysis to control the gain. Although the proposed histogram equalization for image processing can be used as an alternative to attenuation compensation, the quantification of image intensity based on this

approach still needs to be validated [39]. While the techniques presented in the abovementioned three studies have shown improvements in attenuation correction, they were all developed based on traditional B-mode US images. As introduced previously, H-scan US imaging involves different ordered GH kernels to isolate echoes to classify and visualize major scattering classes, which complicates these attenuation correction techniques.

Moreover, cancer is a heterogeneous group of tissues with different histological prognostic, and clinical aspects. This heterogeneity has been documented at both the spatial and temporal level. Thus, it poses a fundamental evaluation challenge because different tumor subregions might have different drug sensitivities. This implies that 2D H-scan US evaluation strategies might not represent the whole tumor.

1.2.3 Research Objectives

The overall objective of this work is to reduce the barrier to clinical application of H-scan with robust methods to classify the tissue scatterers responsible for the backscattered US signal generation and subsequently used for tissue imaging. The main paths to this objective are to develop a robust three-dimensional (3D) H-scan US imaging technique to capture data from the entire tumor burden. The availability of volumetric information allowed the introduction of innovative applications for tissue characterization, as well as for surgery by intraoperative visualization. Two-dimensional arrays for 3-D imaging systems are already available for research purposes [40]–[43], it can capture data from the entire tumor burden to produce a more robust tumor statistic. Moreover, 2-D arrays enable ultrafast imaging [44]–[47] by the transmission of a plane or diverging waves, which can also be combined to improve contrast and resolution. Hence, we hypothesize that 3D H-scan US imaging will capture data from the entire tumor burden, allow

visualization of any heterogenous tissue patterns, and fundamentally improve any tissue characterization strategy and treatment response determination, especially when data averaging is employed to produce a more robust tumor statistic.

Specific Aim 1: Maximize image quality in volume space and then evaluate the sensitivity of 3-D H-scan US imaging technique.

(a): Develop a detailed simulation program to investigate theoretical considerations supporting the novel H-scan US technology and help guide future 3-D H-scan US developments.

(b): Develop a real-time 3D H-scan US imaging system equipped with a custom two-dimensional (2D) 1024-element (32 x 32) matrix array transducer

(c): Confirm the results of simulation with *in vitro* experiments in tissue-mimicking phantoms.

Specific Aim 2: Improve the tissue characterization ability of the H-scan when imaging complex tissue at depth.

(a): Implement a frequency-dependent attenuation correction technique to adjust GH kernels at depth based on K-means clustering algorithms.

(b): Test the proposed technique with *ex vivo* tissue.

Specific Aim 3: Implement new US excitation pulsing and machine learning algorithms to help improve H- scan US image quality and tissue classification.

(a): Implement a real-time 3-D H-scan US imaging technique using a customized wobbler linear transducer.

(b): Test the proposed technique with *in vitro* tissue-mimicking phantom embedded with different-sized scatterers.

(c): Implement a deep convolution neural network (CNN) to help improve the H- scan US scatterer size estimation ability.

Specific Aim 4: Evaluate the 3-D H-scan US imaging for monitoring tumor response to neoadjuvant chemotherapy in a novel transgenic murine model of breast cancer.

(a): Confirm the H-scan results with *in vivo* bioluminescent imaging findings.

(b): Confirm the H-scan results with *ex vivo* histological findings.

Chapters 2 – 5 address aims 1 – 4, respectively. In Chapter 2, we introduce herein an H-scan US imaging system equipped with a 32×32 element matrix array transducer and method for voxel-level characterization of US scattering. The primary objective of this research was to maximize image quality in volume space and then evaluate the sensitivity of H-scan US imaging and compare findings to traditional B-scan US results. It was found that H-scan US was more sensitive to changes in scatterer size than traditional B-scan US imaging. In Chapter 3, a compensation strategy by using an adaptive K-means clustering algorithm is proposed in this paper to adjust GH polynomials based on RF signal spectra changes at different depth to improve the robustness and reliability of the H-scan US imaging method for tissue characterization across different organs in the lateral direction.

We found that the proposed method can properly adjust the GH kernels to account for frequency-dependent attenuation, which leads to the formation of an H-scan US image with a more uniform brightness. This technique may eventually enable the imaging of complex tissue at depth to monitor the tumor response to therapy at an early stage. In Chapter 4, We investigate the feasibility of using 3D H-scan US volumes for tracking relative changes in scatterer size throughout the entire volume space. A convolutional neural network (CNN) architecture based on

a modified Visual Geometry Group (VGG) regression model was introduced to map the H-scan US image to scatterer size and enable real-time tissue characterization. We demonstrate that the H-scan US image intensity was considerably impacted by variations in scatterer size but not concentration and use of a CNN architecture based on a modified VGG regression model allowed voxel-level mapping of H-scan US data to scatterer sizes. In Chapter 5, we detailed the initial use of *in vivo* 3-D H-scan ultrasound imaging for the assessment of early TNBC response to neoadjuvant therapy. The experimental results suggest that the proposed *in vivo* 3-D H-scan ultrasound imaging is a promising technique that allows visualization of the heterogeneous tumor microenvironment in a mouse model of TNBC. Validated by two independent *in vivo* studies and *ex vivo* histological measures. Nuclear size was shown to have a strong linear correlation with local H-scan ultrasound image intensity that also coincided with biomarkers of cancer cell death like apoptosis.

1.3 References

- [1] A. G. Liddane, C. A. McNamara, M. C. Campbell, I. Mercier, and J. M. Holaska, “Defects in Emerin-nucleoskeleton binding disrupt nuclear structure and promote breast cancer cell motility and metastasis,” *Mol. Cancer Res. MCR*, vol. 19, no. 7, pp. 1196–1207, Jul. 2021.
- [2] J. M. Warram, A. G. Sorace, R. Saini, H. R. Umphrey, K. R. Zinn, and K. Hoyt, “A Triple-Targeted Ultrasound Contrast Agent Provides Improved Localization to Tumor Vasculature,” *J. Ultrasound Med.*, vol. 30, no. 7, pp. 921–931, 2011.
- [3] A. Sadeghi-Naini *et al.*, “Quantitative Ultrasound Evaluation of Tumor Cell Death Response in Locally Advanced Breast Cancer Patients Receiving Chemotherapy,” *Clin. Cancer Res.*, vol. 19, no. 8, pp. 2163–2174, Apr. 2013.
- [4] O. S. Al-Kadi, D. Y. F. Chung, C. C. Coussios, and J. A. Noble, “Heterogeneous Tissue Characterization Using Ultrasound: A Comparison of Fractal Analysis Backscatter Models on Liver Tumors,” *Ultrasound Med. Biol.*, vol. 42, no. 7, pp. 1612–1626, Jul. 2016.

- [5] P. Narayan *et al.*, “FDA Approval Summary: Atezolizumab Plus Paclitaxel Protein-bound for the Treatment of Patients with Advanced or Metastatic TNBC Whose Tumors Express PD-L1,” *Clin. Cancer Res.*, vol. 26, no. 10, pp. 2284–2289, May 2020.
- [6] C. D. Herickhoff, M. R. Morgan, J. S. Broder, and J. J. Dahl, “Low-cost Volumetric Ultrasound by Augmentation of 2D Systems: Design and Prototype,” *Ultrason. Imaging*, vol. 40, no. 1, pp. 35–48, Jan. 2018.
- [7] B. Banihashemi, R. Vlad, B. Debeljevic, A. Giles, M. C. Kolios, and G. J. Czarnota, “Ultrasound Imaging of Apoptosis in Tumor Response: Novel Preclinical Monitoring of Photodynamic Therapy Effects,” *Cancer Res.*, vol. 68, no. 20, pp. 8590–8596, Oct. 2008.
- [8] Guofang Xiao, M. Brady, J. A. Noble, and Yongyue Zhang, “Segmentation of ultrasound B-mode images with intensity inhomogeneity correction,” *IEEE Trans. Med. Imaging*, vol. 21, no. 1, pp. 48–57, Jan. 2002.
- [9] M. J. Arends and A. H. Wyllie, “Apoptosis: Mechanisms and Roles in Pathology,” in *International Review of Experimental Pathology*, vol. 32, G. W. Richter and K. Solez, Eds. Academic Press, 1991, pp. 223–254.
- [10] C. Creeley, K. Dikranian, G. Dissen, L. Martin, J. Olney, and A. Brambrink, “Propofol-induced apoptosis of neurones and oligodendrocytes in fetal and neonatal rhesus macaque brain,” *BJA Br. J. Anaesth.*, vol. 110, no. Suppl 1, pp. i29–i38, Jun. 2013.
- [11] M. C. Kolios, G. J. Czarnota, M. Lee, J. W. Hunt, and M. D. Sherar, “Ultrasonic spectral parameter characterization of apoptosis,” *Ultrasound Med. Biol.*, vol. 28, no. 5, pp. 589–597, May 2002.
- [12] A. Athanasiou, H. Latorre-Ossa, A. Criton, A. Tardivon, J.-L. Gennisson, and M. Tanter, “Feasibility of Imaging and Treatment Monitoring of Breast Lesions with Three-Dimensional Shear Wave Elastography,” *Ultraschall Med. Stuttg. Ger. 1980*, vol. 38, no. 1, pp. 51–59, Jan. 2017.
- [13] V. Cantisani *et al.*, “Strain US Elastography for the Characterization of Thyroid Nodules: Advantages and Limitation,” *International Journal of Endocrinology*, 2015. <https://www.hindawi.com/journals/ije/2015/908575/abs/> (accessed May 21, 2019).
- [14] B. Castaneda *et al.*, “Prostate cancer detection using crawling wave sonoelastography,” in *Medical Imaging 2009: Ultrasonic Imaging and Signal Processing*, 2009, vol. 7265, p. 726513.
- [15] D. Dalecki, K. P. Mercado, and D. C. Hocking, “Quantitative Ultrasound for Nondestructive Characterization of Engineered Tissues and Biomaterials,” *Ann. Biomed. Eng.*, vol. 44, no. 3, pp. 636–648, Mar. 2016.

- [16] E. Fiore *et al.*, “Application of texture analysis of b-mode ultrasound images for the quantification and prediction of intramuscular fat in living beef cattle: A methodological study,” *Res. Vet. Sci.*, vol. 131, pp. 254–258, Aug. 2020.
- [17] K. Hoyt, A. Sorace, and R. Saini, “Quantitative mapping of tumor vascularity using volumetric contrast enhanced ultrasound,” *Invest. Radiol.*, vol. 47, no. 3, p. 167, 2012.
- [18] M. Zhang *et al.*, “Quantitative characterization of viscoelastic properties of human prostate correlated with histology,” *Ultrasound Med. Biol.*, vol. 34, no. 7, pp. 1033–1042, 2008.
- [19] C. H. Heath, A. Sorace, J. Knowles, E. Rosenthal, and K. Hoyt, “Microbubble therapy enhances anti-tumor properties of cisplatin and cetuximab in vitro and in vivo,” *Otolaryngol. Neck Surg.*, vol. 146, no. 6, pp. 938–945, 2012.
- [20] Z. Wu, K. Hoyt, D. J. Rubens, and K. J. Parker, “Sonoelastographic imaging of interference patterns for estimation of shear velocity distribution in biomaterials,” *J. Acoust. Soc. Am.*, vol. 120, no. 1, pp. 535–545, 2006.
- [21] I. Z. Nenadic *et al.*, “Attenuation measuring ultrasound shearwave elastography and in vivo application in post-transplant liver patients,” *Phys. Med. Biol.*, vol. 62, no. 2, pp. 484–500, 21 2017.
- [22] P. W. Mesner, I. I. Budihardjo, and S. H. Kaufmann, “Chemotherapy-Induced Apoptosis,” in *Advances in Pharmacology*, vol. 41, S. H. Kaufmann, Ed. Academic Press, 1997, pp. 461–499.
- [23] Z. Zhou, Q. Zhang, W. Wu, S. Wu, and P.-H. Tsui, “Hepatic Steatosis Assessment Using Quantitative Ultrasound Parametric Imaging Based on Backscatter Envelope Statistics,” *Appl. Sci.*, vol. 9, no. 4, Art. no. 4, Jan. 2019.
- [24] R. M. Vlad, N. M. Alajez, A. Giles, M. C. Kolios, and G. J. Czarnota, “Quantitative ultrasound characterization of cancer radiotherapy effects in vitro,” *Int. J. Radiat. Oncol. Biol. Phys.*, vol. 72, no. 4, pp. 1236–1243, Nov. 2008.
- [25] R. Saini and K. Hoyt, “Recent developments in dynamic contrast-enhanced ultrasound imaging of tumor angiogenesis,” *Imaging Med.*, vol. 6, no. 1, p. 41, 2014.
- [26] J. Zhou *et al.*, “Early Prediction of Tumor Response to Bevacizumab Treatment in Murine Colon Cancer Models using Three-Dimensional Dynamic Contrast-Enhanced Ultrasound Imaging,” *Angiogenesis*, vol. 20, no. 4, pp. 547–555, Nov. 2017.
- [27] J. Baek and K. J. Parker, “H-scan trajectories indicate the progression of specific diseases,” *Med. Phys.*, vol. 48, no. 9, pp. 5047–5058, 2021, doi: 10.1002/mp.15108.
- [28] G. R. Ge *et al.*, “H-scan analysis of thyroid lesions,” *J. Med. Imaging*, vol. 5, no. 1, p. 013505, Feb. 2018.

- [29] M. Khairalseed and K. Hoyt, "Integration of a CMUT linear array for wideband H-scan ultrasound imaging," in *2019 IEEE International Ultrasonics Symposium (IUS)*, Oct. 2019, pp. 1519–1522.
- [30] M. Khairalseed, K. Hoyt, J. Ormachea, A. Terrazas, and K. J. Parker, "H-scan sensitivity to scattering size," *J. Med. Imaging Bellingham Wash*, vol. 4, no. 4, p. 043501, Oct. 2017.
- [31] H. Tai, M. Khairalseed, and K. Hoyt, "3-D H-Scan Ultrasound Imaging and Use of a Convolutional Neural Network for Scatterer Size Estimation," *Ultrasound Med. Biol.*, vol. 46, no. 10, pp. 2810–2818, Oct. 2020.
- [32] H. Tai, J. Song, J. Li, S. Reddy, M. Khairalseed, and K. Hoyt, "Three-Dimensional H-Scan Ultrasound Imaging of Early Breast Cancer Response to Neoadjuvant Therapy in a Murine Model," *Invest. Radiol.*, vol. 57, no. 4, pp. 222–232, Apr. 2022.
- [33] M. Khairalseed, K. Brown, K. J. Parker, and K. Hoyt, "Real-time H-scan ultrasound imaging using a Verasonics research scanner," *Ultrasonics*, vol. 94, pp. 28–36, Apr. 2019.
- [34] M. Khairalseed, K. Javed, G. Jashkaran, J.-W. Kim, K. J. Parker, and K. Hoyt, "Monitoring Early Breast Cancer Response to Neoadjuvant Therapy Using H-Scan Ultrasound Imaging," *J. Ultrasound Med. Off. J. Am. Inst. Ultrasound Med.*, vol. 38, no. 5, pp. 1259–1268, May 2019.
- [35] K. J. Parker and J. Baek, "Fine-tuning the H-scan for discriminating changes in tissue scatterers," *Biomed. Phys. Eng. Express*, vol. 6, no. 4, p. 045012, May 2020.
- [36] J. W. Hunt, A. E. Worthington, and A. T. Kerr, "The subtleties of ultrasound images of an ensemble of cells: simulation from regular and more random distributions of scatterers," *Ultrasound Med. Biol.*, vol. 21, no. 3, pp. 329–341, Jan. 1995.
- [37] M. Biswas *et al.*, "Symtosis: A liver ultrasound tissue characterization and risk stratification in optimized deep learning paradigm," *Comput. Methods Programs Biomed.*, vol. 155, pp. 165–177, 2018.
- [38] R. Kuc, "Clinical Application of an Ultrasound Attenuation Coefficient Estimation Technique for Liver Pathology Characterization," *IEEE Trans. Biomed. Eng.*, vol. BME-27, no. 6, pp. 312–319, Jun. 1980.
- [39] H. D. Cheng and X. J. Shi, "A simple and effective histogram equalization approach to image enhancement," *Digit. Signal Process.*, vol. 14, no. 2, pp. 158–170, Mar. 2004.
- [40] A. Austeng and S. Holm, "Sparse 2-D arrays for 3-D phased array imaging - design methods," *IEEE Trans. Ultrason. Ferroelectr. Freq. Control*, vol. 49, no. 8, pp. 1073–1086, Aug. 2002.

- [41] J. W. Choe, Ö. Oralkan, and P. T. Khuri-Yakub, “Design optimization for a 2-D sparse transducer array for 3-D ultrasound imaging,” in *2010 IEEE International Ultrasonics Symposium*, Oct. 2010, pp. 1928–1931.
- [42] S. Harput *et al.*, “3-D Super-Resolution Ultrasound Imaging With a 2-D Sparse Array,” *IEEE Trans. Ultrason. Ferroelectr. Freq. Control*, vol. 67, no. 2, pp. 269–277, Feb. 2020.
- [43] G. R. Lockwood, J. R. Talman, and S. S. Brunke, “Real-time 3-D ultrasound imaging using sparse synthetic aperture beamforming,” *IEEE Trans. Ultrason. Ferroelectr. Freq. Control*, vol. 45, no. 4, pp. 980–988, Jul. 1998.
- [44] L. Fang, N. He, S. Li, A. J. Plaza, and J. Plaza, “A New Spatial–Spectral Feature Extraction Method for Hyperspectral Images Using Local Covariance Matrix Representation,” *IEEE Trans. Geosci. Remote Sens.*, vol. 56, no. 6, pp. 3534–3546, Jun. 2018.
- [45] B. Heiles *et al.*, “Ultrafast 3D Ultrasound Localization Microscopy Using a 32 \times 32 Matrix Array,” *IEEE Trans. Med. Imaging*, vol. 38, no. 9, pp. 2005–2015, Sep. 2019.
- [46] C. Holmes, B. W. Drinkwater, and P. D. Wilcox, “Post-processing of the full matrix of ultrasonic transmit–receive array data for non-destructive evaluation,” *NDT E Int.*, vol. 38, no. 8, pp. 701–711, Dec. 2005.
- [47] J. Yu, H. Yoon, Y. M. Khalifa, and S. Y. Emelianov, “Design of a Volumetric Imaging Sequence Using a Vantage-256 Ultrasound Research Platform Multiplexed With a 1024-Element Fully Sampled Matrix Array,” *IEEE Trans. Ultrason. Ferroelectr. Freq. Control*, vol. 67, no. 2, pp. 248–257, Feb. 2020.

CHAPTER 2

**3-D H-SCAN ULTRASOUND IMAGING OF RELATIVE SCATTERER SIZE USING
SPARSE RANDOM APERTURE COMPOUNDING AND
MATRIX ARRAY TRANSDUCER***

Authors – Haowei Tai ¹, Lokesh Basavarajappa ², Kenneth Hoyt ^{2*}

¹ Department of Electrical and Computer Engineering, EC 33

The University of Texas at Dallas

800 West Campbell Road

Richardson, Texas 75080-3021

² Department of Bioengineering, EC 39

The University of Texas at Dallas

800 West Campbell Road

Richardson, Texas 75080-3021

*Reproduced with permission from Tai, Haowei, Lokesh Basavarajappa, and Kenneth Hoyt. "3-D H-scan ultrasound imaging of relative scatterer size using a matrix array transducer and sparse random aperture compounding." *Computers in Biology and Medicine* (2022): 106316.

Author contribution: Haowei Tai (myself) was responsible for the experimental design, data analysis, and the manuscript preparation presented here.

In this study, we detail 3-D H-scan US as a high-resolution imaging technology for voxel-level tissue characterization. Using a matrix array transducer, H-scan US imaging system was developed to comprehensively evaluate the relative size of US scattering aggregates in volume space. Experimental data was acquired using a programmable US scanner (Vantage 256, Verasonics Inc, Kirkland, WA) equipped with a 1024-element (32×32) matrix array transducer (Vermon Inc, Tours, France). US imaging was performed using a full array in transmission. Radiofrequency (RF) data sequences were collected using the sparse random aperture compounding technique with four mutually exclusive sparse apertures. Plane wave imaging at five angles was performed at a center frequency of 8 MHz. Scan conversion and attenuation correction were applied. To generate the 3-D H-scan US image, a mathematically designed convolution filter bank ($N = 256$) was used to process the RF data sequences and measure the fine grain shifts of the received signals. Preliminary studies were conducted using tissue-mimicking phantom materials embedded with different-sized spherical scatterers. Both simulated and experimental results indicate that the proposed volumetric H-scan US imaging method has low spatial variance when tested with homogeneous phantom materials and is more sensitive than B-mode US for differentiating US scatterers of varying size. Overall, this study helps demonstrate feasibility of evaluating tissue scatterer patterns in volume space using 3-D H-scan US imaging.

2.1 Introduction

Cancer accounts for nearly 600,000 deaths every year [1]. Traditional chemotherapy is not effective for all patients due in part to tumor heterogeneity, which implicates that detection of any early tumor response (or lack thereof) is critically important. To have a better understanding of cancer treatment protocols and to improve development of more personalized medicines, monitoring the tissue microstructure is an evolving clinical procedure. Noninvasive medical imaging offers promising solutions. To that end, several ultrasound (US)-based techniques have been investigated for the purpose of soft tissue characterization and include attenuation and backscatter coefficient estimation [2], [3], tissue elastography [4]–[6], shear wave speed and attenuation quantification [7]–[9], and speckle pattern analysis [10]. Each of these techniques provide different insight into the underlying target tissue structures. To simplify tissue characterization in real-time, a novel high-resolution US-based modality has emerged. Termed H-scan US (where the ‘H’ stands for Hermite or hue) imaging, this technique depicts the relative size of US scatterer aggregates [11]. Our previous studies have demonstrated that H-scan US imaging can distinguish subtle changes at the cellular level that are otherwise not visible in the traditional B-scan US images [12], [13], thereby adding new information to a diagnostic US examination.

It is widely understood that diseased tissues like cancerous lesions are heterogenous in composition. This disease heterogeneity has implications in pathogenesis, diagnosis, and therapeutic management [14]. This suggests that a 2-dimensional (2-D) cross-sectional tissue assessment may not sufficiently represent conditions throughout the entire diseased tissue burden. While magnetic resonance imaging (MRI)-based methods allow tissue characterization in volume space [15]–[17], there are some inherent safety issues. These include the effects of high magnetic

fields and radiofrequency (RF) pulses on the body and on implanted devices. Claustrophobia and hearing loss are additional risks of clinical MRI examinations. With the development of 3-D transducer technology, US imaging can now provide complementary tissue information in volume space with isotropic measures [18]. While the earlier mechanically-driven wobbler transducers are sufficient for US-based tissue characterization [19]–[21], device bulkiness and issues like position tracking introduce control errors that make it relatively difficult to record tilt angle of each imaging plane within the volume acquisition. Further, depending on the region-of-interest (ROI) and transducer sweep speed, US imaging using mechanically driven wobbler transducers is limited to volume rates on the low Hz scale.

The recent development of programmable US systems equipped with matrix array transducers has created new opportunities for volumetric imaging with high spatiotemporal resolution [22]–[24]. For example, the use of plane or diverging waves with these transducer technologies allow acquisition of volume data at rates up to 20 kHz [25]. When coupled with advanced shear wave elastography techniques, the prospect of 3-D tissue characterization is becoming a reality [26]. To that end, we introduce herein a H-scan US imaging system equipped with a 32×32 element matrix array transducer and method for voxel-level characterization of US scattering. The primary objective of this research was to maximize image quality in volume space and then evaluate the sensitivity of H-scan US imaging and compare findings to traditional B-scan US results. To investigate theoretical considerations supporting this novel H-scan US technology, a detailed simulation program was also developed. The proposed simulation provides additional insight into the existing US technology and may help guide future 3-D H-scan US developments.

The feasibility of using US imaging for detecting relative changes in scatterer size was assessed using a series of phantom materials in simulation and experimentation.

2.2 Materials and Methods

2.2.1 Simulation Program

A custom US simulation program was developed in MATLAB (MathWorks Inc, Natick, MA) using the Field II open-source toolkit [27]. A 1024-element (32×32 element) matrix array transducer was implemented to match the spatial configuration and layout as depicted in Figure 2.1. The center frequency f_0 was set to 8 MHz with an effective bandwidth σ of 60% and backscattered US signal sampling frequency of 32 MHz. The spatial impulse response was defined for the simulated transducer and elements were excited using a modified function during transmission to match experimental setting (detailed below). Briefly, the simulated backscattered US signal $e(t)$ was generated by convolving the US pulse-echo (i.e. one-way) response $h(t)$ of the transducer with a medium consisting of randomly distributed US scatterers as follows [28]:

$$e(t) = h(t) * b(\alpha)s(t) \quad (1)$$

where $*$ denotes convolution and the $b(\alpha)s(t)$ product describes the local scattering function. To simulate the impact of different-sized US scatterers, the scattering function was further defined to have the following distribution [29]:

$$b(\alpha) = \frac{8R_s^2 k^4 \alpha^3 e^{-\frac{k^2 \alpha^2}{4}}}{\sqrt{\pi}} \quad (2)$$

where α denotes scatterer size (radius), $R_s = R_i \sqrt{(N\alpha^3 + N^2\alpha^6)}$, R_i is the amplitude reflection coefficient, N is the scatterer density, $k = 2\pi f_0/c$, and c is the speed of sound. To match the

transmitted US signal generated by our experimental platform, the simulated one-way response was defined as [30]:

$$h(t) = \frac{e^{-\frac{t^2}{2\sigma^2}}}{\sigma\sqrt{(2\pi)}}(4t^2 - 1) \quad (3)$$

A pulse-echo US system with a round trip (transmit-receive) impulse response is then approximated as:

$$h(t) * b(\alpha)s(t) = A_0b(\alpha)\frac{e^{-\frac{t^2}{2\sigma^2}}}{\sigma}H_n(t) \approx A_0b(\alpha)GH_n(t) \quad (4)$$

where A_0 is an amplitude scaling constant. Note the n^{th} -order Hermite function $H_n(t)$ was defined by Pierre-Simon Laplace [31] and successive differentiation of this polynomial yields the following:

$$H_n(t) = (-1)^n e^{t^2} \frac{d^n}{dt^n} G(t) \quad (5)$$

$$n = 0, 1, 2, \dots, -\infty < t < \infty$$

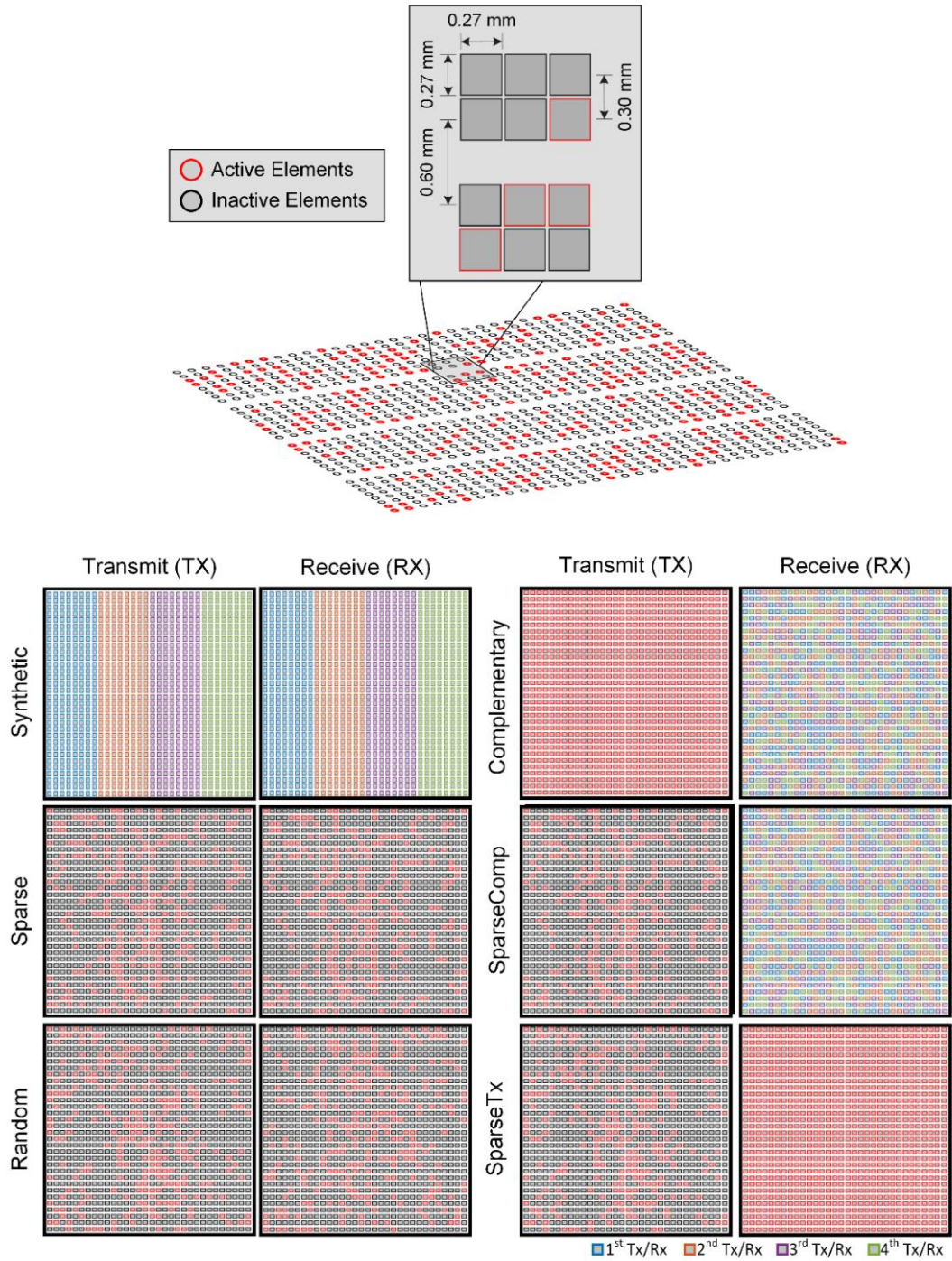


Figure 2.1. Layout of the 2-D sparse array (opti256) with red and black circles showing the selected elements. Random aperture compounding is performed by activating a sequence of four 256-element mutually exclusive random apertures in reception. The pitch between consecutive elements in the x and y directions is 0.3 mm. The rows at 9, 18, and 27 were intentionally left blank during manufacturing and are not related to the density-tapered 2-D spiral method.

where $\frac{d^n}{dt^n} G(t)$ is the n^{th} order derivative for a Gaussian pulse, $G(t) = e^{-t^2}$. A previous study has shown a pulse-echo US system with $f_0 = 8$ MHz has a round trip impulse response that is very similar to a 4th-order Gaussian-weighted Hermite polynomial, $GH_4(t)$ [32].

In practice, different GH_n functions can be used to produce a bandpass filter bank to isolate frequency information of interest. In fact, if we assume that the $GH_n(t)$ function resembles a

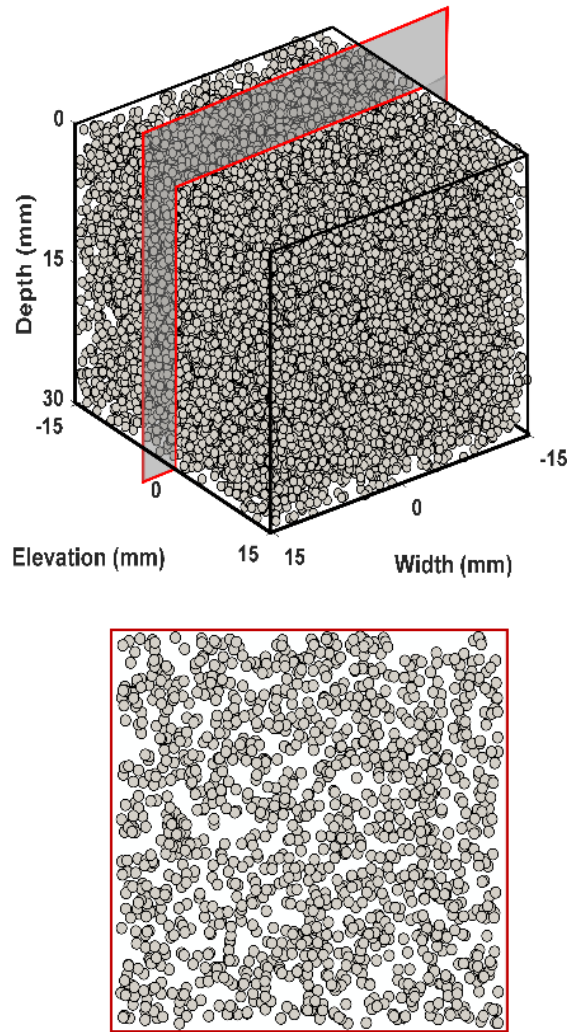


Figure 2.2. Pseudo-random distribution of US scatterers was used to simulate a simulated 3-D acoustic phantom (A) object with a pseudo-random arrangement. A representative 2-D arrangement of scatterers (B) in the simulated phantom material.

general broadband US pulse and that a pulse-echo system has a round trip impulse response of $A_0GH_n(t)$, then the backscattered US signal can be approximated as:

$$e_l(t) = A_0Z_0GH_n(t)(t - t_o) \quad (6)$$

$$e_m(t) = A_0Z_0GH_{n+1}(t)(t - t_o) \quad (7)$$

and

$$e_s(t) = A_0Z_0GH_{n+2}(t)(t - t_o) \quad (8)$$

for a relatively large, moderate, and small scatterer or incoherent aggregate of small scatterers, respectively. Under the assumption of small spatial variation, the constant Z_0 is a term related to the derivative of the acoustic impedance in the direction of the propagating US pulse [32]. For all simulations, material dimensions were fixed at a volume of $30 \times 30 \times 30$ mm. Within that volume, 2×10^5 scatterers were pseudo-randomly positioned to allow simulation of US images with speckle patterns [33]. An example 3-D phantom material embedded with a distribution of spherical scatterers is illustrated in Figure 2.2

2.2.2 Sparse Synthetic Aperture Beamformer

A 2-D matrix array transducer was implemented using the gridded layout as shown in Figure 2.1. Each element was set to be the same size in both the lateral and elevational dimensions. Before beamforming the raw RF data, sparse synthetic apodization was performed by adjusting the receive apodization functions to account for the missing transmit elements while maintaining spatial resolution [34]. Next, 3-D delay-and-sum beamforming was applied to the simulated RF data to form the final US image reconstructions. In this approach, the expected delay is calculated from transducer element position to each pixel location on the reconstruction grid. As illustrated in Figure 2.3, the value for each pixel in the reconstruction grid is obtained by summing the signal

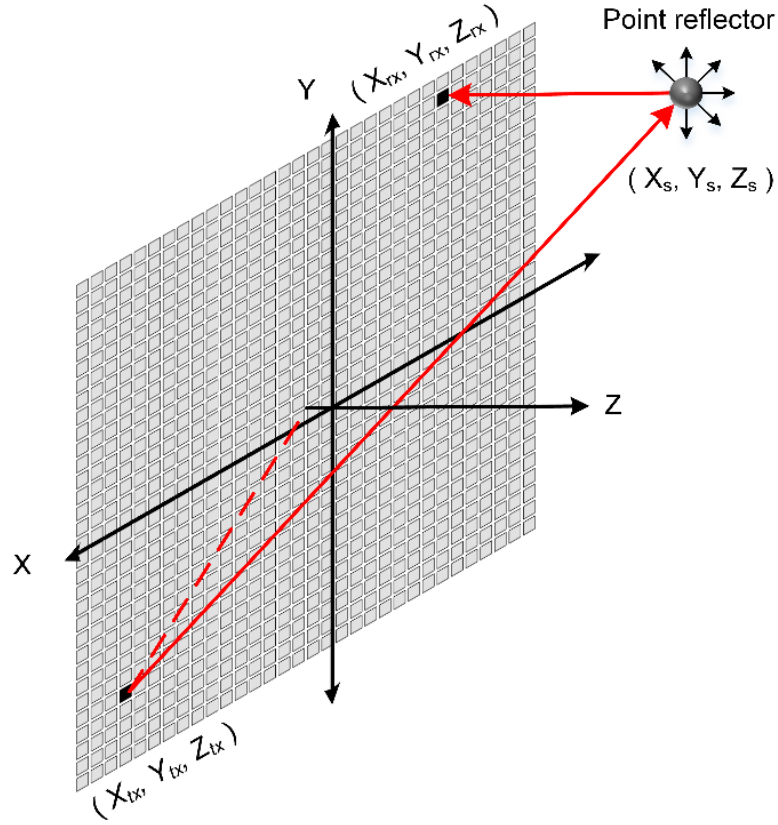


Figure 2.3. Array geometry used for processing the radio frequency US signal. By calculating the distance between the acoustic scatterer and the receive elements, the weighted delay-and-sum beamforming was performed across all depth to provide the beamformed RF data.

traces for all elements at the time delay associated with that pixel location [35]. Given the signal emitted by an arbitrary transmit element at location (X_{tx}, Y_{tx}, Z_{tx}) is h , and considering that the target function at a given point location is (X_s, Y_s, Z_s) in the spatial domain, the beamformed RF data is obtained by the following expression [36]:

$$e_{beamformed}(rx, t) = \sum_s e(t)h(t - \delta) \quad (9)$$

where $\delta = \frac{1}{c} \left[\sqrt{Z_s^2 + (X_s - X_{tx})^2 + (Y_s - Y_{tx})^2} + \sqrt{Z_s^2 + (X_s - X_{rx})^2 + (Y_s - Y_{rx})^2} \right]$ is the round-trip delay of the backscattered US signal.

2.2.1 H-scan US Imaging

Experimental studies were performed using a programmable US scanner (Vantage 256, Verasonics Inc, Kirkland, WA) equipped with a 1024-element (32×32) matrix array transducer (Vermon, Tours, France). Plane wave imaging was performed at a center frequency of 8 MHz. The 2-D matrix array was divided into 4 aperture segments as depicted in Figure 2.1. This configuration allows for direct volume scanning by electronically interrogating a ROI and acquisition of a pyramidal volume of US data. A 2-D array (termed complementary) was designed by activating all elements for transmission (1 Tx) and 4 sets of complementary sparse random apertures for reception (4 Rx) to reduce the collected data size and side lobes [37]. Thus, a total number of transmit and receive events (i.e., $1 \text{ Tx} \times 4 \text{ Rx}$) were generated to interrogate the entire volume. A map of the transmitting and receiving elements was stored as a matrix for simulation validation. Coherent spatial angular compounding was implemented by successively steering and summing overlapping plane wave transmissions using five equally spaced angles in the $\pm 20^\circ$ range. In addition, different data acquisition methods were designed to study the robustness of 3-D H-scan US imaging and potential improvement in image quality: (1) synthetic, (2) sparse, (3) random, (4) sparse complimentary (sparseComp), and (5) sparse transmit (sparseTx) apodization. By switching sub-banks, synthetic apodization was performed using a full reception with 1024 active elements for the full array transmissions, whereas sparse apodization was performed by using the same optimally selected sparse random element map in both transmission and reception, respectively. Two different sets of sparse random element maps were used for transmitting and receiving during random apodization. Using sparse elements for transmitting and sparse random aperture compounding for receiving, the sparseComp imaging scheme was designed. Finally, sparseTx was

performed using 256-element sparse random aperture for transmit while using all 1024 elements for receiving.

H-scan US image processing was applied to each backscattered US signal [38]. Gaussian bandpass functions with 256 distinct center frequencies and bandwidth of 0.02 MHz were implemented in the 5.6 to 10.4 MHz range to measure the frequency content of the received signals [39]. The signal envelope for each of the filtered and compounded data sequences were then calculated by using the Hilbert transformation. Thereafter, the best matched filter index at each voxel location was selected by finding the maximum value among the 256 different convolution results to generate the H-scan US image. A colormap scheme is used to enhance visualization, whereby the relative strength of these filter outputs was color coded where the lower frequency signals were assigned redder values and the higher frequency components were bluer. In general, lower frequency content is generated from larger scattering structures while higher frequency backscattered US signal content is generated by an US wave interacting with small scatterers at a scale below the wavelength of the US transmit pulse (i.e., Rayleigh scatterers).

2.2.2 Phantom Material Fabrication

A series of tissue-mimicking phantom materials were prepared to contain spherical US scatterers of varying size. Each phantom contained a base mixture of 75 g of gelatin (300 Bloom, Sigma Aldrich, St. Louis, MO), spherical US scatterers with diameters in the range of (1) 27 to 45 μm , (2) 63 to 75 μm , or (3) 106 to 125 μm (CoSpheric LLC, Santa Barbara, CA) at a 0.5% concentration, and 1 L of degassed water. After heating to 65 $^{\circ}\text{C}$ to promote gelatin crosslinking, the solution was poured into a solid mold and allowed to cool in a refrigerator overnight. The final material size was 30 \times 30 \times 30 mm. All phantoms were US imaged at room temperature after

solidification. Note that a calculation of the true scatterer size distribution was performed from optical microscopy images of diluted samples.

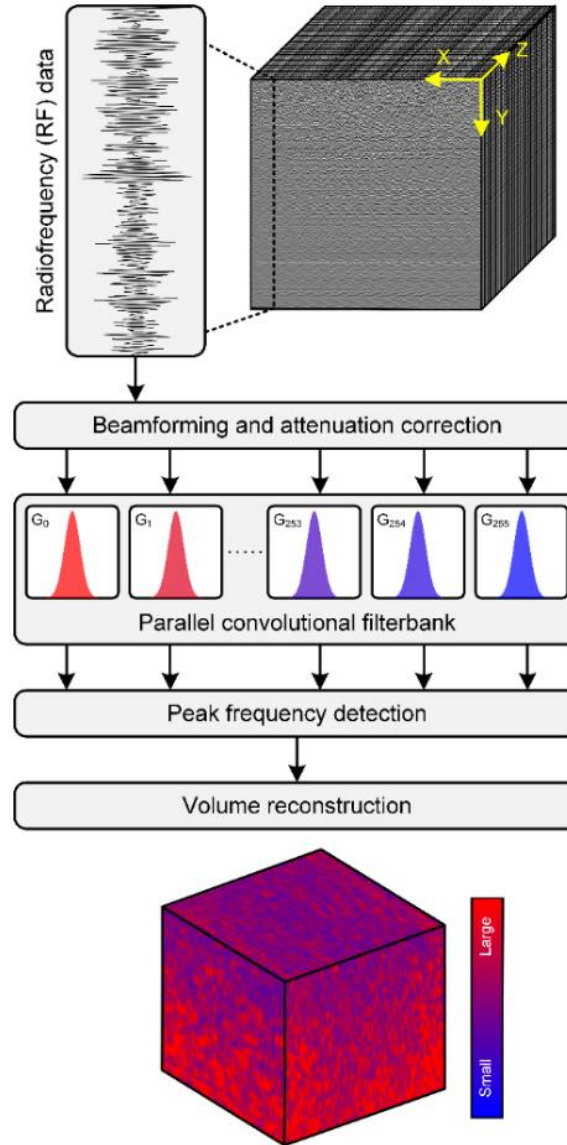


Figure 2.4. Schematic diagram highlighting the parallel processing strategy of 3-D volumetric H-scan US imaging. After local attenuation correction, a bandpass filter bank ($N = 256$) is applied to the US data for measuring relative strength of the received signals. Thereafter, an 8-bit color map is set for H-scan based on maximum matched filter output. Note that the color map is gradually shifting from red to blue as the filter index value changes from 1 to 256 (from low to high frequency). Array geometry used for processing the radio frequency US signal. By calculating the distance between the acoustic scatterer and the receive elements, the weighted delay-and-sum beamforming was performed across all depth to provide the beamformed RF data.

2.2.3 Acoustic Output Measurements

The acoustic output of the US system was measured using a calibrated hydrophone setup (AIMS III, Onda Corp, Sunnyvale, CA). The system consists of a large degassed water tank and stepper motors to precisely control hydrophone movement as it spatially records the peak negative pressure parameter from a fixed transducer. Three orthogonal planes of data were collected to form the final 3-D US beam pattern.

2.2.4 Statistical Analysis

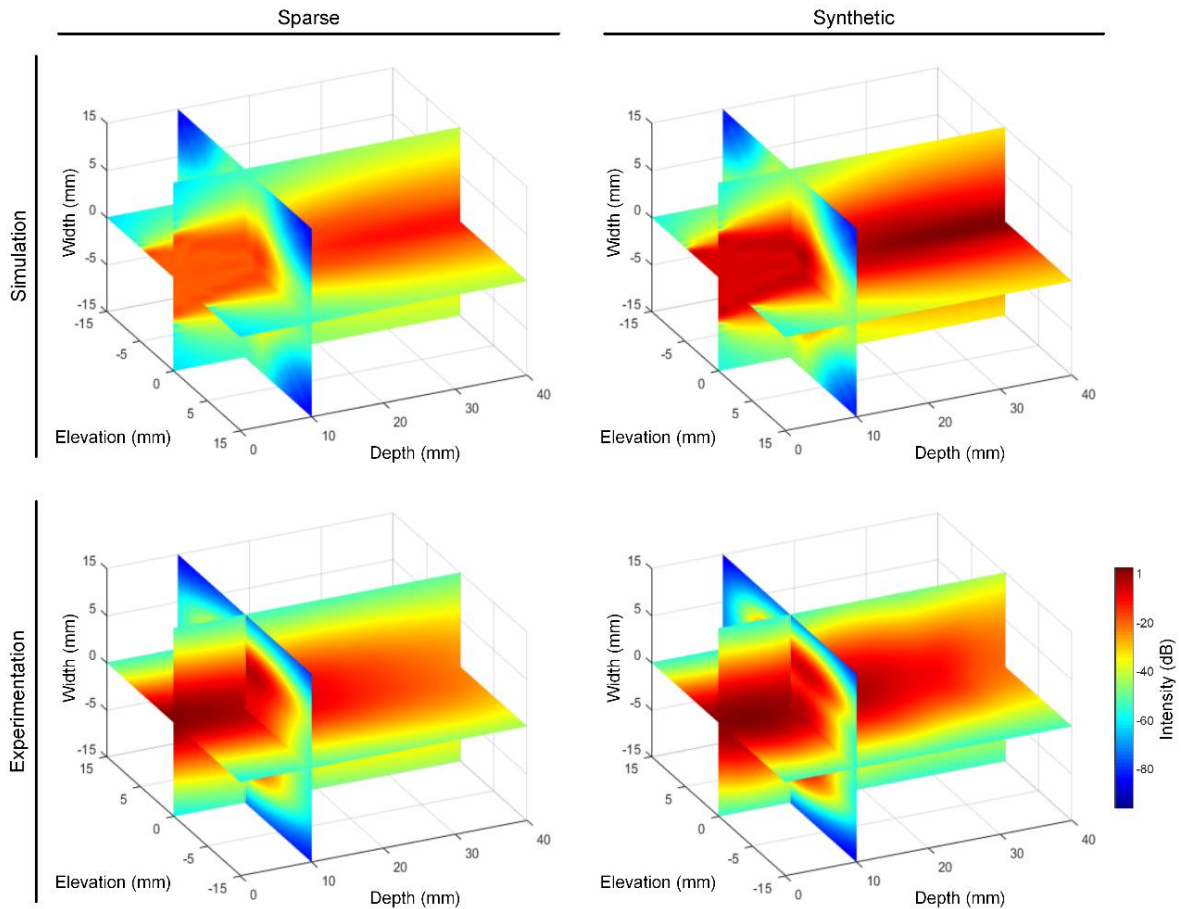


Figure 2.5. The simulated (top) and corresponding Hydrophone measured (bottom) 3-D US beam pattern from the same sparse array transmission and synthetic aperture are shown using plane wave propagation. Note that a self-defined pulse was simultaneously transmitted from 256 elements of the 2-D array. All the images are normalized to their respective maximum.

For each experimental group, US image intensity was summarized as mean \pm SD and spatial variance was measured throughout the entire volume space to evaluate the different US data acquisition approaches. The data deviation between each measurement was used to reflect robustness. To evaluate the impact of scatterer size on US image intensity, a one-way analysis of variance (ANOVA) test was performed. Any p -value less than 0.05 was considered statistically significant. All analyses were performed using Prism 9.0 (GraphPad Software, San Diego, CA).

2.3 Results

The hydrophone measured US beampattern obtained from the synthetic aperture (full flash) and 256-element sparse array transmission with the corresponding simulation result is shown in Figure 2.5. A customized system impulse with a center frequency of 8 MHz was used during the simulation to have a comparable resolution with the Vermon matrix array transducer. The comparison of simulated and experimental acoustic field also demonstrates that plane waves were successfully generated.

Acoustic scatterers were imaged using the microscope system and a set of image processing algorithms were utilized to estimate the relative size of the acoustic scatterers. These scatterer sizes were then used in the phantom simulation for validation. Note that the scatterer used in both the simulation and experiment were similarly distributed over equivalent range. The segmentation approach for quantitative measurement of acoustic scatterer size was done using digitized microscope images. After thresholding the image to identify pixels associated with scatterer location, an active contour was used for complete segmentation of each scatterer. Next, morphological operations were used to improve boundary definition. The scatterer boundaries obtained by the proposed segmentation technique were computed throughout the image. The

processed scatterers are listed in numerical order based on the calculated diameter, and the summarized diameter distribution data are shown in Figure 2.6. To simplify the procedure, the scatterer size was assumed to be Rayleigh-distributed during the acoustic phantom simulation (curve-fitting correlation value, $R^2 > 0.95$).

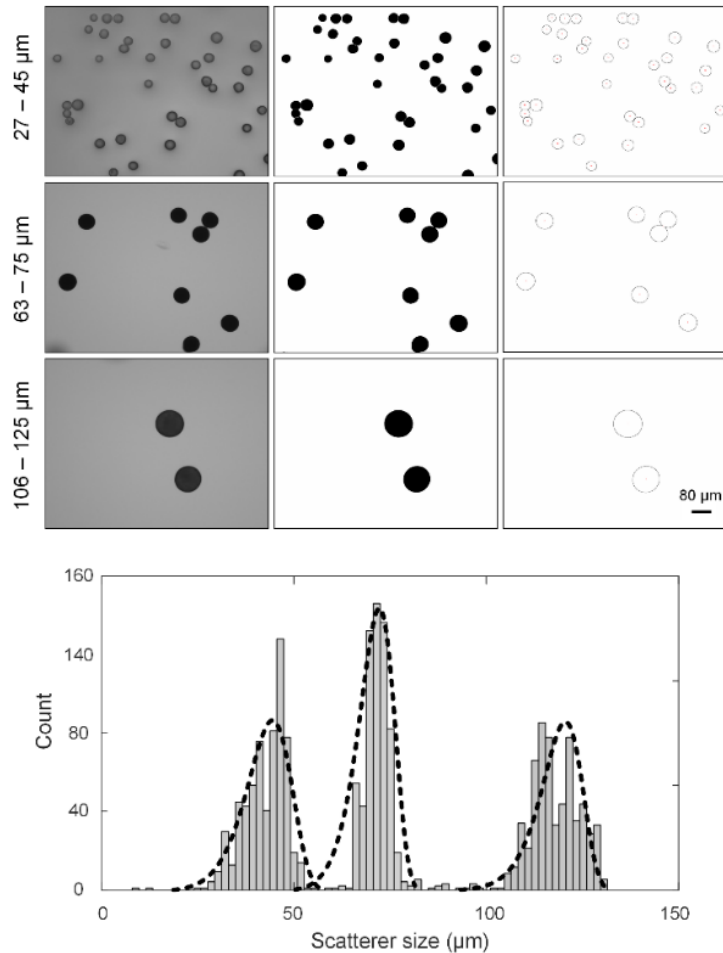


Figure 2.6. Summary of the segmentation approach for quantitative measurement of acoustic scatterer size from the digitized microscope images (RGB color format) of different sized scatterers (column 1) from relatively small (top), moderate (middle), to large (bottom). After thresholding the image to identify pixels associated with the scatterer location, an active contour used for complete segmentation of each nucleus and area measurement (column 2). Next, morphological operations are used to improve the boundary definition (right column). Note that scatterers partially located outside of the image were not considered. Statistical analysis of the size estimation of different scatterers was performed thereafter. The estimated sizes of the scatterers were $42.6 (\pm 2.6)$, $70.8 (\pm 2.2)$, and $114.8 (\pm 4.1)$ μm after curve fitting with the Rayleigh function, which helps to simplify the phantom modeling procedure in simulations.

3-D H-scan US imaging was performed to assess impact of the various apodization methods. Inspection of the reconstructed H-scan US images in Figure 2.7 reveals a subtle intergroup color variation when different apodization methods were used ($p > 0.29$). However, the proposed complimentary apodization technique demonstrated a marked lower spatial variation ($\pm 3.7 \times 10^{-3}$) versus the synthetic ($\pm 1.1 \times 10^{-1}$), sparse ($\pm 1.2 \times 10^{-1}$), random ($\pm 1.3 \times 10^{-1}$), sparseComp ($\pm 3.3 \times 10^{-2}$), and sparseTx ($\pm 3.5 \times 10^{-2}$) approaches.

Simulated B-scan and H-scan US images from phantom materials with scatterer sizes of 42.6 ± 2.6 , 70.8 ± 2.2 , and $114.8 \pm 4.1 \mu\text{m}$ are presented in Figure 2.8. These results highlight the progressive change in the backscattered US signal as the cross-sectional diameter of the scattering object increases. Analysis of this data using the convolutional filter bank reveals a progressive red color shift (whereas a diminished strength of blue) as the size of the US scatterers increases. This validates the H-scan US theory whereby the US signal from larger scatterers dominates the red channel and that from smaller scattering objects dominates the blue channel. More importantly, spatial distribution of the acoustic scatterers could be displayed and visualized throughout the entire volume space. B-scan and H-scan US images were then reconstructed using voxel-based image reconstruction. Overall, simulated results demonstrate that the proposed H-scan US imaging technique is sensitive to scatterer size.

A series of tissue-mimicking phantom materials were embedded with 27 to 45, 63 to 75, or 106 to 125 μm spherical scatterers and then used to cross validate the simulated H-scan US results. Corresponding B-scan and H-scan US images from matched orthogonal views are presented in Figure 2.8. Inspection of the results reveal that the H-scan US image intensity increases with increasing scatterer size which is not a trended observed in the B-scan US images.

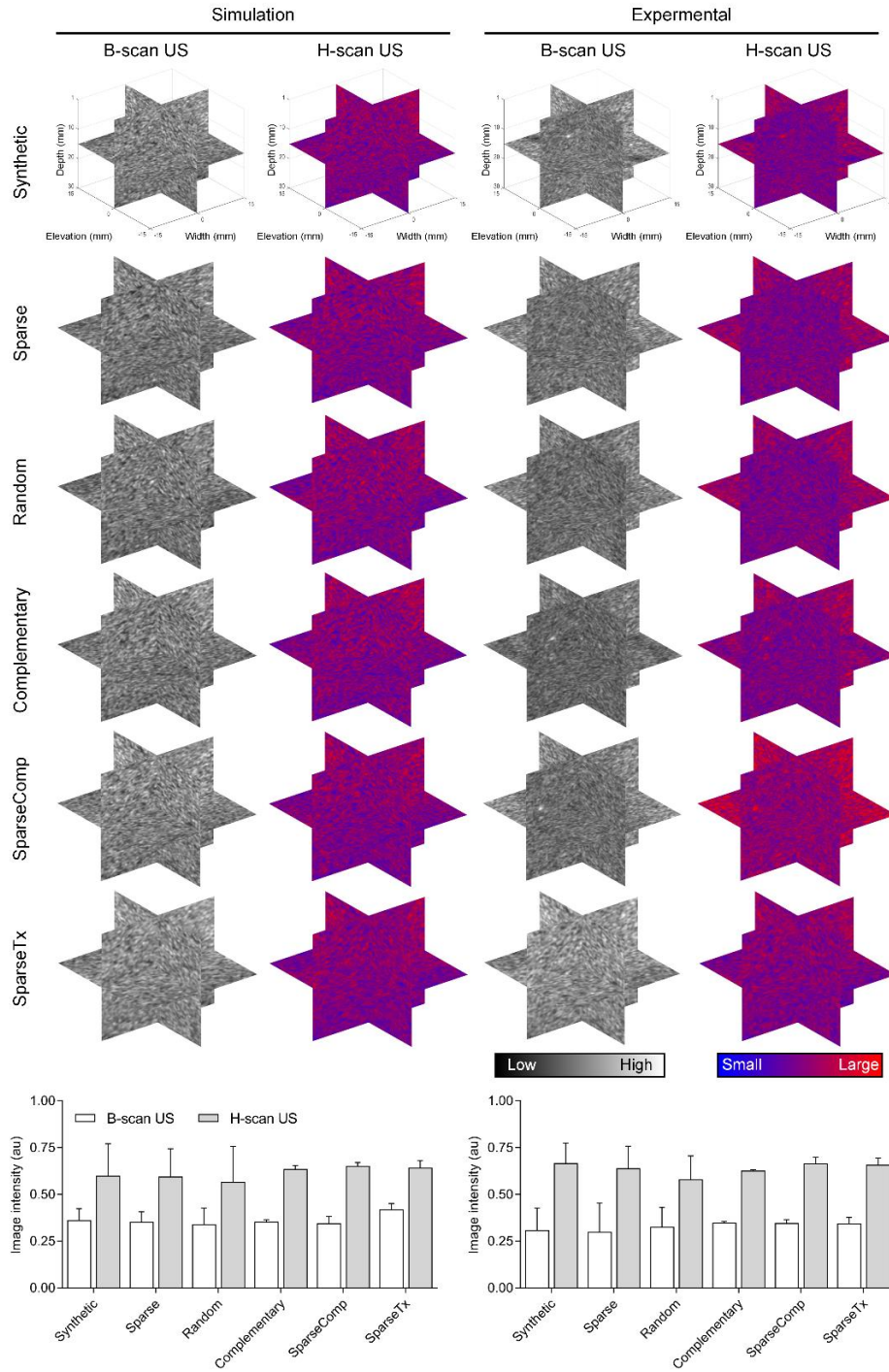


Figure 2.7. Comparison of different apodization methods with different transmission and reception strategies (A) on H-scan US imaging, namely, synthetic, sparse, random, complimentary, sparseComp, and sparseTx apodization. The H-scan US image color is consistent across all different groups and the inspection of H-scan US image intensity indicates that there is no significant difference between the 6 groups.

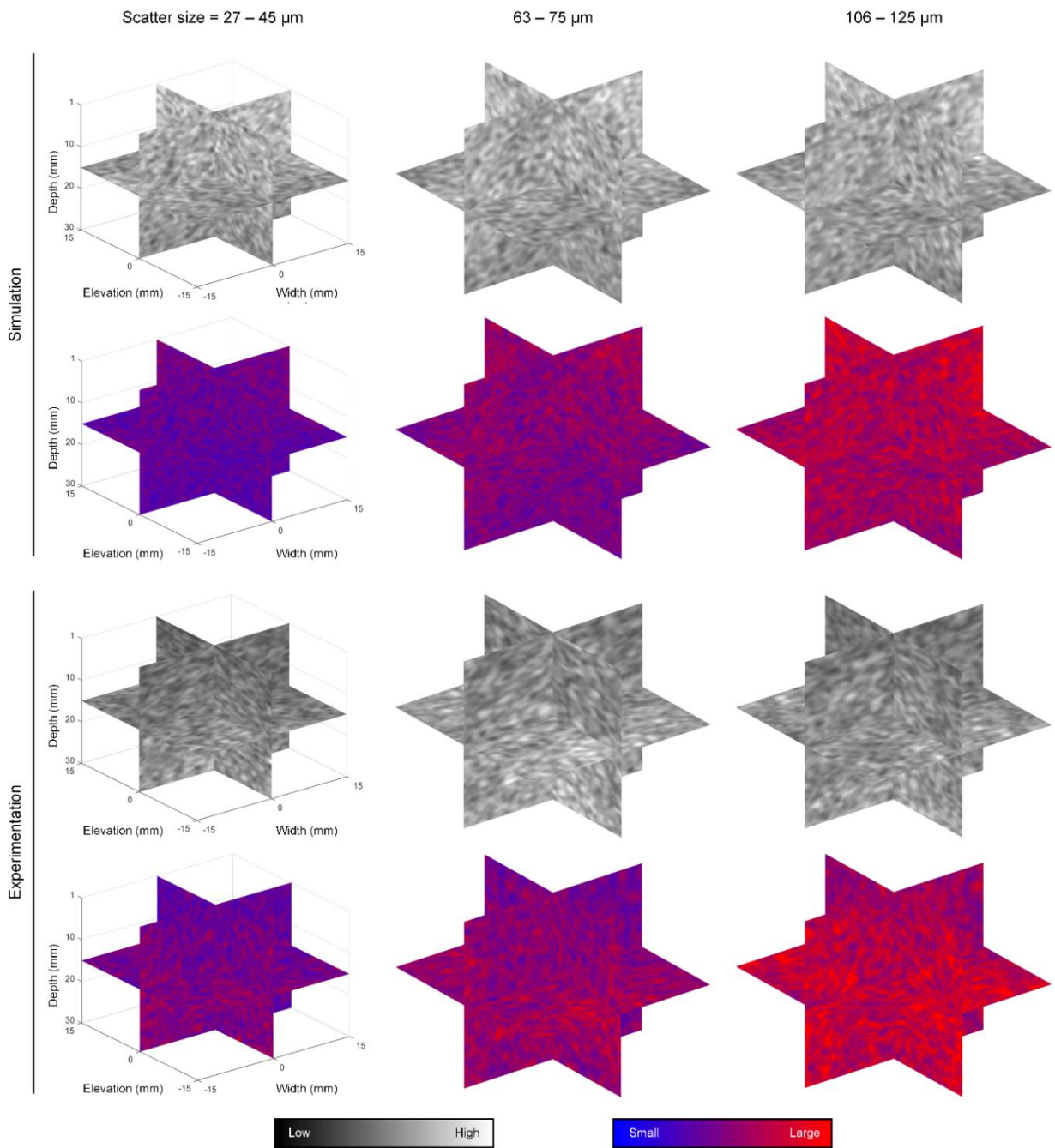


Figure 2.8. Comparison of simulated B-scan (row 1), H-scan (row 2), experimental B-scan (row 3) and H-scan (row 4) 3-D US images from a series of phantom materials containing different sized US scatterers, namely, 42.6 (± 2.6), 70.8 (± 2.2), and 114.8 (± 4.1) μm . The red hue (Lower frequency information) becomes dominant with the increase of scatterer size while the blue (Higher frequency information) diminishes.

Collectively, these results also indicate a progressive red color shift with increased US scatterer size. This again agrees with H-scan US theory whereby subtle changes in scatterer size alter the spectrum of the backscattered US signals. These expected changes can be detected by matched filters in the H-scan process.

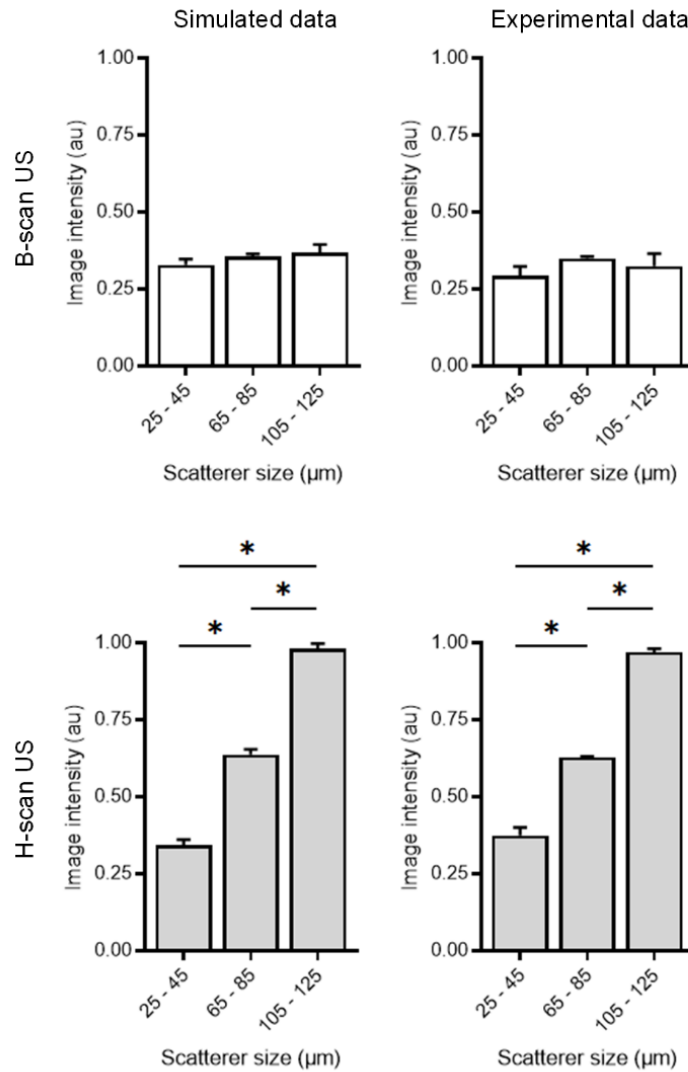


Figure 2.9. Mean image intensity from co-registered B-scan and H-scan US images collected during simulation (left) and experiment (right). Note that changes in US scatterer size have a greater impact on H-scan US images compared to B-scan US results. Repeated measurements were obtained in both simulations and experiments, then the H-scan US image intensity captured from each phantom and the corresponding simulated data was computed. * indicates $p < 0.01$

All simulated and experimental B-scan and H-scan US results were summarized as the mean image intensity and plotted as a function of US scatterer size, Figure 2.9. Note that changes in scatterer size produce relative changes in both B-scan and H-scan US images, which was consistent in both simulated and experimental data. Further inspection of this data reveals that the variation of scatterer size is better reflected in the H-scan US images compared to the matched B-scan US image ($p < 0.01$). These findings highlight the sensitivity of H-scan US imaging to changes in scatterer size and feasibility for voxel-level tissue classification.

2.4 Discussion

In this study we demonstrated improved H-scan US image quality in volume space using a matrix array transducer. Simulated H-scan US results were validated by experimental findings. Both demonstrate feasibility of using US as an imaging modality for volumetric tissue characterization. Analyzed data exhibits high correlations between experimental and simulated data for both B-scan and H-scan US imaging. Compared to previous H-scan US studies that collected cross-sectional images [40]–[42], data collected throughout the entire volume (3-D space) enables multi-planar visualization. Although US systems with matrix array transducers and use of random apertures have been well studied to reduce the number of receive data channels, this is the first time that random aperture compounding was performed for H-scan US imaging. The proposed apodization method demonstrated an improvement in image quality while maintaining high volume rates. Moreover, the proposed method provides spatial information that highlights scattering behavior among different tissue microstructures. Furthermore, the proposed 3-D H-scan imaging technology was accomplished by using a 2-D matrix array transducer and without mechanically sweeping a linear array transducer. This improvement could potentially expand the use of the H-

scan US technique when rapid processing is needed to ensure real-time imaging. Additionally, 3-D H-scan US exhibits less variance compared to planar measurements due to an increased sample size and statistical averaging.

The 2-D sparse array H-scan US imaging technique was theoretically investigated and experimentally validated. A limited number of receive pairs allow a reliable visualization in volume space, which has made 3-D H-scan US imaging with high spatiotemporal resolution possible [37]. A comparison of different acquisition techniques demonstrated that spatial variance of two complimentary random apertures affords a slight advantage (lower values) over the full array when imaging uniform phantom materials. This may be due to the presence of noise during data acquisition that is reduced by averaging the multiple random apertures. Additionally, random apertures were optimally selected from the full array using an optimization algorithm, which can potentially obtain comparable or even better image quality than with use of a larger number of transducer elements. Conversely, 3-D H-scan US images had higher spatial variance when the acquisition is performed using a sparse aperture. This is in agreement with a previous study that used the sparse-random-aperture compounding technique and found improved main-lobe-to-side-lobe ratios of 2.9 ± 0.5 and 1.5 ± 0.7 dB when compared to sparse and full aperture methods, respectively [43]. Compared to a previous H-scan US study [19], the complimentary apodization technique introduced herein can reduce the data acquisition time and achieve real-time H-scan US imaging. Random selection of transducer elements during apodization can significantly reduce the impact of grating lobes and can provide higher quality US images [44]. In another study, a fast 3-D US imaging approach with improved temporal resolution was developed using a novel image acquisition sequence [22], [45]. Multiple datasets were sequentially acquired and synchronized for

structural visualization of an *ex vivo* porcine eye at high resolution. This is one technique that can potentially improve US imaging system performance and functionality to achieve sufficiently high temporal resolution. A potential challenge is that simultaneous control of too many transducer elements using a high number of transmit-receive events would dramatically increase power consumption in addition to system and computational costs [46]. By contrast, our study was conducted by optimally selecting four sets of mutually exclusive 256-element apertures during receive events that can considerably reduce the computational burden while maintaining a sufficiently high data processing speed.

Analysis of our US data revealed that image resolution in the axial dimension was relatively high whereas in the lateral and elevational dimensions the spatial resolution was much lower. This is in part due to the missing element rows in the transducer assembly, which increases the size of the side lobes and impacts US image quality in those directions. A more advanced beamformer could help improve the existing H-scan US image quality. Sparse array design approaches (i.e., random approach, linear programming, or sparse periodic layout, etc.) can also be used to reduce grating lobes by optimally selecting the active transducer elements [47]. Alternatively, high-volume-rate 3-D US imaging can be achieved using synthetic aperture sequential beamforming with chirp-coded excitation [48]. Another limitation of our study is the number of transmit and receive events is higher than use of sparse apodization with one aperture. This led to improved image quality but at the expense of a reduced volume acquisition rate. If higher H-scan US volume acquisition rates are preferred, sparse apodization with one aperture is a logical solution. Future work will explore use of advanced element apodization and coded

excitations techniques in addition to a more complex phantom study to improve the robustness of 3-D H-scan US imaging.

2.5 Conclusion

3-D H-scan US imaging is a novel approach for voxel-level tissue characterization. It was found that H-scan US was more sensitive to changes in scatterer size than traditional B-scan US imaging. Furthermore, the proposed US method can significantly reduce the computational burden and potentially improve imaging quality, which has made tissue characterization in volumetric space possible. Overall, the research presented herein provides additional validation of H-scan US imaging and will help guide future development of this promising modality.

2.6 Acknowledgements

The authors would like to thank A. Honari, D. Merillat, S. R. Sirsi, A. Bellary, M. Jahanandish, and K. Brown for their insightful suggestions on this project and for their help with preparation of this manuscript. This research was supported in part by National Institutes of Health (NIH) grants R01DK126833 and R01EB025841 and award RP180670 from the Cancer Prevention and Research Institute of Texas (CPRIT) to establish the Small Animal Imaging Facility at The University of Texas at Dallas.

2.7 References

- [1] R. L. Siegel, K. D. Miller, and A. Jemal, “Cancer statistics, 2020,” *CA Cancer J Clin*, vol. 70, no. 1, pp. 7–30, 2020.
- [2] A. L. Coila and R. Lavarello, “Regularized spectral log difference technique for ultrasonic attenuation imaging,” *IEEE Trans Ultrason Ferroelectr Freq Control*, vol. 65, no. 3, pp. 378–389, 2018.

- [3] M. L. Oelze and J. Mamou, "Review of quantitative ultrasound: Envelope statistics and backscatter coefficient imaging and contributions to diagnostic ultrasound," *IEEE Trans Ultrason Ferroelectr Freq Control*, vol. 63, no. 2, pp. 336–351, 2016.
- [4] K. Hoyt *et al.*, "Tissue elasticity properties as biomarkers for prostate cancer," *Cancer Biomark*, vol. 4, no. 4–5, pp. 213–225, 2008.
- [5] R. M. S. Sigrist, J. Liau, A. E. Kaffas, M. C. Chammas, and J. K. Willmann, "Ultrasound elastography: Review of techniques and clinical applications," *Theranostics*, vol. 7, no. 5, pp. 1303–1329, 2017.
- [6] J.-L. Gennisson, T. Deffieux, M. Fink, and M. Tanter, "Ultrasound elastography: Principles and techniques," *Diagn Interv Imaging*, vol. 94, no. 5, pp. 487–495, 2013.
- [7] L. Basavarajappa *et al.*, "Multiparametric ultrasound imaging for the assessment of normal versus steatotic livers," *Sci Rep*, vol. 11, no. 1, p. 2655, 2021.
- [8] I. Z. Nenadic *et al.*, "Attenuation measuring ultrasound shearwave elastography and in vivo application in post-transplant liver patients," *Phys Med Biol*, vol. 62, no. 2, pp. 484–500, 2017.
- [9] N. C. Rouze, Y. Deng, C. A. Trutna, M. L. Palmeri, and K. R. Nightingale, "Characterization of viscoelastic materials using group shear wave speeds," *IEEE Trans Ultrason Ferroelectr Freq Control*, vol. 65, no. 5, pp. 780–794, 2018.
- [10] J. Baek *et al.*, "Clusters of ultrasound scattering parameters for the classification of steatotic and normal livers," *Ultrasound Med Biol*, vol. 47, no. 10, pp. 3014–3027, 2021.
- [11] K. J. Parker, "Scattering and reflection identification in H-scan images," *Phys Med Biol*, vol. 61, no. 12, pp. L20–28, 2016.
- [12] M. Khairalseed, K. Hoyt, J. Ormachea, A. Terrazas, and K. J. Parker, "H-scan sensitivity to scattering size," *J Med Imaging*, vol. 4, no. 4, p. 043501, 2017.
- [13] M. Khairalseed, K. Javed, G. Jashkaran, J.-W. Kim, K. J. Parker, and K. Hoyt, "Monitoring early breast cancer response to neoadjuvant therapy using H-scan ultrasound imaging: Preliminary preclinical results," *J Ultrasound Med*, vol. 38, no. 5, pp. 1259–1268, 2019.
- [14] G. Turashvili and E. Brogi, "Tumor heterogeneity in breast cancer," *Front Med*, vol. 4, 2017.
- [15] Z. Yin *et al.*, "Prediction of nonalcoholic fatty liver disease (NAFLD) activity score (NAS) with multiparametric hepatic magnetic resonance imaging and elastography," *Eur Radiol*, vol. 29, no. 11, pp. 5823–5831, 2019.
- [16] G. Low, S. A. Kruse, and D. J. Lomas, "General review of magnetic resonance elastography," *World J Radiol*, vol. 8, no. 1, pp. 59–72, 2016.

- [17] A. Manduca *et al.*, “MR elastography: Principles, guidelines, and terminology,” *Magn Reson Med*, vol. 85, no. 5, pp. 2377–2390, 2021.
- [18] M. Mahoney, A. Sorace, J. Warram, S. Samuel, and K. Hoyt, “Volumetric contrast-enhanced ultrasound imaging of renal perfusion,” *J Ultrasound Med*, vol. 33, no. 8, pp. 1427–1437, 2014.
- [19] H. Tai, M. Khairalseed, and K. Hoyt, “3-D H-scan ultrasound imaging and use of a convolutional neural network for scatterer size estimation,” *Ultrasound Med Biol*, vol. 46, no. 10, pp. 2810–2818, 2020.
- [20] W. Yang, A. Ingle, and T. Varghese, “Comparison of three-dimensional strain volume reconstructions using SOUPR and wobbler based acquisitions: A phantom study,” *Med Phys*, vol. 43, no. 4, p. 1615, 2016.
- [21] H. Tai, J. Song, J. Li, S. Reddy, M. Khairalseed, and K. Hoyt, “Three-dimensional H-scan ultrasound imaging of early breast cancer response to neoadjuvant therapy in a murine model,” *Invest Radiol*, vol. 57, no. 4, pp. 222–232, 2022.
- [22] J. Yu, H. Yoon, Y. M. Khalifa, and S. Y. Emelianov, “Design of a volumetric imaging sequence using a Vantage-256 ultrasound research platform multiplexed with a 1024-element fully sampled matrix array,” *IEEE Trans Ultrason Ferroelectr Freq Control*, vol. 67, no. 2, pp. 248–257, 2020.
- [23] J. Provost *et al.*, “3D ultrafast ultrasound imaging in vivo,” *Phys Med Biol*, vol. 59, no. 19, pp. 1–13, 2014.
- [24] M. Tanter and M. Fink, “Ultrafast imaging in biomedical ultrasound,” *IEEE Trans Ultrason Ferroelectr Freq Control*, vol. 61, no. 1, pp. 102–119, 2014.
- [25] B. Heiles *et al.*, “Ultrafast 3D ultrasound localization microscopy using a 32 x 32 matrix array,” *IEEE Trans Med Imag*, vol. 38, no. 9, pp. 2005–2015, 2019.
- [26] J.-L. Gennisson *et al.*, “4-D ultrafast shear-wave imaging,” *IEEE Trans Ultrason Ferroelectr Freq Control*, vol. 62, no. 6, pp. 1059–1065, 2015.
- [27] J. A. Jensen and N. B. Svendsen, “Calculation of pressure fields from arbitrarily shaped, apodized, and excited ultrasound transducers,” *IEEE Trans Ultrason Ferroelectr Freq Control*, vol. 39, no. 2, pp. 262–267, 1992.
- [28] J. A. Jensen, “A model for the propagation and scattering of ultrasound in tissue,” *J Acoust Soc Am*, vol. 89, no. 1, pp. 182–190, 1991.
- [29] M. Ueda and Y. Ozawa, “Spectral analysis of echoes for backscattering coefficient measurement,” *J Acoust Soc Am*, vol. 77, no. 1, pp. 38–47, 1985.

- [30] R. L. Romijn, J. M. Thijssen, and G. J. van Beuningen, "Estimation of scatterer size from backscattered ultrasound: A simulation study," *IEEE Trans Ultrason Ferroelectr Freq Control*, vol. 36, no. 6, pp. 593–606, 1989.
- [31] T. Tang, "The Hermite spectral method for Gaussian-type functions," *SIAM J Sci Comput*, vol. 14, no. 3, pp. 594–606, 1993.
- [32] K. J. Parker, "The H-scan format for classification of ultrasound scattering," *OMICS Journal of Radiology*, vol. 5, no. 5, pp. 1–7, 2016.
- [33] J. W. Hunt, A. E. Worthington, and A. T. Kerr, "The subtleties of ultrasound images of an ensemble of cells: Simulation from regular and more random distributions of scatterers," *Ultrasound Med Biol*, vol. 21, no. 3, pp. 329–341, 1995.
- [34] G. R. Lockwood, J. R. Talman, and S. S. Brunke, "Real-time 3-D ultrasound imaging using sparse synthetic aperture beamforming," *IEEE Trans Ultrason Ferroelectr Freq Control*, vol. 45, no. 4, pp. 980–988, 1998.
- [35] C. Ceroici, T. Harrison, and R. J. Zemp, "Fast orthogonal row-column electronic scanning with top-orthogonal-to-bottom electrode arrays," *IEEE Trans Ultrason Ferroelectr Freq Control*, vol. 64, no. 6, pp. 1009–1014, 2017.
- [36] J. Arendt, "Synthetic aperture tissue and flow ultrasound imaging," p. 334.
- [37] S. Harput *et al.*, "3-D super-resolution ultrasound imaging with a 2-D sparse array," *IEEE Trans Ultrason Ferroelectr Freq Control*, vol. 67, no. 2, pp. 269–277, 2020.
- [38] H. Tai, M. Khairalseed, and K. Hoyt, "Adaptive attenuation correction during H-scan ultrasound imaging using K-means clustering," *Ultrasonics*, vol. 102, p. 105987, 2020.
- [39] K. J. Parker and J. Baek, "Fine-tuning the H-scan for discriminating changes in tissue scatterers," *Biomed Phys Eng Express*, vol. 6, no. 4, p. 045012, 2020.
- [40] M. Khairalseed, F. Xiong, J.-W. Kim, R. F. Mattrey, K. J. Parker, and K. Hoyt, "Spatial angular compounding technique for H-scan ultrasound imaging," *Ultrasound Med Biol*, vol. 44, no. 1, pp. 267–277, 2018.
- [41] M. Khairalseed, K. Brown, K. J. Parker, and K. Hoyt, "Real-time H-scan ultrasound imaging using a Verasonics research scanner," *Ultrasonics*, vol. 94, pp. 28–36, 2019.
- [42] M. Khairalseed and K. Hoyt, "High-resolution ultrasound characterization of local scattering in cancer tissue," *Ultrasound Med Biol*, 2022.
- [43] M. Bernal, B. Cunitz, D. Rohrbach, and R. Daigle, "High-frame-rate volume imaging using sparse-random-aperture compounding," *Phys Med Biol*, vol. 65, no. 17, p. 175002, 2020.

- [44] B. Diarra, M. Robini, P. Tortoli, C. Cachard, and H. Liebgott, "Design of optimal 2-D nongrid sparse arrays for medical ultrasound," *IEEE Trans Biomed Eng*, vol. 60, no. 11, pp. 3093–3102, 2013.
- [45] Q. Chen *et al.*, "Validation of ultrasound super-resolution imaging of vasa vasorum in rabbit atherosclerotic plaques," *IEEE Trans Ultrason Ferroelectr Freq Control*, vol. 67, no. 8, pp. 1725–1729, 2020.
- [46] E. Roux, A. Ramalli, P. Tortoli, C. Cachard, M. C. Robini, and H. Liebgott, "2-D ultrasound sparse arrays multidepth radiation optimization using simulated annealing and spiral-array inspired energy functions," *IEEE Trans Ultrason Ferroelectr Freq Control*, vol. 63, no. 12, pp. 2138–2149, 2016.
- [47] J. W. Choe, O. Oralkan, and P. T. Khuri-Yakub, "Design optimization for a 2-D sparse transducer array for 3-D ultrasound imaging," *Proc IEEE Ultrason Symp*, pp. 1928–1931, 2010.
- [48] J. Zhou *et al.*, "High-volume-rate 3-D ultrasound imaging based on synthetic aperture sequential beamforming with chirp-coded excitation," *IEEE Trans Ultrason Ferroelectr Freq Control*, vol. 65, no. 8, pp. 1346–1358, 2018.

CHAPTER 3
ADAPTIVE ATTENUATION CORRECTION DURING H-SCAN ULTRASOUND
IMAGING USING K-MEANS CLUSTERING*

Authors – Haowei Tai ¹, Mawia Khairalseed ², Kenneth Hoyt ^{2*}

¹ Department of Electrical and Computer Engineering, EC 33

The University of Texas at Dallas

800 West Campbell Road

Richardson, Texas 75080-3021

² Department of Bioengineering, EC 39

The University of Texas at Dallas

800 West Campbell Road

Richardson, Texas 75080-3021

*Reproduced with permission from Tai, Haowei, Mawia Khairalseed, and Kenneth Hoyt. "Adaptive attenuation correction during H-scan ultrasound imaging using K-means clustering." *Ultrasonics* 102 (2020): 105987.

Author contribution: Haowei Tai (myself) was responsible for the experimental design, data analysis, and the manuscript preparation presented here.

The goal of this research was to develop a novel attenuation correction method based on adaptive K-means clustering. To properly isolate these signals, a lateral moving window approach applied to adaptively adjust GH filters based on the changing of RF vector spectrums. Then the signal isolated via the same filter will be combined via overlap-add technology to keep the information loss minimum. Experimental data was collected using a Verasonics 256 US scanner equipped with a L11-4v linear array transducer. *In vivo* data indicates that H-scan US imaging after adaptive attenuation correction can optimally re-scale the GH kernels and match to the changing spectrum undergoing attenuation (i.e. high frequency shift). This approach produces H-scan US images with more uniform spatial intensity and outperforms global attenuation correction strategies. Overall, this approach will improve the ability of H-scan US imaging to estimate acoustic scatterer size and will improve its clinical use for tissue characterization when imaging complex tissues.

3.1 Introduction

Ultrasound (US) imaging is a real-time and low-cost imaging modality with minimal health risks, which has made it one of the most frequently used clinical imaging method (Jensen 2007; Wells Peter N. T. and Liang Hai-Dong 2011). To monitor subtle size changes among tumor cells, a new US-based technology has been proposed to classify the tissue scatterers responsible for echo signal generation [3], [4]. Termed H-scan US Imaging (where the ‘H’ stands for ‘Hermite’), this imaging approach links the mathematics of Gaussian-weighted Hermite polynomials (GH) to the physics of scattering and reflection from different tissue structures within a standard convolutional model of US pulse-echo systems [5]. The 2nd and 8th order GH polynomials have been used to reduce spectral overlap (correlation) and achieve improved imaging results. This allows H-scan US imaging and tissue characterization based on finding relationships between GH polynomials and backscattered US signals from different scattering structures [6]–[10].

One limitation of the current H-scan US imaging method is that it cannot compensate for frequency dependent attenuation, which can diminish the image quality and its ability of tissue characterization when imaging deep tissue [8]. A number of studies have been done to address the frequency dependent attenuation. [11] proposed a comprehensive correction method to measure and eliminate the effect of attenuation based on the Fourier transform of the tissue motion. But they need robust wave generation with the acoustic radiation force beam and motion detection methods to track waves that could be affected by phase aberration and attenuation in the first case. [12] reported favorable attenuation correction achievements in their study by investigating and comparing the reference US pulse received from a hydrophone with the attenuated signal. But their approach needs a complicated signal analysis to control the gain. Although the proposed histogram

equalization for image processing can be used as an alternative to attenuation compensation, the quantification of image intensity based on this approach still needs to be validated [13]. While the techniques presented in the abovementioned three studies have shown improvements in attenuation correction, they were all developed based on traditional B-mode US images. As introduced previously, H-scan US imaging involves different ordered GH kernels to isolate echoes to classify and visualize major scattering classes, which complicates these attenuation correction techniques. For example, the US information isolated by higher order of GH kernels are attenuated more than that at the fundamental frequency. Therefore, an accurate adaptive attenuation compensation technique is of major importance. Besides, frequency attenuation cannot be addressed by simply increasing signal amplitude. According to H-scan US imaging theory, the center frequency of GH functions should be centered at the low and high-frequency of raw radio frequency (RF) signal to properly isolate backscatter signals [14]. A progressive loss of high-frequency information in RF signal has been observed [15], which leads to spectra changes during propagation. This made the isolation of signals problematic, especially higher frequency signals reflected from small scatterers. Hence, the corresponding H-scan US image quality will be reduced because of attenuation [16].

To improve the robustness and reliability of H-scan US imaging method for tissue characterization across different organs in lateral direction, a compensation strategy by using adaptive K-means clustering algorithm is proposed in this paper to adjust GH polynomials based on RF signal spectra changes at different depth. In this method, the RF signal was segmented via a region-of-interest (ROI) window and then the RF components were sequentially analyzed to adjust the matched GH functions to account for frequency dependent attenuation. The low- and

high-frequency US information are then isolated via these GH kernels to strengthen its acoustic scatterer classification ability. Thus this research may increase the ability of tissue characterization of H-scan US imaging and its clinical potential for imaging complex tissue structures and deep organs.

3.2 Theory

3.2.1 H-scan US Imaging Method

There are three types of acoustic scattering objects that could be assumed to have small spatial variations in medium density and compressibility in H-scan US imaging technology. The concept has been well explained in [5], [17], [18]. In H-scan imaging, the receiving signals from larger, smaller, and Rayleigh scatterers could be classified by their correlation to GH_4 , GH_5 and GH_6 after normalization by the signal energy \sqrt{E} . In order to minimize the overlapping spectra [19], GH_5 and GH_6 are replaced by GH_2 and GH_8 to achieve a better frequency recognition.

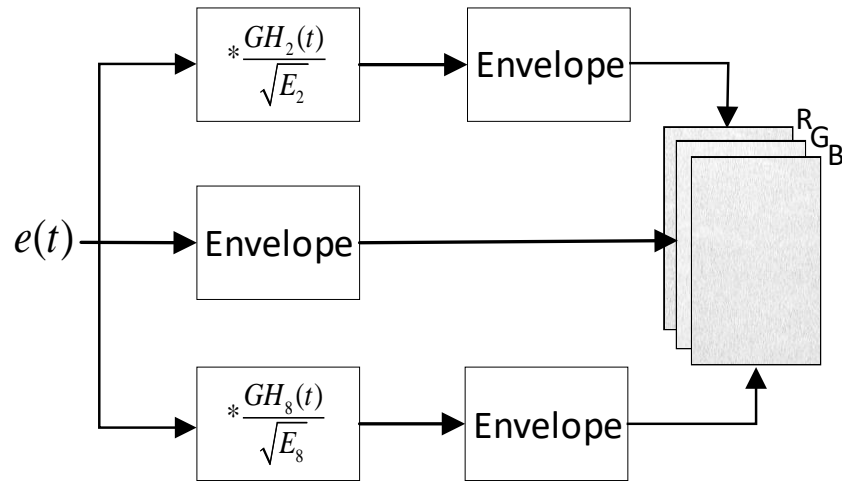


Figure 3.1. An overview of H-scan US imaging technology, where normalized GH_2 and GH_8 are used as two kernels to isolate the low- and high-frequency information in echo signal $e(t)$, respectively. The low-frequency information is then color mapped as the red and the high-frequency information as the blue. A final RGB H-scan US image is the result of using the red and blue channels along with the B mode image as the green channel to increase its image resolution.

With the increase of the order of GH functions, its corresponding central frequency increases. Since smaller scatterer clusters have high frequency US echo, GH₂ function is used as a low-frequency kernel and GH₈ function is performed as high-frequency kernel to isolate low and high-frequency information and then color map these information as red and blue, respectively, in an RGB image (Figure 3.1).

3.2.2 Adaptive K-means Clustering

K-means clustering is an unsupervised machine learning algorithm, which enables the clustering of a dataset into K groups in which each data point belongs to one group with the nearest distance. This is a prototype of the clustering method [20], [21], and then the new centers will be iteratively calculated via items in the same group. This procedure ends when the centers stop moving [22]–[24]. Using adaptive K-means clustering as an objective measure of the low- and high-frequency centers of backscattered echo signals at tissue depth, the GH polynomials can be re-scaled and shift its central frequency to fit different RF signal spectra to reduce the impact of attenuation on the quality of H-scan US image. Given a data X with m samples, thus the data can be modeled as follows [25]:

$$X = (x_1, x_2, x_3 \dots x_m) \quad (1)$$

The clustering is done by minimizing the sum of distances between items and the corresponding centroid of the groups. The distance between items could be calculated as:

$$D_{i,j} = \sum_{i=1}^m \sum_{j=1}^k (\|x_i - C_j\|) \quad (2)$$

where $D_{i,j}$ is the distance between i^{th} items and the j^{th} center. Given the set of centers $C = \{c_1, c_2, c_3 \dots c_k\}$, there are m items that need to be clustered into K groups. The center in each group could be calculated as:

$$C_j = \frac{\sum_{x \in C_j} X}{N(x_i \in C_j)} \quad (3)$$

Where $\sum_{x \in C_j} X$ represents the summation of all data items in j^{th} cluster and $N(x_i \in C_j)$ is the corresponding sample size in that cluster.

After comparing the distance with each center, items will be clustered in the nearest group with the smallest distance. The same process is done iteratively to update centers of the clusters and group the items in a new cluster. When the centers of the clusters become fixed, the K-means clustering iteration loop will stop. Thus the value of the center and its corresponding items can be obtained, which can be represented as:

$$\min \sum_{i=1}^m \sum_{j=1}^k (\|x_i - C_j\|) \quad (4)$$

3.2.3 GH Function Adjusting Strategy

Hermite functions were defined by Pierre-Simon Laplace in 1810 [26] and the n^{th} order Hermite polynomials can be modeled by:

$$H_n(t) = (-1)^n e^{t^2} \frac{d^n}{dt^n} G(t) \quad (5)$$

$$n = 0, 1, 2, \dots; -\infty < t < \infty.$$

where $\frac{d^n}{dt^n} G(t)$ is the n^{th} order of derivative for a Gaussian pulse $G(t) = e^{-t^2}$. To simulate the US pulse, $G(t)$ is used to weight the Hermite functions which also could be used as bandpass filters

to correlate frequency information in US echo pulse. Thus, according to H-scan US imaging theory (Figure 3.2), US signals reflected from large and small acoustic scatterers could be modeled as:

$$e_L(t) = A_L(d) \frac{\Delta Z}{2Z} GH_2(t)(t - t_o) \quad (6)$$

$$e_S(t) = A_S(d) \frac{\Delta Z}{2Z} GH_8(t)(t - t_o) \quad (7)$$

respectively, where $A(d)$ is the signal attenuation as a function of depth d , $\frac{\Delta Z}{2Z}(t - t_o)$ denotes the acoustic impedance and t_o is the time delay.

To isolate frequency information properly, the GH frequency centers need to be adjusted based on a particular RF signal spectrum. The Fourier transform (FT) of GH_2 was defined as (without considering the sampling frequency for simplicity):

$$\mathcal{F}[GH_2(\omega)] = \frac{e^{-\frac{1}{4}\omega^2} \omega^2}{\sqrt{2}} \quad (8)$$

so the shifting of GH_2 in the frequency domain can be modeled as:

$$a \cdot GH_2(t) = \mathcal{F}^{-1}\left[\frac{e^{-\frac{1}{4}(\omega-\omega_a)^2} (\omega - \omega_a)^2}{\sqrt{2}}\right] \quad (9)$$

where $a = \|e^{i\omega_a}\|$ could be regarded as scaling factor of GH_2 and $\frac{1}{2}\sum(\omega_a)$ is an arbitrary low-frequency center of C that could be calculated via (3). By doing so, the spectrum of GH_2 could move by a constant value of ω_a in the frequency domain, which makes the adjustment of GH functions possible via adaptive K-means clustering algorithm. We also generalized the Fourier transform for 8^{th} order of GH functions:

$$b \cdot GH_8(t) = \xi^{-1} \left[\frac{e^{-\frac{1}{4}(\omega - \omega_b)^2} (\omega - \omega_b)^8}{\sqrt{2}} \right] \quad (10)$$

where $b = \|e^{i\omega_b}\|$ could be used as scaling factor of GH_8 and $\frac{1}{2}\sum(\omega_b)$ is an arbitrary high-frequency center C calculated via adaptive K-means clustering algorithm.

According to this theory, the center frequency of both GH_2 and GH_8 are increasing when increase of scaling factor value (Figure 3.3). When GH_2 and GH_8 are scaled to fit within the RF spectrum at different depths, the low- and high-frequency signals (corresponding to different ROIs) are isolated by these kernels and combined together, respectively, via the overlap-add method. (Crochiere 1980; Charpentier and Stella 1986; Raki et al. 2005). Attenuation values were calculated by measuring the kernel center frequency shift at different depths [4]. These attenuation values were compared with an expected attenuation value of 0.3 dB/cm/MHz as defined by [29] for beef skeletal muscle tissue, Table 3.1.

3.3 Methodology

3.3.1 Ultrasound Data Acquisition

Ultrasound data was acquired using a Vantage 256 programmable scanner equipped with a 128-element L11-4 v linear array transducer (Verasonics Inc., Kirkland, WA, USA) for off-line processing. Plane wave imaging was performed at a center frequency of 5.2 MHz and backscattered raw RF data was quantized at sampling rate of 20.4 MHz after beamforming. For spatial angular compounding, successively steered and overlapping plane wave transmissions were performed using five equally spaced angles in the range of $\pm 18^\circ$ [8]. To increase the image intensity, we applied a power-law transformation ($\gamma = 0.3$).

3.3.2 Materials

The *in vivo* H-scan US data was acquired by imaging a commercially available beef chunk (length \times width \times depth of 20 cm \times 20 cm \times 10 cm. This beef chunk contains muscle tissue and the imaging depth was about 4.4 cm.

3.3.3 Statistical Analysis

The H-scan US image intensity of each channel was summarized as the mean \pm SD. All statistical measurements were performed from the mean of individual R, G or B channel components at particular position and the variance between multiple measurements was used to assess the reproducibility and robustness of the data. To evaluate any improvement in H-scan US image intensity from adaptive attenuation correction before and after power-law transformation, a two-way analysis of variance (ANOVA) test without replication was performed to analyze 20 images collected from US system. Any *p*-value less than 0.05 was considered statistically significant.

3.4 Results

The energy associated with the magnitude of RF data in Figure 3.2A is reducing with distance travelled (from left to right) caused by attenuation. Then it was equally subdivided to different region of interest (ROI) windows. The RF components in I^{st} and last ROI windows are regarded as the representative shallow and deep part of RF data, respectively. To know the impact of frequency-dependent attenuation on signal spectra, the frequency spectrum of the RF data was analyzed and compared. The result in Figure 3.2B shows that the RF signal was significantly attenuated along the lateral direction. There is a greater change in the high-frequency parts (right side of the peak) of the RF spectrums compared to their low-frequency parts (left side of the peak).

The spectra analysis of low-(color-coded as red) and high-frequency (color-coded as blue) signal of shallow part of RF signal in Figure 3.2C shows the amplitude of both signal is high and their centers are approximately located at the centers of RF signal. However, Figure 3.2D illustrates that the higher-frequency signal isolated by GH₈ kernel is noticeably reduced within the deeper ROI windows due to attenuation effects and corresponding spectral changes. In contrast, the amplitude of lower-frequency signal remains approximately unchanged.

To properly isolate frequency information, the GH functions have to be adjusted based on the RF frequency spectra. Figure 3.3 shows the effect of scaling factor on GH₂ and GH₈ kernels in time and frequency, respectively. As shown in Figure 3.3B and 3.3D, the center frequency of both GH₂ and GH₈ increases with increasing of scaling factor. And their corresponding signal in time domain becomes narrower.

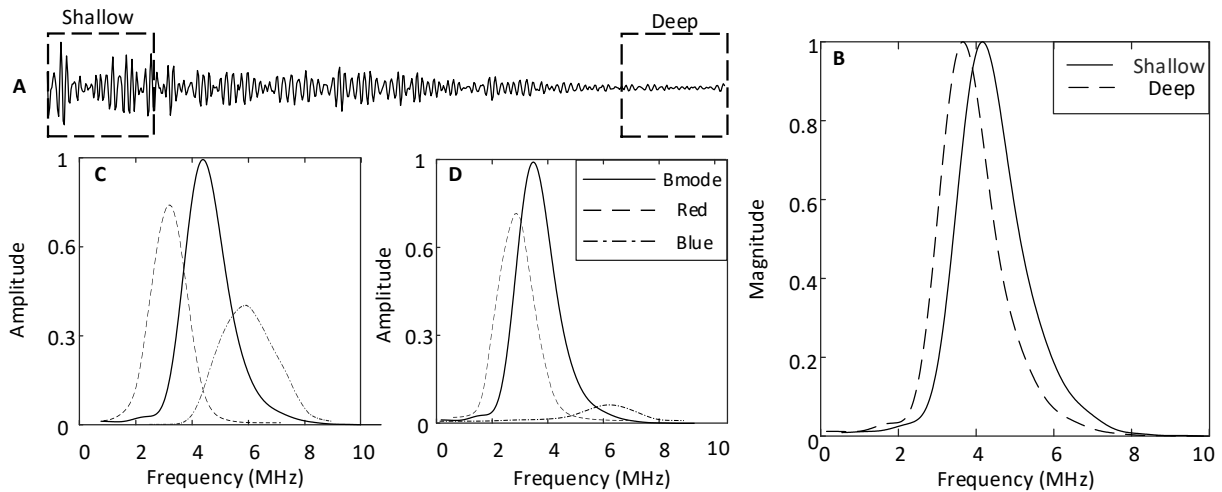


Figure 3.2. The raw RF signal and the frequency spectrum of low and high-frequency information isolated at different ROI windows, (A) RF signal collected from US imaging system. (B) Periodogram spectrum of RF signal in shallow and deep ROI window. The RF signal spectra changes especially its high-frequency information on lateral direction. (C) Frequency spectrum of the RF signal from the shallow ROI and its corresponding low- and high-frequency information isolated via GH₂ and GH₈ color mapped as red and blue, respectively (D) Frequency spectrum of the RF signal from the deep ROI and its corresponding red and blue signal information.

The signal frequency centers at different depths were found using adaptive K-mean clustering algorithm (Figure 3.4A). Then guided by these centers, the corresponding scaling factors are calculated to re-scale GH kernels and its evolution functions through deeper tissue to isolate frequency information. Figure 3.4B shows the signal spectra of red and blue channels of the last ROI isolated via adjusted GH_2 and GH_8 kernels. The high-frequency signal amplitude was 3 times

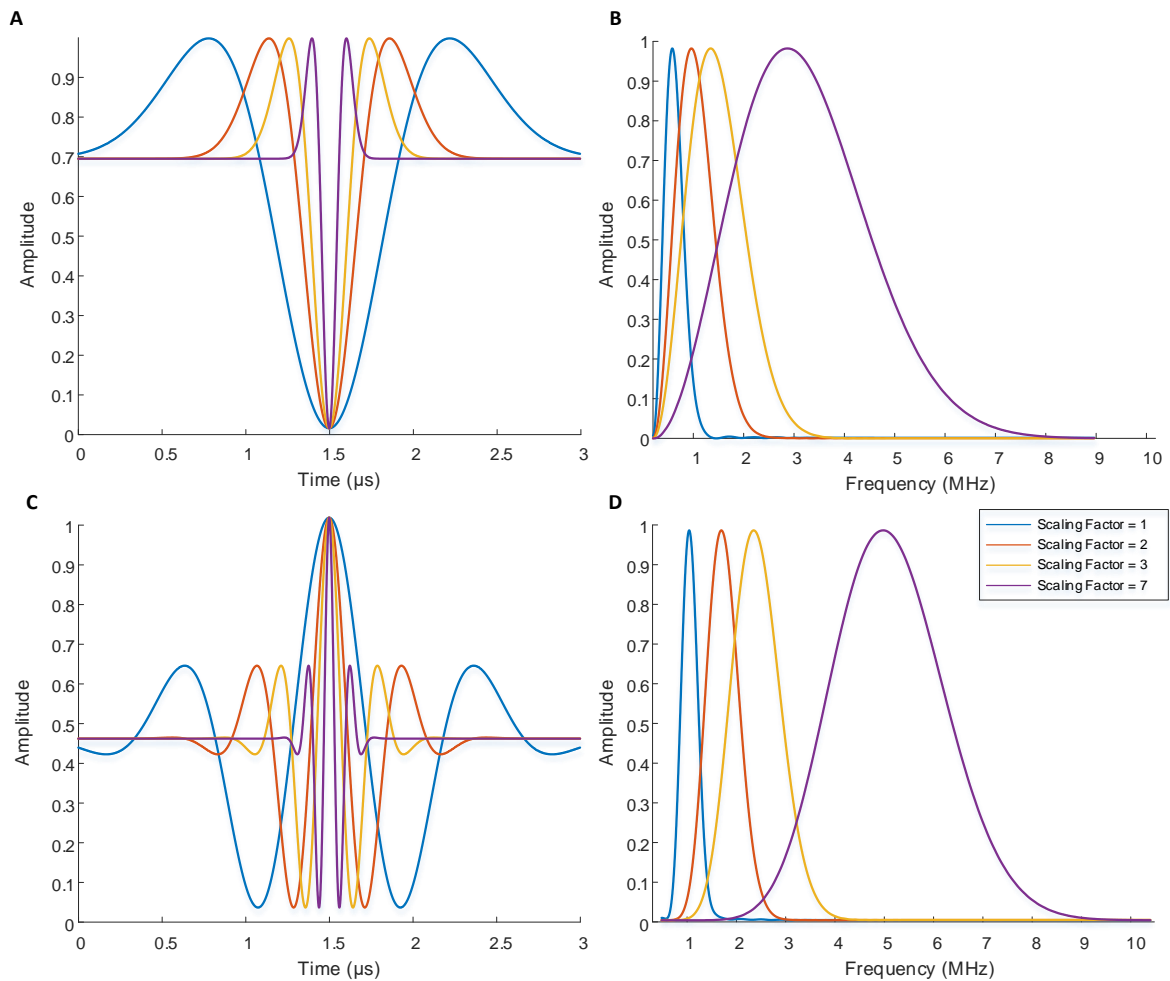


Figure 3.3. The initial pulses of GH_2 and GH_8 with the impact of different scaling factors on them. (A) The GH_2 kernel for different factors (1, 2, 3 and 7) in time domain. (B) The frequency spectra of GH_2 for different scaling factors. The center frequency of the kernel moving towards higher frequencies with the increase of scaling factor. (C) The GH_8 kernel for the same scaling factors in time domain. (D) The corresponding frequency spectra for GH_8 functions scaled via different scaling factors. The center frequency of GH_8 kernels increases if we increase the scaling factor.

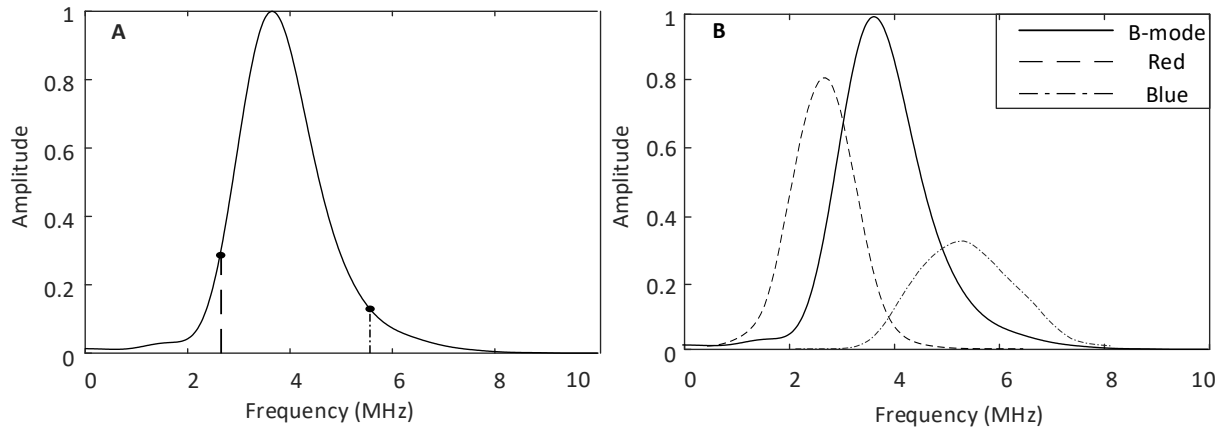


Figure 3.4. The centers of low- and high-frequency kernels in RF signal spectrum calculated via adaptive K-means clustering algorithm. (A) The spectrum of RF signal in deep ROI window, and the low and high-frequency centers calculated via adaptive K-means clustering. (B) The spectrum of low and high-frequency information (color mapped as red and blue, respectively) isolated by re-scaled GH_2 and GH_8 kernels.

higher, which means the adjusted GH functions were properly scaled and were able to isolate low and high-frequency information.

The *in vivo* H-scan US image data suggests that the deep ROI is relatively darker and the higher frequency information is increasingly attenuated (Figure 3.5A), which causes a decrease in the image intensity along the lateral direction. Compared to the shallow ROI (marked as orange), the image intensity at deep ROI (marked as dash blue) is 32.8% lower in Figure 3.5A. The analysis

Table 3.1. Attenuation parameter (dB/cm/MHz) calculated using adaptive K-means clustering algorithm for different order of GH functions with/without power-law correction at different depths.

		Depth (mm)				Average \pm SD
		10	20	30	40	
Before Power- law	GH_2	0.258	0.265	0.274	0.282	0.27 \pm 0.01
	GH_8	0.264	0.276	0.285	0.295	0.28 \pm 0.013
After Power- Law	GH_2	0.241	0.243	0.250	0.257	0.25 \pm 0.007
	GH_8	0.267	0.275	0.285	0.294	0.28 \pm 0.011

of GH frequency center after adjustment account for attenuation was reported in Table 3.1 which shows that the low-frequency attenuation parameter is 0.27 dB/MHz and 0.29 dB/MHz for the high-frequency attenuation parameter at deep ROI is calculated. This can also be seen from its corresponding H-scan US signal, where the signal amplitude is more uniform than the H-scan US signal in Figure 3.5A.

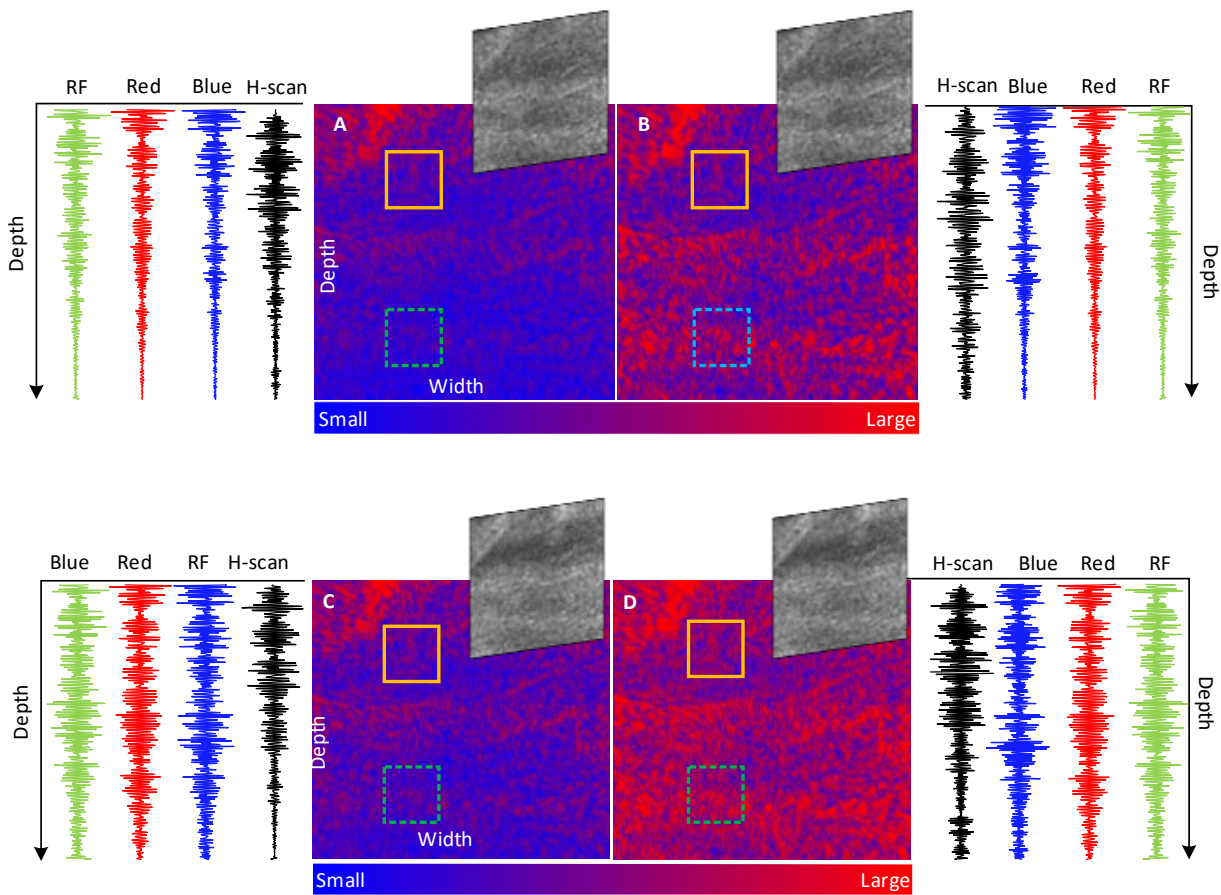


Figure 3.5. The H-scan US images before and after frequency-dependent attenuation correction, the RF signals and the co-registered B-scan US images are provided for comparison (A) H-scan US image and its corresponding B mode image where the attenuation in the lateral direction (i.e. depth) is visible in the H-scan image as well as the RF signals. (B) Attenuation corrected H-scan US image. The image intensity is noticeably increased especially at deep part of the image. (C) H-scan US image with power-law transformation ($\gamma = 0.3$). (D) Attenuation corrected H-scan US image with power-law transformation. Image widths and depths are 30 and 44 mm, respectively. Note the uniform intensity of attenuation corrected H-scan US images. This trend also be observed in the cosigned H-scan US signal, especially when imaging depth is greater than 25mm.

The H-scan US images in Figure 3.5C and 3.5D are reconstructed by using RF data processed via power-law transformation. The image at its deep ROI is brighter in Figure 3.5C according to the co-registered B-mode image, but the mean of H-scan US image intensity is still 29.7% lower than shallow ROI. The H-scan US image shown in Figure 3.5C and 3.5D demonstrate that the frequency-dependent attenuation cannot be addressed via power-law transformation.

Attenuation measurement of the corrected H-scan US signal in Table 3.1 shows that the proposed method calculated 0.25 dB/cm/MHz for the low-frequency attenuation parameter and high-frequency attenuation parameter is 0.29 dB/cm/MHz at deep ROI. This further demonstrated that the frequency dependent attenuation cannot be addressed by increase image intensity. By adjusting GH kernels can make the H-scan US image more uniform, the improvements are more pronounced in Figure 3.6. The comparison of image intensity at deep ROIs show that the attenuation corrected H-scan US imaging made a statistically significant improvement compared to current H-scan US imaging method ($p < 0.02$).

3.4 Discussion

The analysis of *in vivo* data evaluated the feasibility of the proposed adaptive attenuation correction H-scan US imaging. The H-scan US image exhibits a uniform intensity at all depths after attenuation correction since the value of attenuation is corrected by our approach. To compare with other attenuation correction studies, this research simplified the attenuation approach by using machine learning algorithm to adjust GH kernels.

Compared to the work mentioned previously, our approach has two advantages. First, our method addresses an attenuation problem associated with H-scan US imaging. H-scan US imaging can increase contrast between different sized scatterers as compared to traditional B-mode

imaging, making H-scan a superior technique for tissue characterization, especially for deep tissues. This is a promising technique to compensate heterogeneous tissue attenuation and make tissue characterization adaptive for different patients. Second, the use of an unsupervised machine learning algorithm can increase the accuracy of the frequency calculation at a lower computational cost compared to the study performed by [30], and it can efficiently adjust GH kernels to fit changes in the RF signal spectrum. Compared to other scatterer size estimation approaches that involve calculating the correlation between a mathematically-designed theoretical and an acquired backscattered US signal [31], H-scan US format for tissue characterization is a more simplistic method.

But this research still need more future works to be done, such as even though the color shift of the H-scan US images has been demonstrated when imaging different sized scatterers, the mapping of scatterer size to H-scan US image is still not studied. Therefore, one of the directions for future work is to strengthen its ability on scatterer size estimation by combining with other methods, such as machine learning or deep convolutional neural networks. Our approach was performed using a standard linear array transducer and needs to be validated on different imaging probes to improve the possibility of widespread clinical use.

The imaging of complex tissue structures was not included in this study. When imaging heterogeneous tissue, RF signals received by different elements have to be analyzed to achieve high computation accuracy as compared to the case where homogeneous tissue is being considered, and RF data from few elements are sufficient. However, this will increase the computational costs and further reduce the efficiency of the adaptive attenuation correction algorithm. Hence, future work should improve the attenuation correction method to address the

complexity of imaging deep tissue structures *in vivo*. This would further help to study and possibly reduce the impact of other factors on color shift, such as the concentration of cells.

3.6 Conclusion

Attenuation correction of H-scan US imaging was proposed as a novel US-based imaging method to address the frequency-dependent attenuation of H-scan US imaging technology. This method uses adaptive K-means clustering algorithm to re-scale the GH polynomials at different depths, which can adjust its frequency centers to adaptively fit RF spectra changes. Preliminary *in vivo* results suggest that the proposed method can properly adjust the GH kernels to account for frequency dependent attenuation, which leads to formation of an H-scan US image with more uniform brightness. Hence, attenuation correction H-scan US imaging method holds a promise to enhance the ability of tissue characterization at deep tissue using H-scan US imaging technology. An improved reliability of H-scan US imaging modality may eventually enable the imaging of complex tissue at depth to monitor the tumor response to therapy at an early stage.

3.7 Acknowledgements

This work was supported in part by NIH grants K25EB017222, R21CA212851, R01EB025841 and Texas CPRIT award RR150010.

3.8 References

- [1] J. A. Jensen, "Medical ultrasound imaging," *Prog. Biophys. Mol. Biol.*, vol. 93, no. 1, pp. 153–165, Jan. 2007.
- [2] Wells Peter N. T. and Liang Hai-Dong, "Medical ultrasound: imaging of soft tissue strain and elasticity," *J. R. Soc. Interface*, vol. 8, no. 64, pp. 1521–1549, Nov. 2011.

- [3] R. Kuc, "Clinical Application of an Ultrasound Attenuation Coefficient Estimation Technique for Liver Pathology Characterization," *IEEE Trans. Biomed. Eng.*, vol. BME-27, no. 6, pp. 312–319, Jun. 1980.
- [4] B. J. Oosterveld, J. M. Thijssen, P. C. Hartman, R. L. Romijn, and G. J. E. Rosenbusch, "Ultrasound attenuation and texture analysis of diffuse liver disease: methods and preliminary results," *Phys. Med. Biol.*, vol. 36, no. 8, p. 1039, 1991.
- [5] K. Parker, "The H-scan format for classification of ultrasound scattering," in *2017 IEEE International Ultrasonics Symposium (IUS)*, Sep. 2017, pp. 1–1.
- [6] G. R. Ge *et al.*, "H-scan analysis of thyroid lesions," *J. Med. Imaging*, vol. 5, no. 1, p. 013505, Feb. 2018.
- [7] M. Khairalseed, F. Xiong, R. Mattrey, K. Parker, and K. Hoyt, "Detection of early tumor response to abraxane using H-scan imaging: Preliminary results in a small animal model of breast cancer," in *2017 IEEE International Ultrasonics Symposium (IUS)*, Sep. 2017, pp. 1–4.
- [8] M. Khairalseed, F. Xiong, J.-W. Kim, R. F. Mattrey, K. J. Parker, and K. Hoyt, "Spatial Angular Compounding Technique for H-Scan Ultrasound Imaging," *Ultrasound Med. Biol.*, vol. 44, no. 1, pp. 267–277, Jan. 2018.
- [9] M. Khairalseed, K. Brown, K. J. Parker, and K. Hoyt, "Real-time H-scan ultrasound imaging using a Verasonics research scanner," *Ultrasonics*, vol. 94, pp. 28–36, Apr. 2019.
- [10] M. Khairalseed, K. Javed, G. Jashkaran, J.-W. Kim, K. J. Parker, and K. Hoyt, "Monitoring Early Breast Cancer Response to Neoadjuvant Therapy Using H-Scan Ultrasound Imaging: Preliminary Preclinical Results," *J. Ultrasound Med. Off. J. Am. Inst. Ultrasound Med.*, vol. 38, no. 5, pp. 1259–1268, May 2019.
- [11] I. Z. Nenadic *et al.*, "Attenuation measuring ultrasound shearwave elastography and in vivo application in post-transplant liver patients," *Phys. Med. Biol.*, vol. 62, no. 2, pp. 484–500, 21 2017.
- [12] N. Tagawa, T. Hiraoka, and I. Akiyama, "Compensation of Frequency-Dependent Attenuation for Tissue Harmonic Pulse Compression Imaging," *Compend. New Tech. Harmon. Anal.*, Sep. 2018.
- [13] W. K. Cheung *et al.*, "Attenuation Correction and Normalisation for Quantification of Contrast Enhancement in Ultrasound Images of Carotid Arteries," *Ultrasound Med. Biol.*, vol. 41, no. 7, pp. 1876–1883, Jul. 2015.
- [14] E. L. Madsen, M. F. Insana, and J. A. Zagzebski, "Method of data reduction for accurate determination of acoustic backscatter coefficients," *J. Acoust. Soc. Am.*, vol. 76, no. 3, pp. 913–923, Sep. 1984.

- [15] F. T. D'Astous and F. S. Foster, "Frequency dependence of ultrasound attenuation and backscatter in breast tissue," *Ultrasound Med. Biol.*, vol. 12, no. 10, pp. 795–808, Oct. 1986.
- [16] K. Hoyt *et al.*, "Determination of Breast Cancer Response to Bevacizumab Therapy Using Contrast-Enhanced Ultrasound and Artificial Neural Networks," *J. Ultrasound Med.*, vol. 29, no. 4, pp. 577–585, 2010.
- [17] M. Khairalseed, K. Hoyt, J. Ormachea, A. Terrazas, and K. J. Parker, "H-scan sensitivity to scattering size," *J. Med. Imaging Bellingham Wash*, vol. 4, no. 4, p. 043501, Oct. 2017.
- [18] K. J. Parker, "Scattering and reflection identification in H-scan images," *Phys. Med. Biol.*, vol. 61, no. 12, p. L20, 2016.
- [19] S. A. Raki, S. Makino, H. Sawada, and R. Mukai, "Reducing musical noise by a fine-shift overlap-add method applied to source separation using a time-frequency mask," in *Acoustics, Speech, and Signal Processing, 2005. Proceedings.(ICASSP'05). IEEE International Conference on*, 2005, vol. 3, pp. iii–81.
- [20] C. E. Rasmussen, "Gaussian Processes in Machine Learning," in *Advanced Lectures on Machine Learning*, Springer, Berlin, Heidelberg, 2003, pp. 63–71.
- [21] E. Rosten and T. Drummond, "Machine Learning for High-Speed Corner Detection," in *Computer Vision – ECCV 2006*, 2006, pp. 430–443.
- [22] B. H. Juang and L. R. Rabiner, "The segmental K-means algorithm for estimating parameters of hidden Markov models," *IEEE Trans. Acoust. Speech Signal Process.*, vol. 38, no. 9, pp. 1639–1641, Sep. 1990.
- [23] K. Krishna and M. N. Murty, "Genetic K-means algorithm," *IEEE Trans. Syst. Man Cybern. Part B Cybern.*, vol. 29, no. 3, pp. 433–439, Jun. 1999.
- [24] K. Wagstaff, C. Cardie, S. Rogers, and S. Schroedl, "Constrained K-means Clustering with Background Knowledge," p. 8.
- [25] M. Hopf and T. Ertl, "Accelerating 3D convolution using graphics hardware," in *Proceedings Visualization '99 (Cat. No.99CB37067)*, Oct. 1999, pp. 471–564..
- [26] T. Tang, "The Hermite Spectral Method for Gaussian-Type Functions," *SIAM J. Sci. Comput.*, vol. 14, no. 3, pp. 594–606, May 1993.
- [27] F. Charpentier and M. Stella, "Diphone synthesis using an overlap-add technique for speech waveforms concatenation," in *Acoustics, Speech, and Signal Processing, IEEE International Conference on ICASSP'86.*, 1986, vol. 11, pp. 2015–2018.
- [28] R. Crochiere, "A weighted overlap-add method of short-time Fourier analysis/synthesis," *IEEE Trans. Acoust. Speech Signal Process.*, vol. 28, no. 1, pp. 99–102, 1980.

- [29] D. K. Nassiri, D. Nicholas, and C. R. Hill, "Attenuation of ultrasound in skeletal muscle," *Ultrasonics*, vol. 17, no. 5, pp. 230–232, Sep. 1979.
- [30] E. Kretzek, T. Hopp, and N. V. Ruiter, "GPU-based 3D SAFT reconstruction including attenuation correction," in *Medical Imaging 2015: Ultrasonic Imaging and Tomography*, Mar. 2015, vol. 9419, p. 94190E.
- [31] M. L. Oelze and W. D. O'Brien, "Method of improved scatterer size estimation and application to parametric imaging using ultrasound," *J. Acoust. Soc. Am.*, vol. 112, no. 6, pp. 3053–3063, Dec. 2002.
- [32] Thijssen JM. Ultrasonic tissue characterisation and echographic imaging. *Phys Med Biol* 1989; 34:1667-74.

CHAPTER 4

THREE-DIMENSIONAL H-SCAN ULTRASOUND IMAGING AND USE OF A CONVOLUTIONAL NEURAL NETWORK FOR SCATTERER SIZE ESTIMATION*

Authors – Haowei Tai ¹, Mawia Khairalseed ², Kenneth Hoyt ^{2*}

¹ Department of Electrical and Computer Engineering, EC 33

The University of Texas at Dallas

800 West Campbell Road

Richardson, Texas 75080-3021

² Department of Bioengineering, EC 39

The University of Texas at Dallas

800 West Campbell Road

Richardson, Texas 75080-3021

*Reproduced with permission from Tai, Haowei, Mawia Khairalseed, and Kenneth Hoyt. "3-D H-scan ultrasound imaging and use of a convolutional neural network for scatterer size estimation." *Ultrasound in medicine & biology* 46.10 (2020): 2810-2818.

Author contribution: Haowei Tai (myself) was responsible for the experimental design, data analysis, and the manuscript preparation presented here.

The purpose of this study was to introduce a three-dimensional (3D) H-scan US imaging approach for scatterer size estimation in volume space. Using a programmable research scanner (Vantage 256, Verasonics Inc, Kirkland, WA, USA) equipped with a custom volumetric imaging transducer (4DL7, Vermon, Tours, France), raw radiofrequency (RF) data was collected for offline processing to generate H-scan US volumes. A deep convolutional neural network (CNN) was modified and used to achieve voxel mapping from the input H-scan US image to underlying scatterer size. Preliminary studies were conducted using homogeneous gelatin-based tissue-mimicking phantom materials embedded with acoustic scatterers of varying size (15 to 250 μm) and concentrations (0.1 to 1%). Two additional phantoms were embedded with 63 or 125 μm -sized microspheres and used to test CNN estimation accuracy. *In vitro* results indicate that 3D H-scan US imaging can visualize the spatial distribution of acoustic scatterers of varying size at different concentrations ($R^2 > 0.85$, $p < 0.03$). The result of scatterer size estimation reveals that a CNN can achieve an average mapping accuracy of 93.3%. Overall, our preliminary *in vitro* findings reveal that 3D H-scan US imaging allows the visualization of tissue scatterer patterns and incorporation of a CNN can be used to help estimate size of the acoustic scattering objects.

4.1 Introduction

The use of noninvasive ultrasound (US) imaging for quantitative tissue characterization has been the focus of research efforts for several decades now [1]. The overarching challenge is to find hidden patterns in the US data to reveal more information about tissue function and pathology [1]–[3]. Several promising US-based tissue characterization methods have been introduced, namely, backscatter classification [4], integrated backscatter [5], spectral feature extraction [6], and tissue elasticity imaging [7], [8]. A potential limitation for some of these tissue characterization methods is that they use a relatively large kernel (window) of US data during quantification, which can impact spatial resolution and make *in vivo* measurement of local changes problematic. Since the visual criteria for scatterer size estimation is highly subjective, a deep convolutional neural network (CNN) can play an essential role in extracting image features and simplify the estimation task, especially *in vivo* where scatterer size may be unknown [9]–[11].

Recently, a new tissue characterization modality has emerged for the US classification of acoustic scatterers. Termed H-scan US (where the ‘H’ stands for Hermite or hue), this imaging approach links the mathematics of Gaussian-weighted Hermite (GH) functions to the physics of scattering and reflection from different tissue structures within a standard convolutional model of US pulse-echo systems [12]–[19]. Specific integer orders, termed GH_n , are related to the n^{th} derivative of a Gaussian function. Matched filters employing specific orders of GH_n functions are then used to analyze the spectral content of US backscattered echo signals and to colorize the display, providing visual discrimination between the major tissue scattering classes at high resolution [14]. In general, lower frequency spectral content is generated from larger scattering structures whereas higher frequency echo content is produced by the US wave interacting with

small scatterers of scale below the wavelength of the US transmit pulse (i.e. Rayleigh scatterers). Therefore, H-scan US is capable of estimating the relative size and spatial distribution of cellular structures and has shown promise in applications of monitoring cancer response to treatment [16].

To help improve the scatterer size estimation strategy, we developed a novel 3D H-scan US imaging system. The aim of this study was to validate this new US system using tissue-mimicking phantom materials. We investigated the feasibility of using 3D H-scan US volumes for tracking relative changes in scatterer size throughout the entire volume space. A convolutional neural network (CNN) architecture based on a modified Visual Geometry Group (VGG) regression model was introduced to map the H-scan US image to scatterer size and enable real-time tissue characterization. Overall, the hypothesis was that the proposed US imaging technology can increase the accuracy of scatterer size estimation, and data in volume space can highlight the heterogenous tissue microenvironment.

4.2 Materials and Methods

4.2.1 Phantom Material Fabrication

A series of homogeneous tissue-mimicking phantoms were prepared to contain a range of acoustic scatterers of varying size and concentration. Each phantom contained a base mixture of 75 g of gelatin (300 Bloom, Sigma Aldrich, St. Louis, MO, USA) and spherical US scatterers (US Silica, Pacific, MO, USA) in 1 L of H₂O. The diameter and concentration of the spherical scatterers were varied for each phantom produced, 15, 30, 40 or 250 μm and 0.1, 0.3, 0.5 or 1.0 %, respectively. Two separate phantoms containing spherical scatterers that were 63 or 125 μm in diameter (0.3 % concentration) were made to test the H-scan US imaging system estimation accuracy after training the CNN architecture. Phantom blocks were formed by heating the gelatin solution to at least 50

°C and then pouring into a rigid rectangular mold and allowing to cool overnight. The final material size was about $35 \times 35 \times 40$ mm (depth \times width \times elevation) and all 3D H-scan US imaging was performed at room temperature (25 °C).

4.2.2 US Data Acquisition

Volumetric H-scan US data was collected using a programmable research scanner (Vantage 256, Verasonics Inc, Kirkland, WA, USA) integrated with a custom imaging transducer (4DL7, Vermon, Tours, France). This 192-element (0.2 mm pitch) transducer has an 8.5 MHz center frequency and a motor-controlled mechanism to rapidly sweep the linear array for 3D data

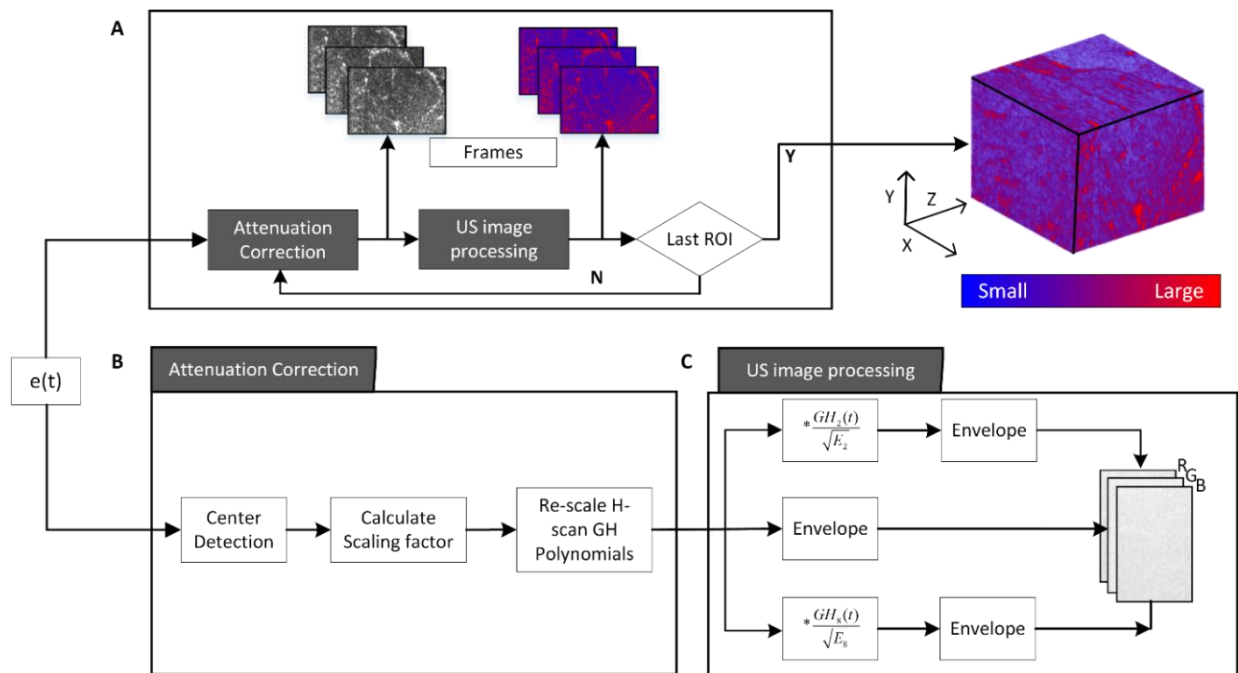


Figure 4.1. Flowchart of three-dimensional (3D) H-scan ultrasound (US) imaging. (A) By processing the 3D US image data, the H-scan US volume is reconstructed. (B) An adaptive k-means clustering algorithm is used to adjust the Gaussian-weighted Hermite (GH) kernels to account for frequency dependent attenuation. (C) The H-scan US processing via two different order GH polynomials used as parallel convolution filters. The low and high frequency information are then color-coded as red (R) and blue (B) to make the contrast among different sized scatterers more pronounced. The envelope of the received US echo is assigned to the green (G) channel to complete the RGB map.

acquisitions. The total scan angle was 27° (maximum negative and positive displacements of -13.5° and 13.5° , respectively) with the acceleration angle set to 0.135° to contain 200 frames per volume. All backscattered radiofrequency (RF) data was acquired using ultrafast plane wave imaging. Although the spatial resolution of US plane wave imaging is known to be inferior to focused US approaches, each frame using the former exposes the entire image field with nearly uniform acoustic intensity and avoids resolution differences at depth and away from any focusing used. Spatial angular compounding improves the spatial resolution of plane wave-based H-scan US imaging [15].

4.2.3 3D H-scan US Image Processing

After scan conversion, two parallel convolution filter kernels were applied to the acquired RF data sequences to measure the relative strength of the received signals relative to GH_n after normalization by the signal energy, Figure 4.1. To minimize correlation between the GH spectra and increase the image contrast, we used more disparate functions for the convolution filtering, namely GH_2 and GH_8 (Khairalseed et al. 2018, 2019a). The signal envelopes for each of the filtered data sequences were then calculated using a Hilbert transformation. Using an RGB colormap scheme, the relative strength of these filter outputs was color-coded whereby the lower frequency (GH_2) backscattered signals are assigned to the red (R) channel and the higher frequency (GH_8) components to the blue (B) channel. The envelope of the original unfiltered compounded B-scan US image is assigned to the green (G) channel to complete the colormap and 3D H-scan US image display.

4.2.4 Attenuation Correction

The Hermite functions have been well defined by Pierre-Simon Laplace [20] and the n^{th} order of its polynomial can be modeled as follows:

$$H_n(t) = (-1)^n e^{t^2} \frac{d^n}{dt^n} G(t) \quad (1)$$

$$n = 0, 1, 2, \dots; -\infty < t < \infty.$$

where $\frac{d^n}{dt^n} G(t)$ is the n^{th} order of derivative for a Gaussian pulse $G(t) = e^{-t^2}$. A pulse-echo US system (operating at 8 MHz center frequency) with a round trip impulse response has a high correlation with the 4th order of Gaussian weighted Hermite polynomial [19]. Therefore, $G(t)$ is used to weight the GH functions and then applied as bandpass filters to identify or associate the received US backscattered signal with the major signal types from tissue. According to H-scan US imaging theory [19], the US backscattered signal from larger and smaller acoustic scatterers can be modeled as follows:

$$e_L(t) = A(d) \frac{\Delta Z}{2Z} GH_2(t)(t - t_0) \quad (2)$$

$$e_S(t) = A(d) \frac{\Delta Z}{2Z} GH_8(t)(t - t_0) \quad (3)$$

where $A(d)$ is the US attenuation coefficient as a function of image depth d , $\frac{\Delta Z}{2Z}(t - t_0)$ is used to represent the acoustic impedance, and t_0 is a time delay. To isolate frequency information properly, GH functions in the frequency domain (spectrum centers) must be adjusted based on a particular RF signal spectrum. The Fourier transform (\mathcal{F}) of GH_n was defined as:

$$\mathcal{F} \left[GH_n \left(\frac{t}{\tau} \right) \right] = \frac{e^{-\frac{1}{4}\tau^2\omega^2} \tau^{n+1}\omega^n}{\sqrt{2}} \quad (4)$$

where $\tau \approx \frac{1}{f_0}$, and f_0 is the center frequency of transducer. The adjusting of GH_n in the frequency domain can be controlled via a scaling factor in the time domain as follows:

$$A(d)GH_n(t) = \mathcal{F}^{-1} \left[\frac{e^{-\frac{1}{4}\tau^2(\omega-\omega_\rho)^2} \tau^{n+1}(\omega-\omega_\rho)^n}{\sqrt{2}} \right] \quad (5)$$

where $A(d) = \mathcal{F}^{-1}(\|e^{-\frac{1}{4}\tau^2\omega_\rho^2} \omega_\rho\|)$ is the scaling factor of GH_n when the depth equals d . The frequency center is $\frac{1}{2} \int_0^\omega (\omega - \omega_\rho) d\omega$, which can be calculated by a depth-adaptive K-means clustering algorithm [21]–[23]. The center frequencies of the GH_n kernels were independently and continuously adjusted at all depths to maximize spectral coverage (see Figure 4.1), and the filtered signals were combined via an overlap-add method [24], [25].

4.2.5 Training and Testing Protocols

All H-scan and B-scan US datasets were in a standard 8-bit image format. The training was performed using a Windows 10 Pro operating system platform (Microsoft Corporation, Redmond, WA, USA) installed with MATLAB (Mathworks Inc, Natick, MA, USA) and the Neural Network and Parallel Processing Toolbox [26]. To adequately handle the processing, the computer had an NVIDIA TESLA K80 24GB graphics processor (Nvidia Corporation, Santa Clara, CA, USA) and 64 GB of RAM installed.

Training data for each category (i.e. scatterer size and concentration) was collected by imaging an assortment of tissue-mimicking phantom materials ($N = 14$, 200 images each). The

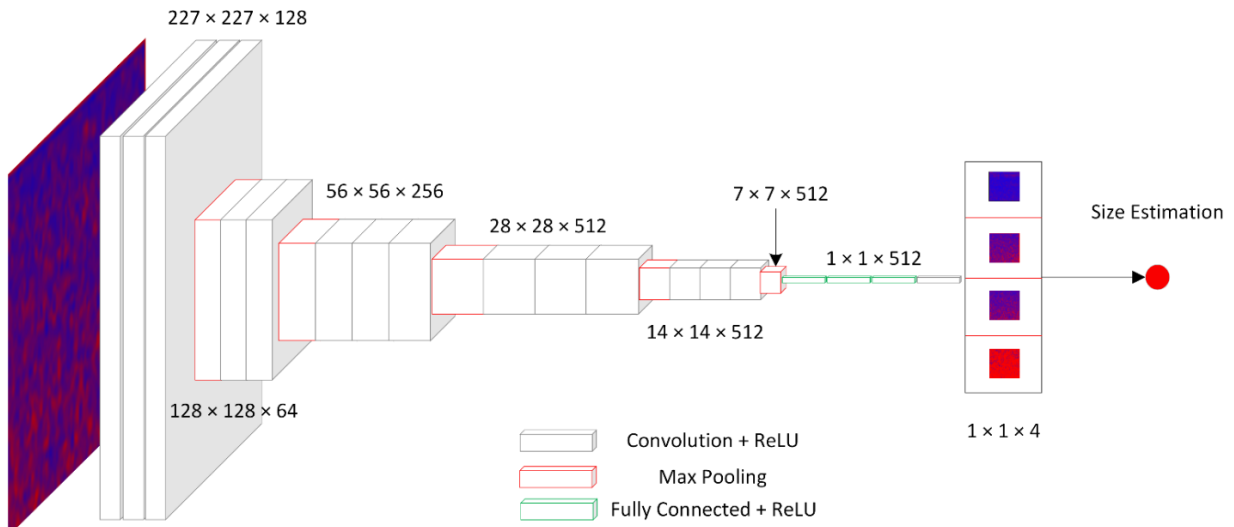


Figure 4.2. The architecture of the deep convolutional neural network (CNN) and modified Visual Geometry Group (VGG) kernels with down sampling and feature extraction. Architecture consists of 13 convolutional with rectified linear unit (ReLU) layers and 3 fully connected layers. The input data includes H-scan US images of phantom materials embedded with US scatterers of various sizes (15 to 250 μm) and concentrations (0.1 to 1.0 %). All image data was down sampled to small patches for CNN training.

sample size for each category was 2800. The US data collected from imaging the phantoms embedded with 15, 30, 40 or 250 μm -sized scatterers were randomly split into either training (70%) or validation (30%) sections. During the CNN training process, a modified VGG convolution operator was applied to extract image features [26], Figure 4.2. It contained 16 layers and the last layer was replaced with a regression layer to spatially map output images with estimates of scatterer size. For each patch, the training patches were resampled to a size of $227 \times 227 \times 3$ pixels. The initial learning rate was set to 0.001 to update weights every epoch. During final testing, 200 H-scan US images collected from phantom materials embedded with 63 or 125- μm scatterers were utilized. The average scatterer size (standard deviation, SD) was estimated by the trained CNN.

4.2.6 Statistical Analysis

For each experimental group, US volumes were summarized as the mean \pm SD from the weighted summation of the individual RGB channel components. The data variance between each measurement was used to assess heterogeneity in the spatial image intensity. To evaluate the impact of US scatterer size and concentration on 3D H-scan US imaging, a two-way analysis of variance (ANOVA) test was performed. A p -value less than 0.05 was considered statistically significant.

4.3 Results

A representative set of 3D H-scan US volume reconstructions is depicted in Figure 4.3. Collectively, the results reveal a progressive red color shift (with diminishing blue channel signal strength) as the size of the US scatterers was increased in the range from 15 to 250 μm . This agrees with the H-scan US theory whereby received backscattered US signals from larger scatterers dominate the red channel and that from smaller scattering objects dominates the blue channel. Recall that the red and blue channels are derived from the lower and higher frequency signals, respectively. The spatial distribution of the acoustic scatterers could be clearly detected throughout the entire 3D H-scan US volume space. Importantly, the H-scan volume color appears unchanged when the scatterer concentration in the phantom materials was varied. To study the impact of scatterer size and concentration on H-scan US image intensity, the mean value for each red and blue channel was summarized, Figure 4.4. Review of these measurements confirms the visual trends noted above. Since the H-scan US signal amplitude is a weighted sum of the RGB channel components, the image intensity variation (listed in Table 4.1) is more pronounced in volume reconstructions.

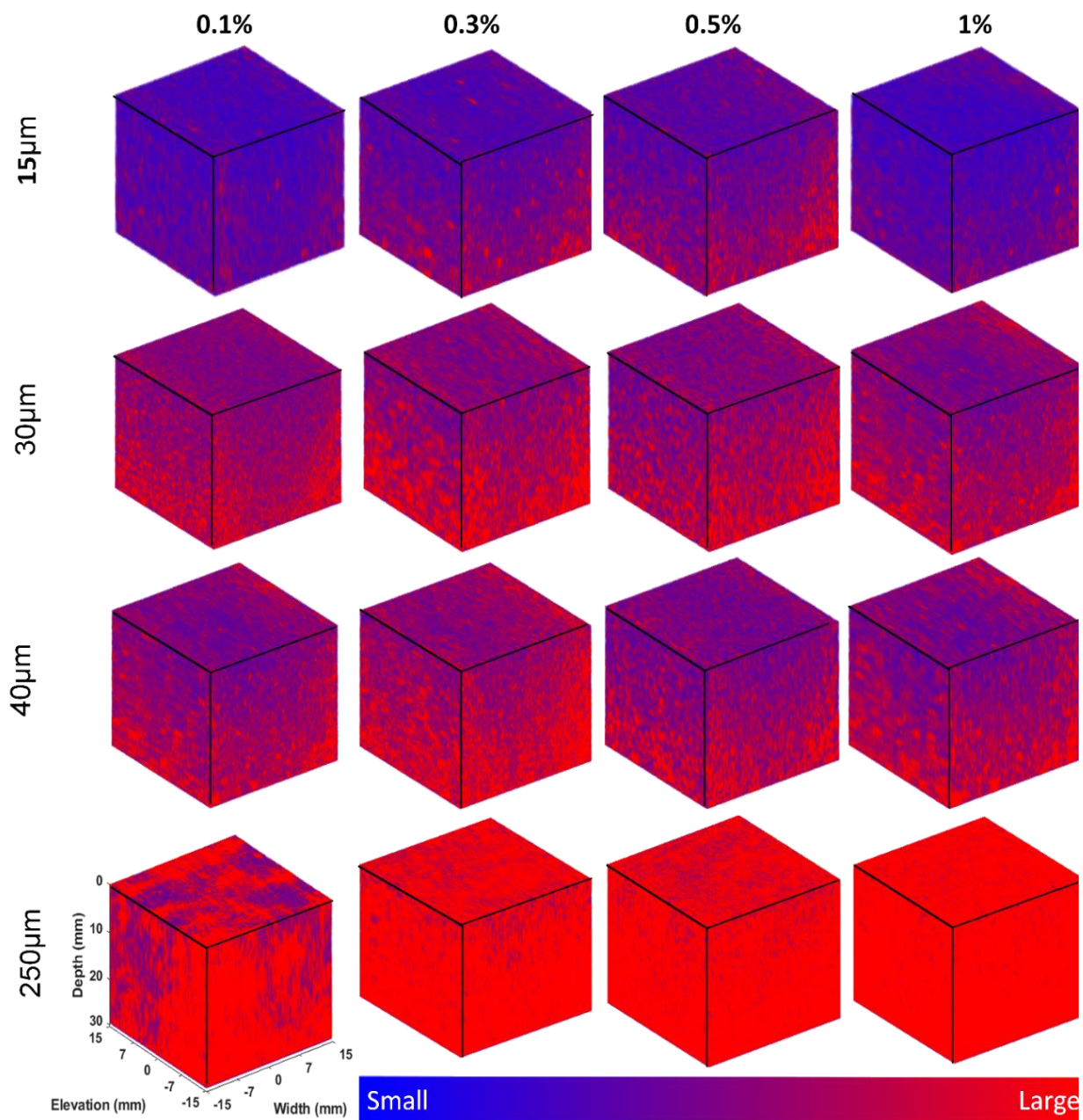


Figure 4.3. 3D H-scan images from phantoms embedded with 15, 30, 40 or 250 μm scatterers at concentrations of 0.1, 0.3, 0.5 or 1.0 %. The red channel (lower frequency US signal information) becomes dominant as scatterer size progressively increases while the blue channel (higher frequency information) diminishes.

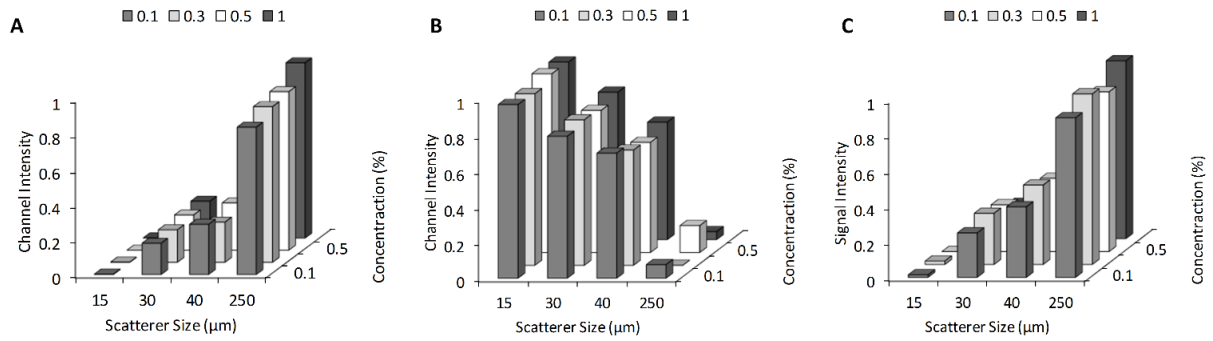


Figure 4.4. Spatial analysis of the (A) red and (B) blue channel signals used to generate the H-scan US images acquired from different phantom materials. Note the blue channel intensity decreases while red image intensity increases when the scatterer size increases. (C) Mean voxel values of the H-scan US images. Average image intensity increases with corresponding increased scatterer size.

Statistical analysis of the red channel data used to produce the final H-scan US image suggests that intensity is significantly affected by scatterer size ($p < 0.03$), but not concentration ($p = 0.24$). Scatterer size also had a significant impact on the blue channel data ($p < 0.03$), which was not the case for scatterer concentration ($p = 0.40$). Analysis of 3D H-scan US image intensities reveals the same data patterns and supports the use for scatterer size estimation ($p < 0.001$) and independent of scatterer density ($p = 0.62$). Overall, the ANOVA results of H-scan US images did not show a significant interaction between the effect of the concentration and the scatterer size ($p < 0.03$).

Table 4.1. Mean image intensity values calculated by averaging US data collected in phantom materials of varying concentrations.

Size (μm)	Mean (SD) US image intensity		
	Red	Blue	H-scan
15	0.001 (0.001)	0.98 (0.02)	0.01 (0.01)
30	0.19 (0.01)	0.81 (0.02)	0.25 (0.04)
40	0.27 (0.03)	0.66 (0.04)	0.42 (0.02)
250	0.91 (0.07)	0.07 (0.06)	0.94 (0.05)

To further illustrate scatterer size estimation using 3D H-scan US, different volume subregions from matched B-scan US were randomly selected for comparison. As Figure 4.5 reveals, the H-scan US images clearly highlights the capacity to characterize different sized acoustic scatterer populations, which is not possible using conventional B-scan US imaging alone. More specifically, after embedding spherical scatterers in the phantom materials of increasing size, the H-scan US images exhibited an overall intensity increase ($R^2 = 0.94$, $p = 0.02$). However, analysis of B-scan US image intensity values reveal this mode is less sensitive to changes in scatterer size ($R^2 = 0.89$, $p = 0.08$). Also illustrated in Figure 4.5, H-scan US image shows a more rapid change in image intensity with increases scatterer size (278.6%) as compared to B-scan (27.8%), which suggests H-scan US imaging is more sensitive to the scatterer size changes that were evaluated during the *in vitro* phantom studies ($p < 0.03$).

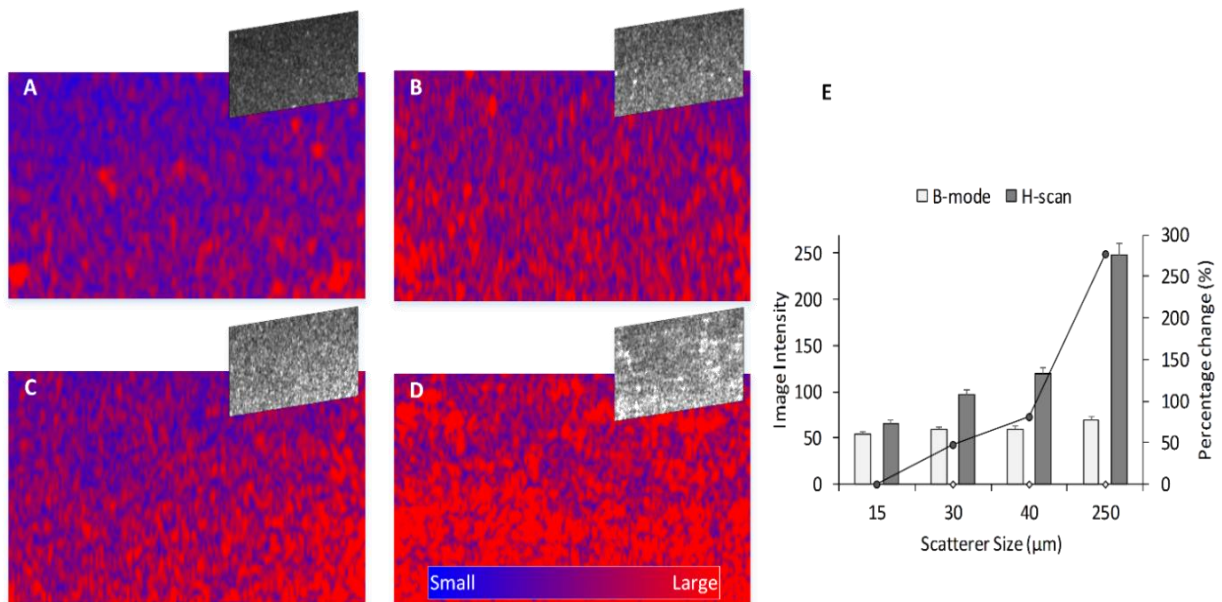


Figure 4.5. Representative H-scan US slices with coregistered B-scan US images for comparison. Phantoms were prepared using either (A) 15 μm, (B) 30 μm, (C) 40 μm, or (D) 250 μm acoustic scatterers. (E) Mean image intensity and the corresponding percentage changes reveals that 3D H-scan US is more sensitive to scatterer size changes than traditional B-mode US imaging.

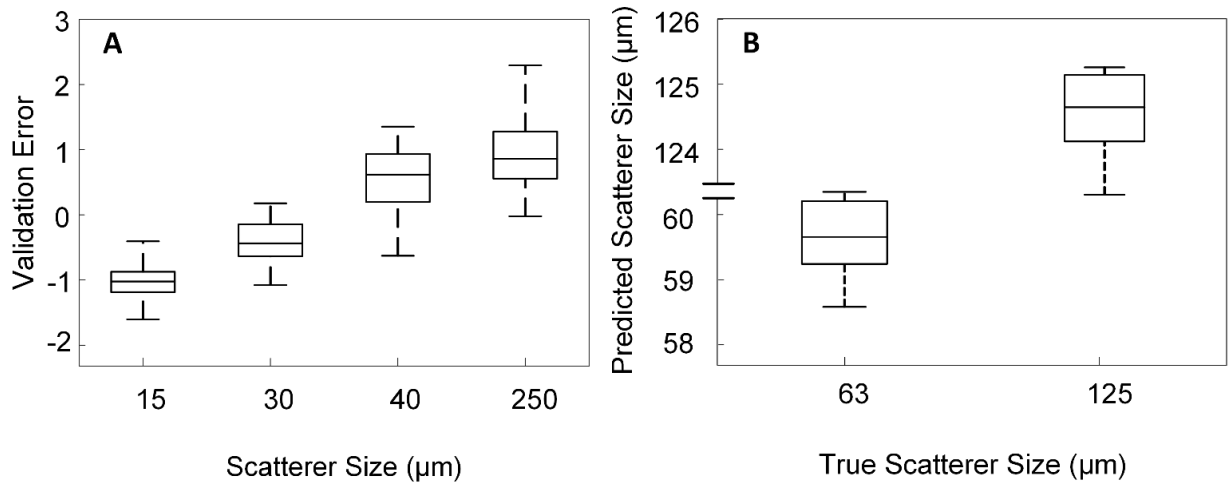


Figure 4.6. Box and whisker plots representing the root mean square error (RMSE) of the (A) four predicted and actual scatterer sizes during the training process and the (B) scatterer size estimates produced by the trained CNN. Note that the scatterers used for testing were not used during CNN training. The mean (standard deviation, SD) of the RMSE was reported to show the robustness of our model, namely, -0.98 (0.40), -0.40 (0.34), 0.59 (0.79) and 0.94 (0.60). H-scan US-based scatterer size estimates in (B) are 59.7 (0.6) μm and 124.6 (0.6) μm .

The H-scan US images obtained from homogenous phantoms were optimally modeled via machine learning methodologies. The 3D H-scan US images obtained from homogenous phantoms were used to train a CNN architecture based on a modified VGG regression model for accurate scatterer size estimation. The validation results reported in Figure 4.6 reveal that the CNN can yield a low average root-mean-square error (RMSE) of 0.95. Lastly, the trained CNN was used to estimate the scatterer size through H-scan US data collected by imaging phantoms that contained either 63 or 125- μm sized scatterers. Note that neither these phantom materials nor same-sized acoustic scatterer types were used in any of the CNN training sessions. Overall, the scatterer size predicted by the VGG model was 59.7 (\pm 0.6) μm when the input images were collected from homogeneous phantom materials embedded with the 63- μm sized scatterers. The estimated result was 124.6 (\pm 0.6) μm when the phantoms containing the 125- μm sized scatterers were studied.

4.4 Discussion

Analysis of the *in vitro* 3D H-scan US imaging data demonstrated the feasibility of qualitatively detecting changes in acoustic scatterer size in volume space. Furthermore, the trained CNN architecture helped reduce scatterer size estimation errors. Hence, the hypothesis of accurate scatterer size estimation using H-scan US and a CNN was supported by these findings. Compared to other scatterer size estimation algorithms, presented herein is the first study to demonstrate use of a 3D H-scan US technology to improve image contrast between different-sized US scatterers (in the range 15 to 250 μm) and independent of concentration (0.1 to 1.0 %).

Tracking scatterer changes can provide useful quantitative assessments for understanding the condition of healthy and diseased tissue. The scatterer size estimation methods proposed by Kurokawa et al. (2016) and Oelze and O'Brien (2002) use a moving region-of-interest (ROI) to calculate the correlation between a theoretical and acquired backscattered US signal. However, the design of the theoretical signal is complex and does not implicitly consider the mathematical relationship between the reflected US signal and underlying scatterer size. The calculation of signal correlation from the power spectrum can improve results but increases the computational cost. In contrast, it has been shown that the physics of reflection or scattering are linked to the mathematics of GH functions so the overall tissue characterization task can be simplified yet accurate [19]. Compared to the study conducted by [17], the 3D H-scan US imaging captures data from volume space and permits extended view of any tissue patterns or heterogeneities. Also, 3D imaging provides a more comprehensive view of the whole tissue structure and yield a more robust statistic if needed, which can further increase the accuracy of scatterer size estimation strategy. Our approach was shown to be robust when changing scatterer concentrations, whereas statistical

analysis of matched B-scan US data reveals image intensity may be different when scatterer density changes ($p < 0.05$). Thus, the use of B-scan US images alone for acoustic scatterer size tracking may be problematic and more work is needed.

The feature extraction model described by [28] appears to be less efficient than the method used and detailed herein, since the VGG model appears to help improve scatterer size estimation. Specifically, mapping accuracy using the Al-Kadi-based method was slightly lower when we used the same H-scan US images to train their model (86.3 versus 99.3 %). The estimation accuracy does increase by 15.1 % if H-scan US images are utilized as compared to the B-scan US images [29]. These improvements are attributed in part to increasing the dimension of the data for the input layer [30] and size of each kernel [31], [32]. Moreover, most of the previous studies in have been performed using two-dimensional (2D) B-scan US images [1]–[3], [5], [33]. The data collection throughout the entire volume (3D) space can highlight the heterogenous microenvironment and further help improve tissue characterization *in vivo* [34]. A custom 3D US transducer was used to generate high resolution H-scan US images and allows the user to pan through the entire tissue volume. This makes the monitoring of scatterer size on different subregions possible. Our image analysis revealed that when the phantom scatterer concentration was low (0.1 %), H-scan US image intensity was relatively lower than intensities calculated from phantom materials embedded with higher concentrations of same-sized acoustic scatterers, but still valid for our regression task. This confirms that the 3D H-scan US imaging is based on the clusters of scattering objects instead of an individual acoustic scatterer. The H-scan US technology could yield acceptable image quality from a medium containing a range of scatterer sizes and concentrations (i.e. heterogeneous tissue), but this needs to be verified with a detailed *in vivo*

imaging study including spatial correlation of matched physical measurements from tissue microscopy sections.

4.5 Conclusion

3D H-scan US is a novel bioimaging technology for estimating the size of acoustic scattering objects and structures. This approach outperformed B-scan US imaging when used for the same task. The H-scan US image intensity was considerably impacted by variations in scatterer size but not concentration. Use of a CNN architecture based on a modified VGG regression model allowed voxel-level mapping of H-scan US data to scatterer sizes (accuracy of 93.3 %). Overall, preliminary *in vitro* studies using 3D H-scan US imaging were encouraging and future work will explore use for *in vivo* tissue characterization.

4.6 Acknowledgements

This work was supported in part by NIH grant R01EB025841 and Texas CPRIT award RP180670.

4.7 References

- [1] T. Steifer and M. Lewandowski, "Ultrasound tissue characterization based on the Lempel–Ziv complexity with application to breast lesion classification," *Biomed. Signal Process. Control*, vol. 51, pp. 235–242, May 2019.
- [2] T. Opacic *et al.*, "Motion model ultrasound localization microscopy for preclinical and clinical multiparametric tumor characterization," *Nat. Commun.*, vol. 9, no. 1, p. 1527, Apr. 2018.
- [3] J. P. Kelly, S. L. Koppenhaver, L. A. Michener, L. Proulx, F. Bisagni, and J. A. Cleland, "Characterization of tissue stiffness of the infraspinatus, erector spinae, and gastrocnemius muscle using ultrasound shear wave elastography and superficial mechanical deformation," *J. Electromyogr. Kinesiol.*, vol. 38, pp. 73–80, Feb. 2018.
- [4] Y. Kurokawa, H. Taki, S. Yashiro, K. Nagasawa, Y. Ishigaki, and H. Kanai, "Estimation of size of red blood cell aggregates using backscattering property of high-frequency ultrasound: In vivo evaluation," *Jpn. J. Appl. Phys.*, vol. 55, no. 7S1, p. 07KF12, Jul. 2016.

- [5] H. Takami *et al.*, “Comparison between minimum lumen cross-sectional area and intraluminal ultrasonic intensity analysis using integrated backscatter intravascular ultrasound for prediction of functionally significant coronary artery stenosis,” *Heart Vessels*, vol. 34, no. 2, pp. 208–217, Feb. 2019.
- [6] L. Fang, N. He, S. Li, A. J. Plaza, and J. Plaza, “A New Spatial–Spectral Feature Extraction Method for Hyperspectral Images Using Local Covariance Matrix Representation,” *IEEE Trans. Geosci. Remote Sens.*, vol. 56, no. 6, pp. 3534–3546, Jun. 2018.
- [7] K. Hoyt, B. Castaneda, and K. J. Parker, “Two-dimensional sonoelastographic shear velocity imaging,” *Ultrasound Med. Biol.*, vol. 34, no. 2, pp. 276–288, 2008.
- [8] K. Hoyt *et al.*, “Tissue elasticity properties as biomarkers for prostate cancer,” *Cancer Biomark.*, vol. 4, no. 4–5, pp. 213–225, 2008.
- [9] L. Zhang *et al.*, “Automatic Assessment of Full Left Ventricular Coverage in Cardiac Cine Magnetic Resonance Imaging with Fisher Discriminative 3D CNN,” *IEEE Trans. Biomed. Eng.*, pp. 1–1, 2018.
- [10] Q. Zheng, M. Yang, J. Yang, Q. Zhang, and X. Zhang, “Improvement of Generalization Ability of Deep CNN via Implicit Regularization in Two-Stage Training Process,” *IEEE Access*, vol. 6, pp. 15844–15869, 2018.
- [11] S. Bhonsle, M. F. Lorenzo, A. Safaai-Jazi, and R. V. Davalos, “Characterization of Nonlinearity and Dispersion in Tissue Impedance During High-Frequency Electroporation,” *IEEE Trans. Biomed. Eng.*, vol. 65, no. 10, pp. 2190–2201, Oct. 2018.
- [12] G. R. Ge *et al.*, “H-scan analysis of thyroid lesions,” *J. Med. Imaging*, vol. 5, no. 1, p. 013505, Feb. 2018.
- [13] M. Khairalseed, K. Hoyt, J. Ormachea, A. Terrazas, and K. J. Parker, “H-scan sensitivity to scattering size,” *J. Med. Imaging*, vol. 4, no. 4, p. 043501, 2017.
- [14] M. Khairalseed, F. Xiong, R. Mattrey, K. Parker, and K. Hoyt, “Detection of early tumor response to abraxane using H-scan imaging: Preliminary results in a small animal model of breast cancer,” in *2017 IEEE International Ultrasonics Symposium (IUS)*, Sep. 2017, pp. 1–4.
- [15] M. Khairalseed, F. Xiong, J.-W. Kim, R. F. Mattrey, K. J. Parker, and K. Hoyt, “Spatial Angular Compounding Technique for H-Scan Ultrasound Imaging,” *Ultrasound Med. Biol.*, vol. 44, no. 1, pp. 267–277, Jan. 2018.
- [16] M. Khairalseed, K. Javed, G. Jashkaran, J.-W. Kim, K. J. Parker, and K. Hoyt, “Monitoring early breast cancer response to neoadjuvant therapy using H-scan ultrasound imaging: Preliminary preclinical results,” *J Ultrasound Med*, vol. 38, no. 5, pp. 1259–1268, 2019.

- [17] M. Khairalseed, K. Brown, K. J. Parker, and K. Hoyt, “Real-time H-scan ultrasound imaging using a Verasonics research scanner,” *Ultrasonics*, vol. 94, pp. 28–36, Apr. 2019.
- [18] K. J. Parker, “Scattering and reflection identification in H-scan images,” *Phys. Med. Biol.*, vol. 61, no. 12, pp. L20–28, 2016.
- [19] K. J. Parker, “The H-scan format for classification of ultrasound scattering,” *OMICS J. Radiol.*, vol. 5, no. 5, pp. 1–7, 2016.
- [20] T. Tang, “The Hermite Spectral Method for Gaussian-Type Functions,” *SIAM J. Sci. Comput.*, vol. 14, no. 3, pp. 594–606, May 1993.
- [21] Z. Huang, “Extensions to the k-Means Algorithm for Clustering Large Data Sets with Categorical Values,” *Data Min. Knowl. Discov.*, vol. 2, no. 3, pp. 283–304, Sep. 1998.
- [22] B. H. Juang and L. R. Rabiner, “The segmental K-means algorithm for estimating parameters of hidden Markov models,” *IEEE Trans. Acoust. Speech Signal Process.*, vol. 38, no. 9, pp. 1639–1641, Sep. 1990.
- [23] K. Krishna and M. N. Murty, “Genetic K-means algorithm,” *IEEE Trans. Syst. Man Cybern. Part B Cybern.*, vol. 29, no. 3, pp. 433–439, Jun. 1999.
- [24] R. Crochiere, “A weighted overlap-add method of short-time Fourier analysis/synthesis,” *IEEE Trans. Acoust. Speech Signal Process.*, vol. 28, no. 1, pp. 99–102, 1980.
- [25] M. J. Narasimha, “Modified Overlap-Add and Overlap-Save Convolution Algorithms for Real Signals,” *IEEE Signal Process. Lett.*, vol. 13, no. 11, pp. 669–671, Nov. 2006.
- [26] S. Ji, W. Xu, M. Yang, and K. Yu, “3D Convolutional Neural Networks for Human Action Recognition,” *IEEE Trans. Pattern Anal. Mach. Intell.*, vol. 35, no. 1, pp. 221–231, Jan. 2013.
- [27] M. L. Oelze and W. D. O’Brien, “Method of improved scatterer size estimation and application to parametric imaging using ultrasound,” *J. Acoust. Soc. Am.*, vol. 112, no. 6, pp. 3053–3063, Dec. 2002.
- [28] O. S. Al-Kadi, D. Y. F. Chung, C. C. Coussios, and J. A. Noble, “Heterogeneous Tissue Characterization Using Ultrasound: A Comparison of Fractal Analysis Backscatter Models on Liver Tumors,” *Ultrasound Med. Biol.*, vol. 42, no. 7, pp. 1612–1626, Jul. 2016.
- [29] M. Biswas *et al.*, “Symtosis: A liver ultrasound tissue characterization and risk stratification in optimized deep learning paradigm,” *Comput. Methods Programs Biomed.*, vol. 155, pp. 165–177, 2018.
- [30] L. Zhang, and I. Noguees, R. M. Summers, S. Liu, and J. Yao, “DeepPap: Deep Convolutional Networks for Cervical Cell Classification,” *IEEE J. Biomed. Health Inform.*, vol. 21, no. 6, pp. 1633–1643, Nov. 2017.

- [31] K. Lee, M. Lam, R. Pedarsani, D. Papailiopoulos, and K. Ramchandran, "Speeding Up Distributed Machine Learning Using Codes," *IEEE Trans. Inf. Theory*, vol. 64, no. 3, pp. 1514–1529, Mar. 2018.
- [32] Y.-D. Zhang, K. Muhammad, and C. Tang, "Twelve-layer deep convolutional neural network with stochastic pooling for tea category classification on GPU platform," *Multimed. Tools Appl.*, vol. 77, no. 17, pp. 22821–22839, Sep. 2018.
- [34] A. Sayed, G. Layne, J. Abraham, and O. Mukdadi, "Nonlinear characterization of breast cancer using multi-compression 3D ultrasound elastography in vivo," *Ultrasonics*, vol. 53, no. 5, pp. 979–991, Jul. 2013.

CHAPTER 5

THREE-DIMENSIONAL H-SCAN ULTRASOUND IMAGING OF EARLY BREAST CANCER RESPONSE TO NEOADJUVANT THERAPY IN A MURINE MODEL*

Authors – Haowei Tai ¹, Jane Song ², Junjie Li ², Shreya Reddy ², Mawia Khairalseed ²,
Kenneth Hoyt ^{2*}

¹ Department of Electrical and Computer Engineering, EC 33

The University of Texas at Dallas

800 West Campbell Road

Richardson, Texas 75080-3021

² Department of Bioengineering, EC 39

The University of Texas at Dallas

800 West Campbell Road

Richardson, Texas 75080-3021

*Part 1 of this chapter is reproduced with permission from Tai, Haowei, et al. "Three-dimensional H-scan ultrasound imaging of early breast cancer response to neoadjuvant therapy in a murine model." *Investigative Radiology* 57.4 (2022): 222-232. Part 2 will be submitted for future publication.

Author contribution: Haowei Tai (myself) was responsible for the experimental design, data analysis, and the manuscript preparation presented here.

The goal of this research was to evaluate use of 3-D H-scan ultrasound imaging for monitoring early breast cancer response to neoadjuvant therapy using a preclinical murine model of breast cancer. Preclinical studies were conducted using luciferase-positive breast cancer-bearing mice ($N = 40$). Anesthetized animals underwent ultrasound imaging at baseline before administration with an apoptosis-inducing drug or a saline control. Image data was acquired using an ultrasound scanner equipped with a volumetric transducer following either a shorter or longer term protocol. The later included bioluminescent imaging to quantify tumor cell viability. At termination, tumors were excised for *ex vivo* analysis. *In vivo* results showed that 3-D H-scan ultrasound imaging is considerably more sensitive to tumor changes after apoptosis-inducing drug therapy as compared to traditional B-scan ultrasound. While there was no difference at baseline ($p > 0.99$), H-scan ultrasound results from treated tumors exhibited progressive decreases in image intensity (up to 62.2% by day 3) that had a significant linear correlation with cancer cell nuclear size ($R^2 > 0.51$, $p < 0.001$). Results were validated by histological data and a secondary longitudinal study with survival as the primary endpoint. Experimental results demonstrate that noninvasive 3-D H-scan ultrasound imaging can detect an early breast tumor response to apoptosis-inducing drug therapy. Local *in vivo* H-scan ultrasound image intensity correlated with cancer cell nuclear size, which is one of the first observable changes of a cancer cell undergoing apoptosis and confirmed using histological techniques. Early imaging results appear to provide prognostic insight on longer-term

tumor response. Overall, 3-D H-scan ultrasound imaging is a promising technique that visualizes the entire tumor and detects breast cancer response at an early stage of therapy.

5.1 Part 1

5.1.1 Introduction

The goal of personalized medicine is becoming increasingly important to maximize effective therapy for an individual patient, reduce morbidity, and constrain escalating health care costs associated with overtreatment. Breast cancer is the most common type of cancer in women (30% of new cases) with the second highest mortality rate (15% of cancer deaths each year) [1]. Monitoring response to treatment is a key element in the management of breast cancer. In the neoadjuvant setting, assessing tumor response to treatment prior to surgery to include evaluation for pathologic response can provide prognostic information to help guide follow up care.[2] The more successful breast cancer treatments are targeted to cancer cell receptors known to promote tumor growth, namely, estrogen receptors (ER), progesterone receptors (PR), and human epidermal growth factor receptor 2 (HER2). However, triple negative breast cancer (TNBC) is a particularly aggressive form of breast cancer that is not treated with drugs that target the aforementioned receptors.[3]–[5] Approximately 15 to 20% of all breast tumors are classified as TNBC[6] and this disease disproportionately affects young women of African origin.[7] Due to high metastatic potential and poor patient prognosis, improved therapy is needed for women diagnosed with TNBC. In the interim, inexpensive and noninvasive methods to determine early treatment response are urgently needed to determine if the chosen anticancer therapy is efficacious and discontinue treatment of the patient with a costly high-risk regimen with no demonstrable benefit.

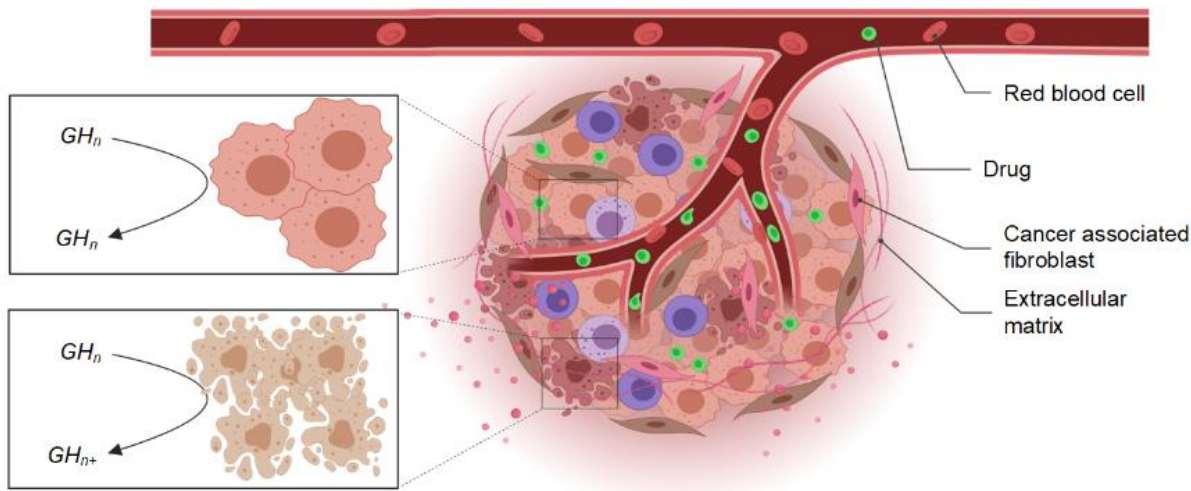


Figure 5.1. Apoptosis is a form of programmed cell death that leads to the physical change of cancer cells including considerable nuclear shrinkage (condensation) at the early stage after treatment with apoptosis-inducing chemotherapeutic drugs.

By a biological process known as apoptosis, the aim of cancer treatment is to induce tumor cell death. This process involves a carefully orchestrated sequence of intracellular events that systematically dismantle the cell. Previous studies have demonstrated that a wide range of anticancer drugs, including many chemotherapeutic agents, induce apoptosis in malignant cells *in vitro*. [8] Characteristic apoptotic changes have also been described in solid tumors after treatment. [9] As illustrated in Figure 5.1, the first observable morphological change in a cancer cell undergoing apoptosis is considerable shrinkage of both the cell and nucleus (up to 50% volume change). [10], [11] Both acquired and intrinsic drug resistance often prevents cancer cells from undergoing sufficient levels of apoptosis, resulting in cancer cell survival and treatment failure. [12] This chemotherapy-induced autophagy is a protective response that actually leads to cancer cell swelling. [13] Noninvasive imaging tools that are sensitive to changes in cancer cell size after neoadjuvant therapy represent a new prognostic biomarker for evaluating early treatment response.

A major clinical challenge in monitoring neoadjuvant therapy is how to detect and accurately quantify response at an early stage. Current methods for evaluating breast tumor response to neoadjuvant therapy consist of physical examination and conventional breast imaging with mammography and ultrasound. These assessment methods involve tracking changes in tumor size relative to baseline measures, using guidelines provided by the Response Evaluation Criteria in Solid Tumors (RECIST) [14]. However quantifiable changes in bulk tumor size may not be detectable until after multiple cycles of chemotherapy, i.e. months.[15] Specialized magnetic resonance imaging (MRI) techniques like diffusion-weighted MRI (DW-MRI) and dynamic contrast-enhanced MRI (DCE-MRI), have also been explored for use in monitoring early therapeutic response in breast cancer patients [16]. However, MRI requires a considerable capital investment, and lengthy exam times can produce patient discomfort and claustrophobia. There is also an ongoing concern that preoperative MRI shows clinically irrelevant tumors and increases mastectomies without patient benefit [17], [18]. In recent years, clinical use of contrast-enhanced spectral mammography (CESM) has shown promise for neoadjuvant therapy monitoring [19]. Notwithstanding, studies in large patient populations are still needed to validate initial findings [20]. While ultrasound is a convenient and affordable modality, newer advances are necessary to improve breast tumor imaging.

Noninvasive ultrasound imaging has slowly evolved from a modality for only a subset of practitioners to a tool with applications in nearly all medical fields. In addition to being relatively inexpensive, ultrasound has other unique features that make it attractive for medical professionals like use of nonionizing radiation, portability, and real-time imaging capability [21]. Given the ubiquitous use of ultrasound imaging, researchers were motivated to search for hidden patterns in

the ultrasound data that might help reveal more information about tissue health and function.[22] Termed tissue characterization, several promising quantitative ultrasound methods have been explored.[23]–[25] Independent of instrumentation and the operator when properly implemented, these techniques examine the frequency content of backscatter ultrasound signals to extract quantitative parameters that are directly linked to the tissue microstructure. Accuracy of these quantitative ultrasound methods is dependent on reference signal measurements from a calibration phantom and hydrophone. Despite preclinical successes, translation to human studies and clinical adoption has encountered barriers. In part, quantitative ultrasound techniques are too computationally intensive for existing hardware, or not robust enough for everyday clinical use.[26] Notwithstanding, these issues are being diminished with modern technology and quantitative ultrasound imaging for tissue characterization may be on the verge of wide clinical applicability and use as an adjunct to diagnostic procedure.

Bypassing some of the computational complexity issues associated with the more established tissue characterization approaches, a new ultrasound modality has recently emerged to qualitatively investigate the backscattering properties of tissue. Called H-scan ultrasound (where ‘H’ denotes Hermite), this imaging approach is based on the classification theory for tissue scattering.[27] Using a matched filter methodology applied to backscattered ultrasound signals, filter outputs are used to colorize a display to provide local discrimination between various-sized ultrasound scatterers in real-time.[28], [29] In general, lower frequency spectral content is generated from larger scattering structures whereas the higher frequency signal content is produced by an ultrasound wave interacting with smaller scatterers of scale below the wavelength of the ultrasound transmit pulse (i.e., Rayleigh scatterers). Using a murine model of TNBC, it was shown

that this ultrasound imaging modality can detect an early response to neoadjuvant therapy.[30], [31]. Early intratumoral changes in the *in vivo* H-scan ultrasound signal amplitude were shown to be positively correlated with histologic measurements of apoptotic activity. Independently, a strong correlation was also found between the local H-scan ultrasound image intensity and physical measures of cancer cell nuclear size from co-registered histologic tissue sections.[32], [33] Collectively, these findings demonstrate how H-scan ultrasound images depict scatterer size and spatial distribution of the rigid cell nucleus while offering prognostic insight on chemotherapy-induced cancer cell death.

A potential limitation of current *in vivo* H-scan ultrasound approaches is that they are restricted to planar imaging and may not accurately capture spatially-varying tissue patterns. In response, recent research efforts have introduced a volumetric H-scan ultrasound imaging system and method that estimates the relative size of scattering objects and structures. Preliminary *in vitro* studies in phantom materials embedded with microspheres revealed 3-dimensional (3-D) H-scan ultrasound imaging can visualize the spatial distribution of acoustic scatterers of varying size at different concentrations.[34] When coupled with a deep learning approach, quantitative estimates of actual scatterer size achieved an average mapping accuracy exceeding 93%.

Breast cancer is now widely known to be a heterogeneous disease that differs greatly between different patients and within each individual tumor type.[35], [36] This spatial heterogeneity inevitably impacts tumorigenicity, metastatic potential, and therapy response or resistance. Therefore, the purpose of this study was to detail the initial use of *in vivo* 3-D H-scan ultrasound imaging for the assessment of early TNBC response to neoadjuvant therapy. Using a murine model of breast cancer and two different experimental protocols, longitudinal H-scan

ultrasound imaging was applied at baseline and again at different time points after administration of neoadjuvant therapy. Image findings were compared to histologic measures of treatment efficacy.

5.1.2 Materials and Methods

5.1.2.1 Animal Model and Treatment Protocol

All procedures were carried out in accordance with relevant guidelines and regulations. Animal experiments were performed based on a protocol approved by the Institutional Animal Care and Use Committee (IACUC) at the University of Texas at Dallas. Preclinical studies were conducted using female nude athymic mice ($N = 40$, Charles River Laboratories, Wilmington, MA) implanted with 1 million luciferase-positive breast cancer cells (MDA-MB-231, American Type Culture Collection, Manassas, VA) in the mammary fat pad. Once tumors reached approximately 6 to 8 mm in size (maximum diameter) as measured using calipers, mice were randomized into the control or treatment groups. After baseline (day 0) imaging, mice received intraperitoneal injections of (i) 0.3 ml sterile saline (control), (ii) 8 mg/kg of agnostic TRA-8 monoclonal antibody

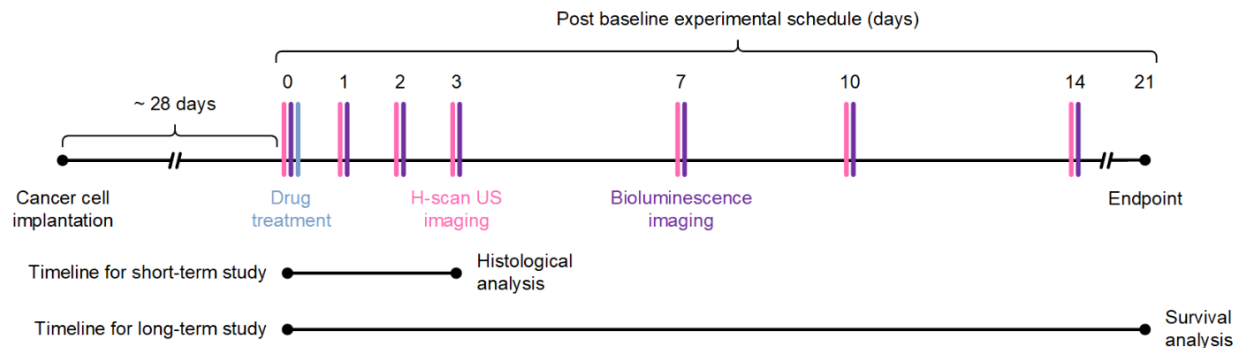


Figure 5.2. Timeline of the *in vivo* imaging and drug treatment schedule timeline for both a shorter-term and longer-term study. At study conclusion or when tumor burden guidelines warranted, mice were sacrificed and tumors excised for *ex vivo* analysis.

to human death receptor 5 (DR5) + 0.1 ml sterile saline, (iii) 4 mg/kg paclitaxel + 0.2 ml sterile saline, or (iv) 8 mg/kg TRA-8 + 4 mg/kg paclitaxel ($N = 5$ per group). The post baseline experimental schedule and timeline for both a shorter-term (days 0 to 3) and longer-term (day 0 to 21) study is presented in Figure 5.2, whereby the primary endpoints were histological and survival analysis, respectively. At study conclusion or when tumor burden guidelines warranted, mice were humanely euthanized via cervical dislocation and tumors excised for *ex vivo* analysis. During all *in vivo* imaging procedures, animals were controlled with isoflurane anesthesia (V3000PK, Parkland Scientific, Coral Springs, FL).

5.1.2.2 H-scan Ultrasound Imaging

3-D H-scan ultrasound data was collected using a programmable research scanner (Vantage 256, Verasonics Inc, Kirkland, WA) equipped with a custom transducer (4DL7, Vermon, Tours, France). This 192-element (0.2 mm pitch) transducer has an 8.5 MHz center frequency and a motor-controlled mechanism to rapidly sweep the linear array for volumetric data acquisitions. The total scan angle was 27° (maximum negative and positive displacements of -13.5° and 13.5° , respectively) with an acceleration angle set to 0.135° to allow collection of 200 frames per volume at a rate of about 2 Hz. Under B-scan ultrasound guidance, radiofrequency (RF) data was acquired using a plane wave imaging and saved for offline processing.

All ultrasound data underwent scan conversion and attenuation correction to recover any depth-dependent signal loss [37]. The RF data was then processed to classify the scattering transfer functions of tissue. Knowing the two-way impulse response of our ultrasound system has a high correlation to a 4th-order Gaussian-weighted Hermite polynomial (GH_4), parallel convolutional filters comprised of 2nd and 8th-order Gaussian-weighted Hermite polynomials (GH_2 and GH_8)

were used to capture the low and high frequency information, respectively. After normalization by the signal energy and envelop detection, lower and higher frequency filter outputs were assigned to a pseudo-color map and used for the H-scan ultrasound volume reconstruction and visualization of larger and smaller scatterers, respectively.[38], [39] A review of the H-scan ultrasound image formation process is presented in Figure 5.3.

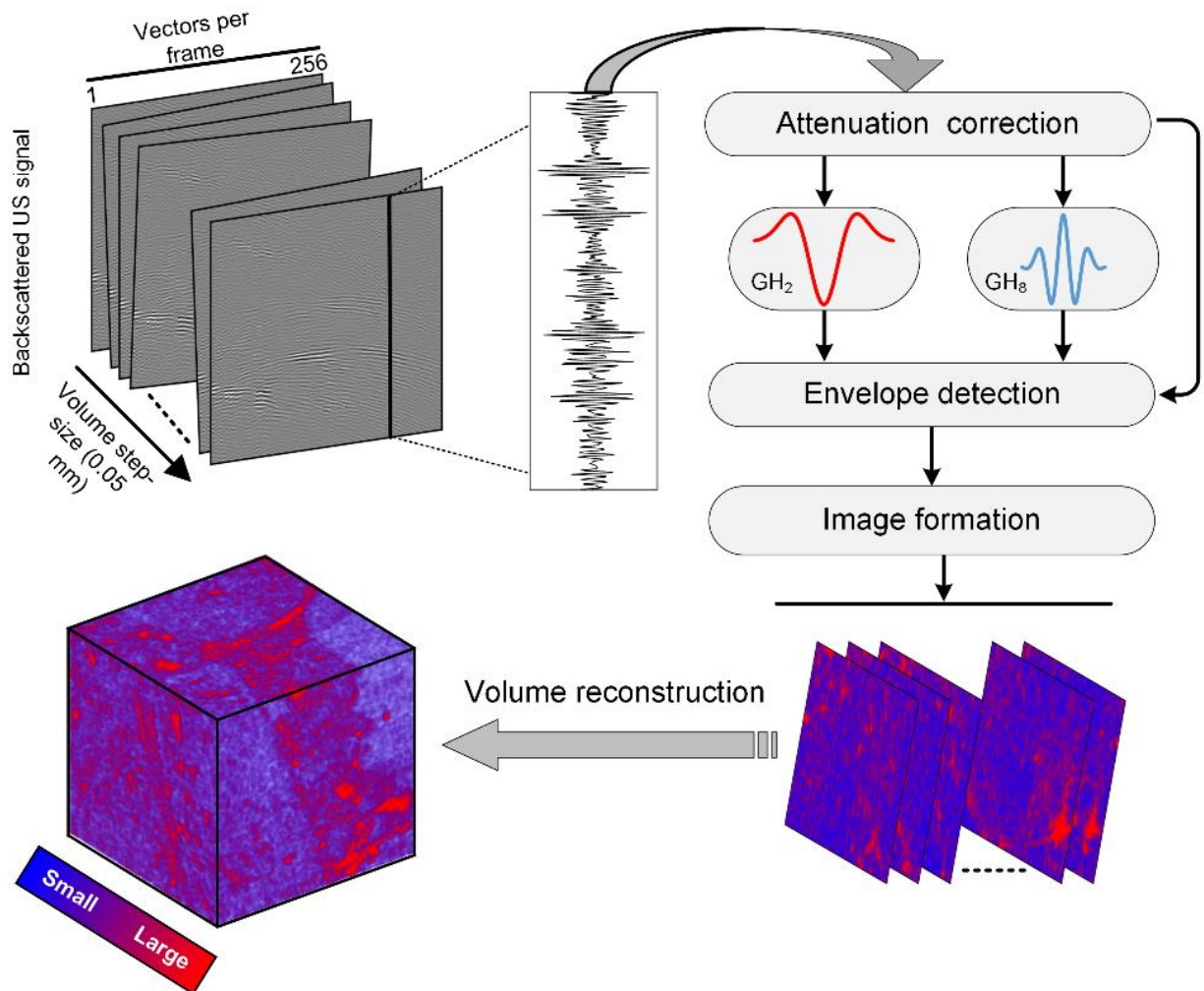


Figure 5.3. Schematic diagram of the 3-D H-scan ultrasound image formation process. Using a pair of n^{th} -order Gaussian-weighted Hermite polynomials (denoted GH_2 and GH_8 , respectively), parallel convolution filters were applied before normalization by the signal energy (E_n). After envelope detection, low and high frequency information is then color-coded as red and blue to describe larger and smaller ultrasound scatterers, respectively.

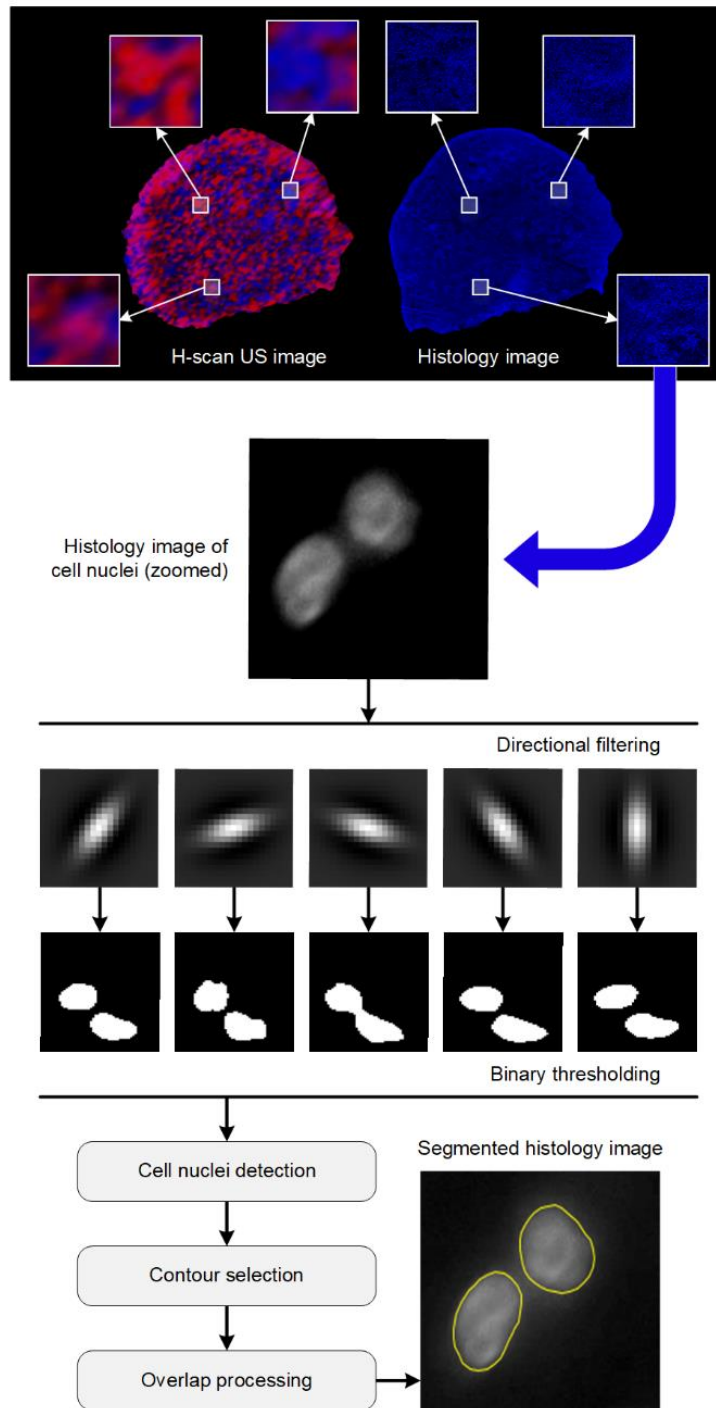


Figure 5.4. Summary of the segmentation approach for measurement of nuclear size and location from the DAPI-stained histologic images. After nuclei localization using a directional filter bank, an initial global segmentation is performed. Nuclei edges were then processed to find the best contour with minimum calculated loss before calculating mean nuclear size from small subregions.

5.1.2.3 Optical Imaging

Optical imaging allows longitudinal measurement of bioluminescent signals from luciferase-positive cancer cells and commonly used for indication cell viability in living organisms. Mice were administered D-luciferin ($300 \text{ mg}\cdot\text{kg}^{-1}$ body weight in saline; Gold Biotechnology Inc, St. Louis, MO) via intraperitoneal injection. Following a 10 min incubation period, mice were anesthetized and bioluminescence imaging was performed using a small animal optical system (Pearl Trilogy, LI-COR Bioscience, Lincoln, NE). Images were acquired at baseline and again at each time corresponding to the ultrasound imaging sessions. Bioluminescent signal intensity was measured for each tumor using system software (Image Studio Software, LI-COR Biosciences). All measurements were normalized by the background bioluminescent signal and then pixel count of the tumor region.

5.1.2.4 Histology

Animals were humanely euthanized via cervical dislocation under deep anesthesia and tumors were excised for *ex vivo* analysis. Tumors were fixed in 10% neutral-buffered formalin for at least 7 d at room temperature. Tissue samples were embedded in paraffin, sectioned ($5 \mu\text{m}$), and mounted taking care to select similarly sized sections representative of both the tissue edge and center. Deparaffinization was performed using xylene for 10 min followed by washing through a descending alcohol series and tap water. Multiple sections were obtained throughout the entire tumor volume and stained for activated caspase-3 (AC3, cell apoptosis) and Ki-67 (cell proliferation) using established protocols. Tumor sections were also fluorescently stained with 4',6-diamidino-2-phenylindole (DAPI) to identify cancer cell nuclei. Whole tissue cross-sections were optically scanned and digitized at 40x magnification (Axio Observer 7, Carl Zeiss

Microscopy, White Plains, NY). Both AC3 and Ki67 activity was analyzed and tissue stain was recorded as a fraction of the entire tissue cross-section.

5.1.2.5 Histological Image Analysis

All image processing was performed using custom MATLAB software MathWorks Inc, Natick, MA). Feature matching based image automatic registration was performed to find the H-scan ultrasound image from the volume stack that best matched the DAPI-stained histologic tissue cross-section.[40] Generalized Laplacian of Gaussian (gLoG) kernels with five different orientations were used to localize the nucleus of each cancer cell and then a multi-scale radial line scanning (mRLS) method performed contour delineation.[41] The mRLS-based technique first identifies several candidate boundary contours for each cell nucleus. The gradient, intensity, and shape information are then integrated to determine the optimal boundary from candidate boundary contours. The Dice coefficient measure is finally applied to resolve any severely overlapped cancer cell nuclei. A summary of the histologic image analysis is presented in Figure 5.4. Next, the co-registered H-scan ultrasound and histologic image with nuclei localizations were equally divided into 100 distinct region-of-interests (ROIs). For each, the mean H-scan ultrasound image intensity and nuclear size was computed. Each detected nucleus was segmented to compute nuclear size and the average was calculated within the ROI to compare with corresponding matched H-scan ultrasound image features.

5.1.2.6 Statistical Analysis

In vivo group data was summarized as mean \pm SD. A two-way analysis with repeat measures was used to assess changes in the longitudinal data. A mixed-effects model analysis was performed to

make comparisons between ultrasound imaging-based group measurements. A Welch's *t*-test was used to compare group means from the histologic data. A simple linear regression analysis was applied to local H-scan ultrasound image intensity and nuclear size. A *P*-value less than 0.05 will be considered statistically significant. All analyses were performed using Prism software (GraphPad Software, San Diego, CA).

5.1.3 Results

3-D H-scan ultrasound imaging was used to assess early TNBC response to neoadjuvant therapy following initiation of neoadjuvant therapy in a murine model. This drug treatment included a single dose of control, agnostic TRA-8 monoclonal antibody to human death receptor 5 (DR5), paclitaxel, or combination TRA-8 + paclitaxel. A representative group of 3-D H-scan ultrasound image reconstructions and plots of group summary statistics are depicted in Figure 5.5. Inspection of the segmented H-scan ultrasound volumes reveals subtle spatial heterogeneity around the tumor periphery. While no differences in image intensity were found at baseline ($p > 0.99$), longitudinal H-scan ultrasound volumes reveal a progressive blue color (hue) shift for tumors undergoing chemotherapy, while the control group appears unchanged over the same short time interval.

A repeat measures analysis found a statistically significant change in H-scan ultrasound image intensity from the TRA-8 + paclitaxel treated mice ($p = 0.04$) but not from the other treatment groups ($p > 0.21$). Notwithstanding, compared to baseline measurements, there were pronounced $-19.8 \pm 8.2\%$, $-51.4 \pm 0.1\%$, and $-62.2 \pm 7.8\%$ decreases in the mean H-scan ultrasound image intensity at day 3 for the TRA-8, paclitaxel, and TRA-8 + paclitaxel treated tumor groups, respectively. A similar analysis of repeat 3-D B-scan ultrasound images found no significant differences for any of the treatment group measurements ($p > 0.58$).

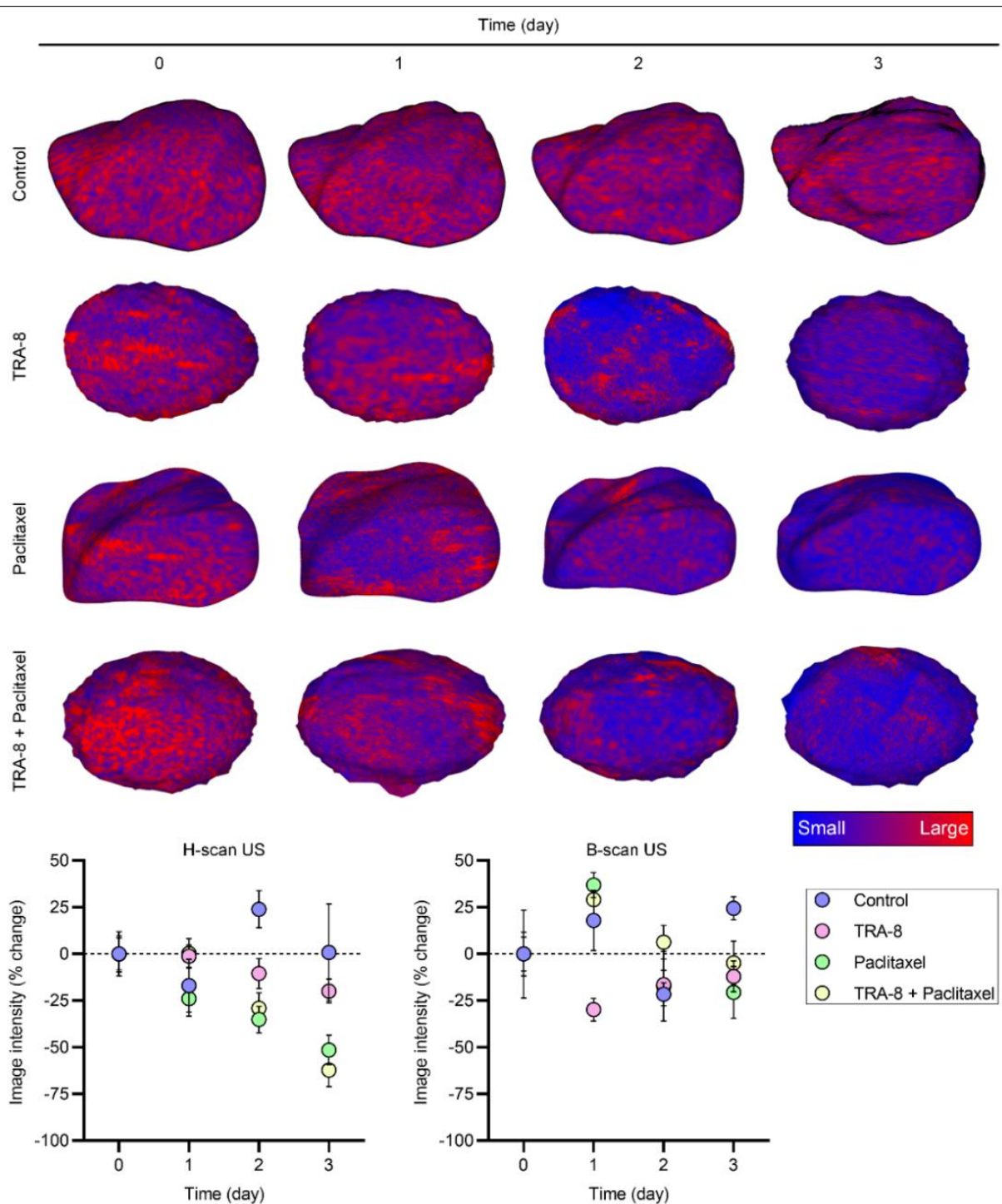


Figure 5.5. 3-D H-scan US image reconstructions from breast cancer-bearing mice at baseline (day 0) and days 1, 2 and 3 after receiving a single dose of control or chemotherapeutic drug, namely, TRA-8, paclitaxel, or TRA-8 + paclitaxel (top). A summary of *in vivo* H-scan US image intensities reveals a marked early response and trend not found in the B-scan US measures (bottom).

After ultrasound imaging on day 3, animals were humanely euthanized and tissue excised for histological processing. An example of matched H-scan US and histologic images depicting cancer cell proliferation (Ki67), apoptosis (AC3), and nuclear size (DAPI) are presented in Figure 5.6. These representative *in vivo* and *ex vivo* images from a TRA-8 + paclitaxel group mouse reveal breast tumor heterogeneity and a differential spatial response to therapy at termination. After summarizing intratumoral measurements from the entire histological cross-sections, significantly different levels of cell proliferation and apoptotic activity were found for both the control and treated tumors. Reported as a fraction of the entire tissue cross-section, proliferation activity was $24.4 \pm 2.2\%$ for the control group compared to the therapy groups, which were found to be $13.2 \pm 2.1\%$, $10.9 \pm 1.6\%$ and $4.2 \pm 1.6\%$ for the TRA-8, paclitaxel, and TRA-8 + paclitaxel, respectively ($p < 0.001$). Using a similar metric, apoptotic activity for the control group was $3.8 \pm 0.4\%$ and $18.2 \pm 1.9\%$, $19.3 \pm 0.7\%$ and $27.8 \pm 3\%$ for the TRA-8, paclitaxel, and TRA-8 + paclitaxel, respectively ($p < 0.001$). Lastly, DAPI-stained tissue sections allowed sensitive detection of cancer cell nuclei using fluorescent microscopy. Dedicated image processing algorithms were then used to measure mean nuclear diameter. While no significant differences were found between the control and TRA-8 or paclitaxel treated tumors, that is $21.2 \pm 1.5 \mu\text{m}$ versus 18.2 ± 1.3 and $16.9 \pm 1.7 \mu\text{m}$ ($p > 0.06$), mice administered the combination TRA-8 + paclitaxel therapy had tumor tissue with nuclear sizes that were significantly smaller at $15.8 \pm 1.2 \mu\text{m}$ ($p = 0.006$). Given the dense volume of H-scan ultrasound images, DAPA-stained tissue sections were resized and oriented to the same perspective.

Then the H-scan image that most closely matched the histologic section was selected for further analysis. After dividing each image into smaller nonoverlapping ROIs and ignoring areas with necrotic tissue, local H-scan ultrasound image intensity and nuclear size measures were summarized for both the control and treated tumor groups. It is noteworthy that there was a significant linear correlation between the local H-scan ultrasound image intensity and nuclear size ($R^2 > 0.51$, $p < 0.001$) (see Figure 5.6). Given TRA-8 and paclitaxel are apoptosis-inducing

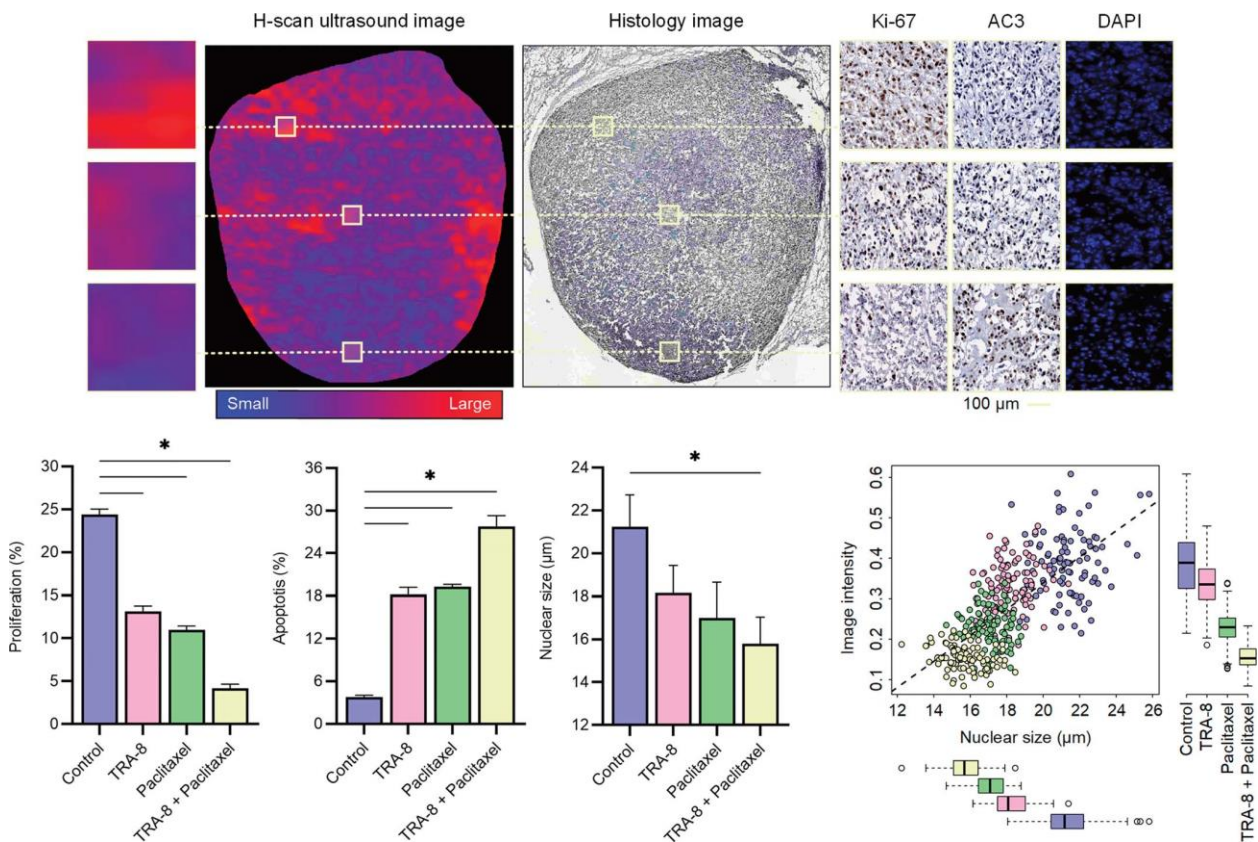


Figure 5.6. Comparison of matched H-scan US and histologic images depicting cell proliferation (Ki-67), apoptosis (AC3), and nuclear size (DAPI, top). Enlarged regions show breast tumor heterogeneity and a differential spatial response to neoadjuvant therapy as highlighted by the three distinct zoomed subregions. Bar plots summarize control tumor histologic measures and those administered a single dose of TRA-8, paclitaxel, or TRA-8 + paclitaxel (bottom left). A linear comparison of *in vivo* H-scan US image intensities and co-registered local measures of cancer cell nuclear size suggests that H-scan US imaging can detect increased apoptotic activity and cancer cell nuclear shrinkage in tumors administered neoadjuvant therapy. A * indicates $p < 0.05$ versus control data.

chemotherapeutic drugs, progressive changes in local H-scan ultrasound image intensity were due in part to varying levels of cell death and nuclear condensation.

In a second experiment, 3-D H-scan ultrasound imaging was again used to assess response to neoadjuvant therapy in luciferase-positive TNBC-bearing mice. Longitudinal bioluminescent images of tumor cell viability were also acquired and the main endpoint of this longer-term study was subject survival. A representative group of 3-D H-scan ultrasound image reconstructions and plots of group summary statistics are detailed in Figure 5.7. On average, results reveal that H-scan ultrasound images of the tumors exhibited a considerable blue shift at 72 h of therapy administration that are in good agreement with the independent measures depicted in Figure 5.5 ($p > 0.11$).

Thereafter, progressive intensity changes in the segmented H-scan ultrasound volumes were very pronounced for tumors undergoing chemotherapy, while the control group again appears mostly unchanged over the same longer-time interval. An analysis of repeat measures found a statistically significant change in H-scan ultrasound image intensities for all treated mice by day 7 ($p < 0.01$), but not for the control group ($p = 0.87$). These trends continued to become more pronounced on subsequent days up until the last H-scan ultrasound imaging session on day 14 and were comparable to bioluminescent image findings presented in Figure 5.8.

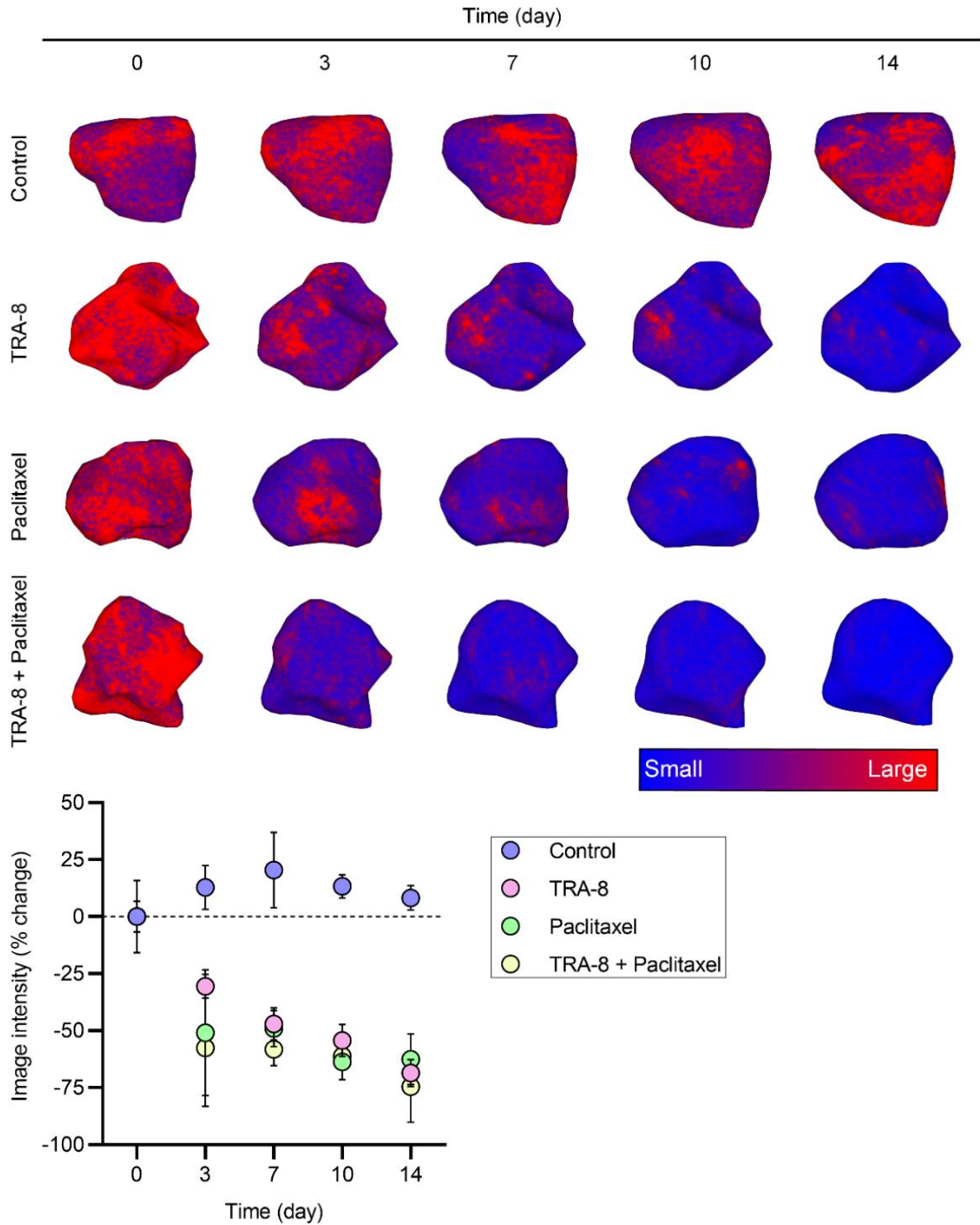


Figure 5.7. 3-D H-scan US image reconstructions of breast cancer-bearing mice after receiving a single dose of sham or neoadjuvant therapy (top). A summary of *in vivo* H-scan US image intensities reveals a considerable change and longer-term treatment response (bottom).

The optical images depict a progressive increase for the control group and reflects a progressive increase in viable cancer cells in the growing TNBCs. Conversely, tumors in the TRA-8, paclitaxel, and TRA-8 + paclitaxel treated mice exhibit progressive decreases suggestive of increased cell death. When tumor burden warranted, mice were euthanized up until the terminal endpoint of day 21. Survival curves detail a general improvement in subject outcomes following a single dose of neoadjuvant therapy compared to controls. These longer-term survival trends were less consistent than the *in vivo* H-scan ultrasound and optical imaging because several mice were euthanized prematurely due to tumor ulceration from the house bedding and not due to size limitation concerns.

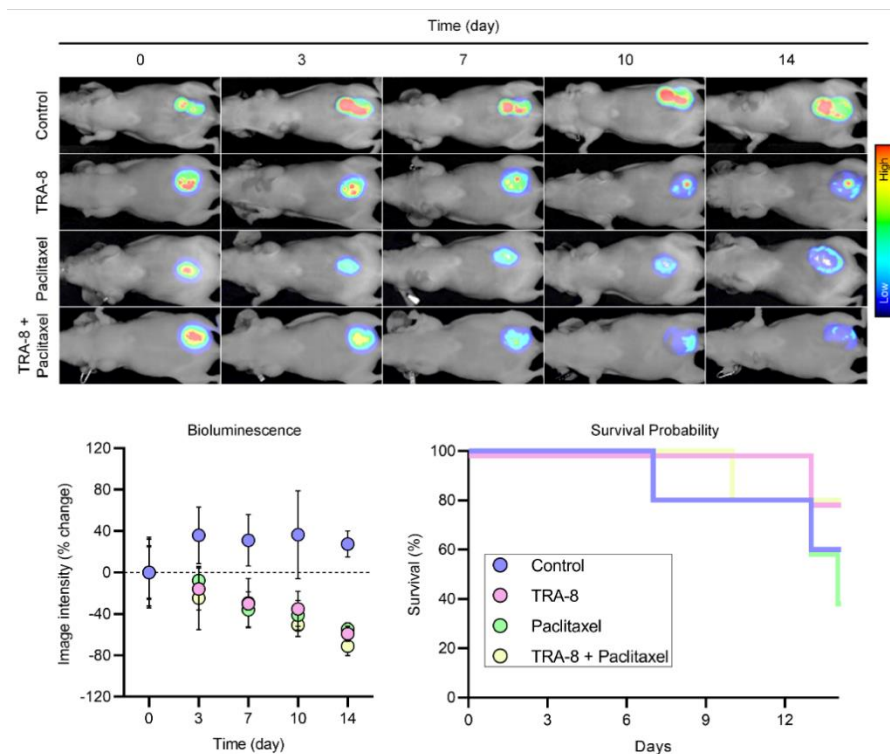


Figure 5.8. Whole body bioluminescent images of breast cancer-bearing mice at baseline (day 0) and days 3, 7, 10, and 14 after receiving a single dose of control or chemotherapeutic drug, namely, TRA-8, paclitaxel, or TRA-8 + paclitaxel (top). A summary of *in vivo* bioluminescent image intensities (bottom left) reveals a marked early response and trend comparable to that found using 3-D H-scan ultrasound imaging. Survival curves detail a general improvement in subject outcomes following neoadjuvant therapy compared to controls.

5.1.4 Discussion

During this research, we explored the use of 3-D H-scan ultrasound imaging to visualize heterogenous patterns in TNBC-bearing mice and characterization of tissue scatterers. During the shorter-term study, changes in H-scan ultrasound image intensity compared favorably to histologic measures at termination. Specifically, there was a decrease in the H-scan ultrasound signal following neoadjuvant therapy that coincided with increased cancer cell apoptosis and decreased proliferation, both hallmark features of a successful cancer treatment. Tumor response was most pronounced in the TRA-8 + paclitaxel treatment group mice, as TRA-8 is known to sensitize TNBC to paclitaxel.[42] Following measurement of cancer cell nuclear size from histological images, it was found that a strong correlation with the local H-scan ultrasound image intensity existed. During the longer-term study, changes in H-scan ultrasound imaging intensity were supported by those found using optical imaging and survival analysis. These collective findings suggest that *in vivo* 3-D H-scan ultrasound imaging can noninvasively detect an early TNBC response to neoadjuvant therapy (apoptosis-induced cell death) and within days of treatment initiation. It also can be inferred that spatial variations in ultrasound scatter size is more accurately depicted using H-scan ultrasound images compared to the conventional B-scan ultrasound imaging techniques [28].

During the H-scan ultrasound analysis and display, visualization of different scattering sizes and types are enabled by a matched filter approach involving different orders of Gaussian-weighted Hermite functions. Like the technology detailed in this paper, an H-scan ultrasound system employing a transducer with center frequencies in the 10 MHz range are suitable for clinical imaging of human breast. If available, use of a higher frequency and wideband array

transducer would further increase H-scan ultrasound sensitivity to tissue scatterer size.[28], [43] While the effects are less consequential during preclinical murine studies, depth-dependent attenuation in human tissues is more pronounced and will strongly influence the H-scan ultrasound analysis. Before clinical translation can be pursued, additional work is required to develop robust compensation strategies that minimize any depth-dependent biases.

Analysis of backscattered ultrasound signals is promising noninvasive approach to tissue characterization. For example, Kolios et al. used a spectral feature-based method to analyze backscattered ultrasound signals from aggregates of both normal healthy cells and cancer cells (like a simplified tumor model) treated with chemotherapeutic drugs.[44] Unlike measurements from the untreated cells, tissue characterization parameters from treated cell aggregates changed as a consequence of the decrease in effective scatterer size caused by nuclear condensation during apoptotic death. More recent studies provided additional evidence that these changes in ultrasound scattering were linked to the degree of chromatin condensation (density of nuclear material).[45], [46] As a greater fraction of tumor tissue undergoes cell death, a greater degree of chromatin condensation and possibly fragmentation is expected to occur.[47] In a large cohort of breast cancer patients, Czarnota et al. detailed how quantitative ultrasound imaging and spatial heterogeneities in size and spacing of ultrasound scatterers could predict response to neoadjuvant therapy within weeks of treatment initiation.[48] Furthermore, tissue characterization features in the core and margin of breast tumors can predict five-year recurrence free survival.[49] Preclinical H-scan ultrasound imaging findings presented herein are in good agreement with several of the conclusions from these pioneering *in vitro* and *in vivo* studies. An advantage of our 3-D H-scan ultrasound approach is it provides information in volumetric space throughout the entire cancer

burden. However, the absolute value of this volumetric data (like spatial heterogeneity) and comparison to an established quantitative ultrasound method needs to be carefully explored. Future work will also integrate a deep learning modeling approach with *in vivo* 3-D H-scan ultrasound imaging to allow quantitative estimation of actual scatterer size.[34] This innovation will require a rather large amount of labeled image data (for model training and testing) that is spatially registered to known histological measurements, which was not feasible using the limited data collected for the current study.

3-D H-scan ultrasound imaging was performed using a wobbler transducer that includes mechanically sweeping a linear array transducer to capture volumetric data from a spatial series of ultrasound images. The advantage of this mechanical scanner is low cost, and relatively low power consumption. The disadvantage includes reverberation artifacts caused by an impedance mismatch between oil and the transducer lens. Given these reverberation artifacts would presumably compromise any tissue characterization attempts, future work could investigate use of 3-D H-scan ultrasound imaging using a 2-D matrix array transducer. While allowing electronic beam steering and considerably higher volume imaging rates if needed, these matrix arrays are devoid of mechanical parts that are prone to failure. Techniques for the mechanical characterization of tissue have been detailed and preliminary results are encouraging.[50], [51]

5.1.5 Conclusions

Overall, it was shown that *in vivo* 3-D H-scan ultrasound imaging is a promising technique that allows visualization of the heterogeneous tumor microenvironment in a mouse model of TNBC. H-scan ultrasound imaging was also considerably more sensitive to tumor changes after apoptosis-inducing drug therapy as compared to traditional B-scan ultrasound. While there was no difference

at baseline ($p > 0.99$), H-scan ultrasound results from treated tumors exhibited progressive decreases in image intensity (up to 62.2% by day 3) that had a significant linear correlation with cancer cell nuclear size ($R^2 > 0.51$, $p < 0.001$). In short, the proposed 3-D H-scan methodology was validated by two independent *in vivo* studies and *ex vivo* histological measures. Nuclear size was shown to have a strong linear correlation with local H-scan ultrasound image intensity that also coincided with biomarkers of cancer cell death like apoptosis.

5.1.6 References

- [1] R. L. Siegel, K. D. Miller, H. E. Fuchs, and A. Jemal, “Cancer statistics, 2021,” *CA Cancer J Clin*, vol. 71, no. 1, pp. 7–33, 2021.
- [2] L. J. Graham *et al.*, “Current approaches and challenges in monitoring treatment responses in breast cancer,” *J. Cancer*, vol. 5, no. 1, pp. 58–68, 2014.
- [3] L. N. Harris *et al.*, “Molecular subtypes of breast cancer in relation to paclitaxel response and outcomes in women with metastatic disease: results from CALGB 9342,” *Breast Cancer Res. BCR*, vol. 8, no. 6, p. R66, 2006.
- [4] L. A. Carey *et al.*, “Race, breast cancer subtypes, and survival in the Carolina Breast Cancer Study,” *JAMA*, vol. 295, no. 21, pp. 2492–2502, 2006.
- [5] C. Liedtke *et al.*, “Response to neoadjuvant therapy and long-term survival in patients with triple-negative breast cancer,” *J. Clin. Oncol.*, vol. 26, no. 8, pp. 1275–1281, 2008.
- [6] R. D. Chacón and M. V. Costanzo, “Triple-negative breast cancer,” *Breast Cancer Res. BCR*, vol. 12 Suppl 2, p. S3, 2010.
- [7] E. C. Dietze, C. Sistrunk, G. Miranda-Carboni, R. O’Regan, and V. L. Seewaldt, “Triple-negative breast cancer in African-American women: Disparities versus biology,” *Nat. Rev. Cancer*, vol. 15, no. 4, pp. 248–254, 2015.
- [8] M. J. Arends and A. H. Wyllie, “Apoptosis: mechanisms and roles in pathology,” *Int. Rev. Exp. Pathol.*, vol. 32, pp. 223–254, 1991.
- [9] P. W. Mesner, I. I. Budihardjo, and S. H. Kaufmann, “Chemotherapy-induced apoptosis,” *Adv. Pharmacol. San Diego Calif*, vol. 41, pp. 461–499, 1997.

- [10] T. A. D. A.-A. Tengku Din, A. Seeni, W.-N. M. Khairi, S. Shamsuddin, and H. Jaafar, "Effects of rapamycin on cell apoptosis in MCF-7 human breast cancer cells," *Asian Pac. J. Cancer Prev. APJCP*, vol. 15, no. 24, pp. 10659–10663, 2014.
- [11] H. Shen, S. Zhao, Z. Xu, L. Zhu, Y. Han, and J. Ye, "Evodiamine inhibits proliferation and induces apoptosis in gastric cancer cells," *Oncol. Lett.*, vol. 10, no. 1, pp. 367–371, 2015.
- [12] T. R. Wilson, P. G. Johnston, and D. B. Longley, "Anti-apoptotic mechanisms of drug resistance in cancer," *Curr. Cancer Drug Targets*, vol. 9, no. 3, pp. 307–319, 2009.
- [13] X. Li *et al.*, "Autophagy: A novel mechanism of chemoresistance in cancers," *Biomed. Pharmacother.*, vol. 119, p. 109415, 2019.
- [14] E. A. Eisenhauer *et al.*, "New response evaluation criteria in solid tumours: revised RECIST guideline," *Eur. J. Cancer*, vol. 45, no. 2, pp. 228–247, 2009.
- [15] K. Brindle, "New approaches for imaging tumour responses to treatment," *Nat. Rev. Cancer*, vol. 8, no. 2, pp. 94–107, 2008.
- [16] U. Sharma, K. K. A. Danishad, V. Seenu, and N. R. Jagannathan, "Longitudinal study of the assessment by MRI and diffusion-weighted imaging of tumor response in patients with locally advanced breast cancer undergoing neoadjuvant chemotherapy," *NMR Biomed.*, vol. 22, no. 1, pp. 104–113, 2009.
- [17] N. Houssami, R. M. Turner, and M. Morrow, "Meta-analysis of pre-operative magnetic resonance imaging (MRI) and surgical treatment for breast cancer," *Breast Cancer Res. Treat.*, vol. 165, no. 2, pp. 273–283, 2017.
- [18] E. Ong, "Preoperative imaging for breast conservation surgery - Do we need more than conventional imaging for local disease assessment?," *Gland Surg.*, vol. 7, no. 6, pp. 554–559, 2018.
- [19] B. K. Patel *et al.*, "Contrast-enhanced spectral mammography is comparable to MRI in the assessment of residual breast cancer following neoadjuvant systemic therapy," *Ann. Surg. Oncol.*, vol. 25, no. 5, pp. 1350–1356, 2018.
- [20] E. F. Jones *et al.*, "Current landscape of breast cancer imaging and potential quantitative imaging markers of response in ER-positive breast cancers treated with neoadjuvant therapy," *Cancers*, vol. 12, no. 6, 2020.
- [21] S. Wang, J. A. Hossack, and A. L. Klibanov, "From anatomy to functional and molecular biomarker imaging and therapy: Ultrasound is safe, ultrafast, portable, and inexpensive," *Invest. Radiol.*, vol. 55, no. 9, pp. 559–572, 2020.

- [22] J. M. Thijssen, “Ultrasonic tissue characterisation and echographic imaging,” *Phys. Med. Biol.*, vol. 34, no. 11, pp. 1667–1674, Nov. 1989.
- [23] H. Tadayyon *et al.*, “Quantitative ultrasound assessment of breast tumor response to chemotherapy using a multi-parameter approach,” *Oncotarget*, vol. 7, no. 29, pp. 45094–45111, 2016.
- [24] M. L. Oelze and J. Mamou, “Review of quantitative ultrasound: Envelope statistics and backscatter coefficient imaging and contributions to diagnostic ultrasound,” *IEEE Trans. Ultrason. Ferroelectr. Freq. Control*, vol. 63, no. 2, pp. 336–351, 2016.
- [25] H. G. Nasief, I. M. Rosado-Mendez, J. A. Zagzebski, and T. J. Hall, “A quantitative ultrasound-based multi-parameter classifier for breast masses,” *Ultrasound Med. Biol.*, vol. 45, no. 7, pp. 1603–1616, 2019.
- [26] M. Oelze, “Quantitative ultrasound successes: Past, present and future,” *SPIE Med. Imaging*, vol. 11319, pp. 1–6, 2020.
- [27] K. J. Parker, “Scattering and reflection identification in H-scan images,” *Phys. Med. Biol.*, vol. 61, no. 12, pp. L20–28, 2016.
- [28] M. Khairalseed, K. Hoyt, J. Ormachea, A. Terrazas, and K. J. Parker, “H-scan sensitivity to scattering size,” *J. Med. Imaging*, vol. 4, no. 4, p. 043501, 2017.
- [29] M. Khairalseed, K. Brown, K. J. Parker, and K. Hoyt, “Real-time H-scan ultrasound imaging using a Verasonics research scanner,” *Ultrasonics*, vol. 94, pp. 28–36, 2019.
- [30] M. Khairalseed, K. Javed, G. Jashkaran, J.-W. Kim, K. J. Parker, and K. Hoyt, “Monitoring early breast cancer response to neoadjuvant therapy using H-scan ultrasound imaging: Preliminary preclinical results,” *J. Ultrasound Med.*, vol. 38, no. 5, pp. 1259–1268, 2019.
- [31] M. Khairalseed, F. Xiong, J.-W. Kim, R. F. Mattrey, K. J. Parker, and K. Hoyt, “Spatial angular compounding technique for H-scan ultrasound imaging,” *Ultrasound Med. Biol.*, vol. 44, no. 1, pp. 267–277, 2018.
- [32] M. Khairalseed, G. Rijal, and K. Hoyt, “Spatial comparison between the H-scan format for classification of ultrasound scatterers and histology - Preliminary results using an animal model of breast cancer,” *Proc IEEE Ultrason Symp*, pp. 1–4, 2020.
- [33] M. Khairalseed, G. Rijal, and K. Hoyt, “H-scan format for classification of ultrasound scatterers and matched comparison to histology measurements,” *Proc IEEE Int Symp Biomed. Imaging*, vol. 1, pp. 1820–1823, 2020.

- [34] H. Tai, M. Khairalseed, and K. Hoyt, “3-D H-scan ultrasound imaging and use of a convolutional neural network for scatterer size estimation,” *Ultrasound Med. Biol.*, vol. 46, no. 10, pp. 2810–2818, 2020.
- [35] G. Turashvili and E. Brogi, “Tumor heterogeneity in breast cancer,” *Front. Med.*, vol. 4, 2017.
- [36] R. E. Ellsworth, H. L. Blackburn, C. D. Shriver, P. Soon-Shiong, and D. L. Ellsworth, “Molecular heterogeneity in breast cancer: State of the science and implications for patient care,” *Semin. Cell Dev. Biol.*, vol. 64, pp. 65–72, 2017.
- [37] H. Tai, M. Khairalseed, and K. Hoyt, “Adaptive attenuation correction during H-scan ultrasound imaging using K-means clustering,” *Ultrasonics*, vol. 102, p. 105987, 2020.
- [38] H. Tai, M. Khairalseed, and K. Hoyt, “3D H-scan ultrasound imaging system and method for acoustic scatterer size estimation – Preliminary studies using phantom materials,” *Proc IEEE Ultrason Symp*, pp. 1515–1518, 2019.
- [39] H. Tai, S. Dolui, M. Khairalseed, and K. Hoyt, “Three-dimensional voxel-level classification of ultrasound scattering,” *Proc IEEE Int Symp Biomed. Imaging*, vol. 1, pp. 1838–1841, 2020.
- [40] J. Ma, J. Jiang, H. Zhou, J. Zhao, and X. Guo, “Guided locality preserving feature matching for remote sensing image registration,” *IEEE Trans. Geosci. Remote Sens.*, vol. 56, no. 8, pp. 4435–4447, 2018.
- [41] H. Xu, C. Lu, R. Berendt, N. Jha, and M. Mandal, “Automatic nuclear segmentation using multiscale radial line scanning with dynamic programming,” *IEEE Trans. Biomed. Eng.*, vol. 64, no. 10, pp. 2475–2485, 2017.
- [42] K. Hoyt, A. Sorace, and R. Saini, “Volumetric contrast-enhanced ultrasound imaging to assess early response to apoptosis-inducing anti-death receptor 5 antibody therapy in a breast cancer animal model,” *J. Ultrasound Med.*, vol. 31, no. 11, pp. 1759–1766, 2012.
- [43] M. Khairalseed and K. Hoyt, “Integration of a CMUT linear array for wideband H-scan ultrasound imaging,” *Proc IEEE Ultrason Symp*, vol. 1, pp. 1519–1522, 2019.
- [44] M. C. Kolios, G. J. Czarnota, M. Lee, J. W. Hunt, and M. D. Sherar, “Ultrasonic spectral parameter characterization of apoptosis,” *Ultrasound Med. Biol.*, vol. 28, no. 5, pp. 589–597, 2002.
- [45] M. Pasternak *et al.*, “Effect of chromatin structure on quantitative ultrasound parameters,” *Oncotarget*, vol. 8, no. 12, pp. 19631–19644, 2017.
- [46] M. M. Pasternak *et al.*, “High-frequency ultrasound detection of cell death: Spectral differentiation of different forms of cell death in vitro,” *Oncoscience*, vol. 3, no. 9–10, pp. 275–287, 2016.

- [47] G. J. Czarnota *et al.*, “Ultrasound imaging of apoptosis: High-resolution non-invasive monitoring of programmed cell death in vitro, in situ and in vivo,” *Br. J. Cancer*, vol. 81, no. 3, pp. 520–527, 1999.
- [48] A. Sadeghi-Naini *et al.*, “Chemotherapy-response monitoring of breast cancer patients using quantitative ultrasound-based intra-tumour heterogeneities,” *Sci. Rep.*, vol. 7, no. 1, p. 10352, 2017.
- [49] H. Tadayyon *et al.*, “A priori prediction of neoadjuvant chemotherapy response and survival in breast cancer patients using quantitative ultrasound,” *Sci. Rep.*, vol. 7, no. 1, p. 45733, 2017.
- [50] J.-L. Gennisson *et al.*, “4-D ultrafast shear-wave imaging,” *IEEE Trans. Ultrason. Ferroelectr. Freq. Control*, vol. 62, no. 6, pp. 1059–1065, 2015.
- [51] J. Provost *et al.*, “3D ultrafast ultrasound imaging in vivo,” *Phys. Med. Biol.*, vol. 59, no. 19, pp. 1–13, 2014.

5.2 Part 2

5.2.1 Introduction

Breast cancer accounts for 30% of all new cancer diagnoses in women [1]. Despite encouraging clinical advances that have spurred a decline in mortality, breast cancer remains a major public health and economic issue. For many breast cancer patients, neoadjuvant chemotherapy is the standard of care. Several clinical studies have demonstrated that an early response to neoadjuvant chemotherapy is a good predictor of a patient's long-term survival [2]. Therefore, a responsive adaptive chemotherapy selection in the neoadjuvant setting could improve the cure rate and prognosis of breast cancer patients. This highlights the importance of early predictions of patient response to neoadjuvant chemotherapy.

A major challenge in monitoring neoadjuvant chemotherapy is how to detect and accurately quantify response at an early stage of drug treatment. The use of noninvasive ultrasound (US) for monitoring this tumor response has been the focus of research efforts for decades. Several promising quantitative US-based tissue characterization methods have been introduced like backscatter classification and spectral feature extraction [3]. These approaches examine the frequency content of backscattered US signals to extract quantitative parameters linked to the tumor microstructure [4]. However, these techniques routinely use a kernel of data for tissue parameter estimation, which introduces a fundamental tradeoff between estimator accuracy and spatial resolution.

To help overcome limitations of the more traditional tumor tissue characterization approaches and to simplify the procedure, the hue-scanning (H-scan) US imaging technique has emerged [5]. This newer modality depicts subtle changes in the tissue microstructure that are

otherwise invisible during B-scan US imaging, thereby adding new information to a diagnostic US examination. In approach, the H-scan US format links the mathematics of Gaussian-weighted Hermite (GH) functions to the physics of scattering and reflection from different-sized tissue components. In general, lower frequency signal content is generated from larger scattering structures whereas higher frequency backscattered US signal content is produced by an US wave interacting with small scatterers of scale below the wavelength of the US transmit pulse (i.e., Rayleigh scatterers) [6], [7]. The purpose of this study was to introduce a new 3-dimensional (3-D) H-scan US imaging technique for investigating an early chemotherapy response in breast cancer-bearing mice. US findings were then compared to measurements from diffusion-weighted magnetic resonance imaging (DW-MRI) and histological analysis of excised tumor tissue samples.

5.2.2 Materials and Methods

5.2.2.1 Animal Preparation

All protocols were approved by the Institutional Animal Care and Use Committee (IACUC) at the University of Texas at Dallas. Preclinical studies were conducted using six-week-old female nude athymic mice (N = 18, Charles River Laboratories, Wilmington, MA) orthotopically implanted with 1 million breast cancer cells (MDA-MB-231, American Type Culture Collection, Manassas, VA). When tumor size reached 6 to 8 mm (maximum diameter), mice were divided into three groups and administered the following intraperitoneal injections: (1) 5 mg/kg of sterile saline (sham drug), (2) 5 mg/kg of cisplatin, or (3) 25 mg/kg cisplatin. The animals were treated biweekly. All US and MRI scans were performed at baseline before drug injection and again at days 1, 3, and 7.

5.2.2.2 Ultrasound Data Acquisition and H-scan Processing

US imaging was performed using a Vevo 3100 system (FUJIFILM VisualSonics Inc) equipped with an MX201 linear array transducer. This 256-element (0.125 mm pitch) transducer was operated at a 15 MHz center frequency. Volumetric data acquisitions were acquired by fixing the transducer to a motorized stage and then collecting a series of US images at discrete positions that are equally spaced 50 μm apart. Using custom MATLAB software (MathWorks Inc, Natick, MA), all US data underwent attenuation correction for depth-dependent signal loss [8]. To generate the H-scan US images, two parallel convolutional filters comprised of 2nd and 8th-order GH polynomials (GH2 and GH8) were applied to measure the relative strength of the backscattered US signals [9]. After normalization and envelope detection, lower frequency signals were assigned to a red (R) channel and the higher frequency components to a blue (B) channel. The unfiltered original RF signal was assigned to the green (G) channel to complete the RGB colormap and final H-scan US volume reconstruction [10].

5.2.2.3 Magnetic Resonance Data Acquisition

MRI data acquisitions were performed using a 3 T preclinical system (BioSpec 3T, Bruker, Billerica, MA) equipped with a mouse body coil. Images were acquired using a pulsed-gradient spin echo sequence with a TR/TE (repetition time/echo time) of 30 ms and b-value set to 650 s/mm^2 . Using vendor software (ParaVision 360, Bruker Corp), apparent diffusion coefficient (ADC) maps generated. A region-of-interest (ROI) was then placed to encompass the tumor volume before calculation of the mean ADC value.

5.2.2.4 *Ex vivo* Processing of Tumor Tissue

Immediately after the last imaging session, animals were humanely euthanized via cervical dislocation under deep anesthesia. Tumors were surgically excised and fixed in neutral-buffered formalin for 7 d at room temperature. After complete fixation, tissue samples were embedded in paraffin and thin 5 μm sections were prepared from the blocks. To help identify the cell nucleus, tissue sections were repeatedly treated with a 4',6-diamidino-2-phenylindole (DAPI) solution (1 $\mu\text{g}/\text{mL}$, Thermal Fisher Scientific) and washed with phosphate buffered saline (PBS). Slides were mounted with fluorescent mounting media (HCO8, Millipore, Burlington, VT). Finally, whole tumor tissue sections were scanned and digitized using a fluorescence microscope equipped with a motorized volumetric scanning stage (Axio Observer 7, Carl Zeiss Inc, Thornwood, NY) and a fluorescent filter for DAPI ($\lambda = 461 \text{ nm}$). Lastly, digital histology images were analyzed using custom image processing software to quantify nuclear size throughout each tumor tissue section [11].

5.2.2.5 Statistical Analysis

Group data was summarized as mean \pm SD. A mixed-effects one-way analysis of variance (ANOVA) test was performed to make comparisons between group measurements. A p-value less than 0.05 was considered statistically significant. All statistical analyses were performed using Prism 9.0 (GraphPad Software, San Diego, CA).

5.2.3 Results and Discussion

Example 3-D H-scan US image reconstructions and plots of group summary statistics are depicted in Figure 5.9. Inspection of the segmented US volumes reveals subtle patterns of spatial heterogeneity along the tumor periphery. While no differences in H-scan US image intensity were found at baseline ($p > 0.99$), repeat images at days 1, 3, and 7 reveal a progressive blue hue shift for tumors that were undergoing chemotherapy, while the control group tumors appear unchanged. Compared to baseline H-scan US image intensity levels, there were pronounced increases of $36.4 \pm 6.9\%$ and $43.8 \pm 8.1\%$ at day 7 for the low and high dose cisplatin treated tumors, respectively. A similar analysis of repeat B-scan US images (not shown) found no differences for any of the treatment group measures ($p > 0.92$).

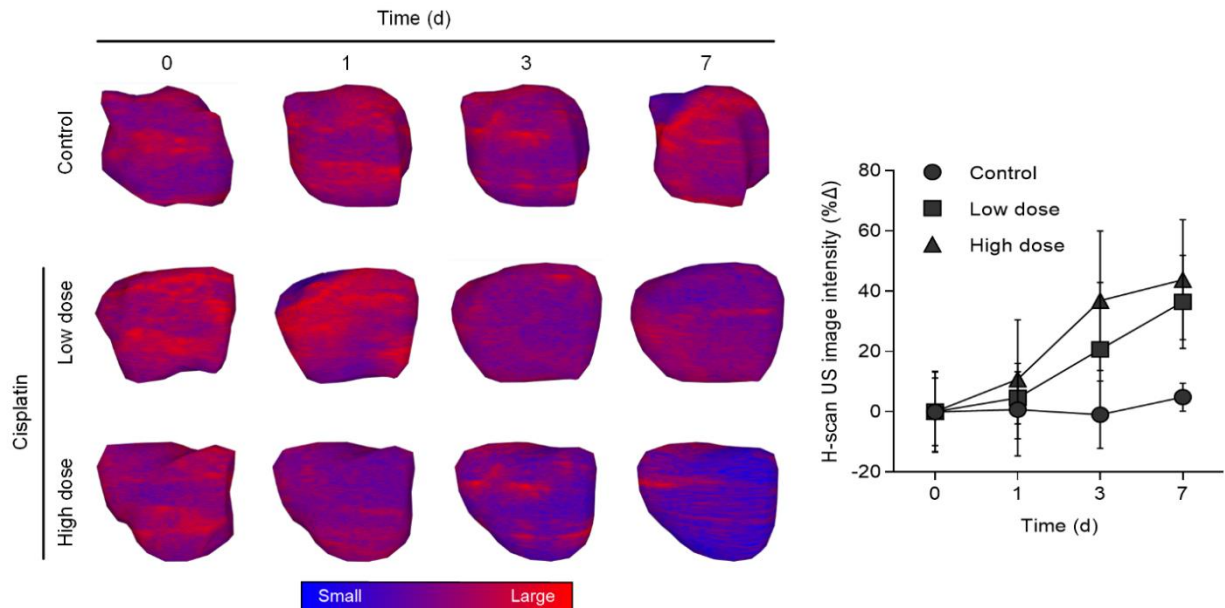


Figure 5.9. Representative H-scan ultrasound (US) tumor volume reconstructions from breast cancer-bearing mice at baseline (day 0) and days 1, 3, and 7 after the start of control treatment or chemotherapy using 3 mg/kg (low dose) or 25 mg/kg (high dose) of cisplatin. A summary of H-scan US image intensities reveals marked intratumoral changes in the drug dosed animals versus those treated with sham drug.

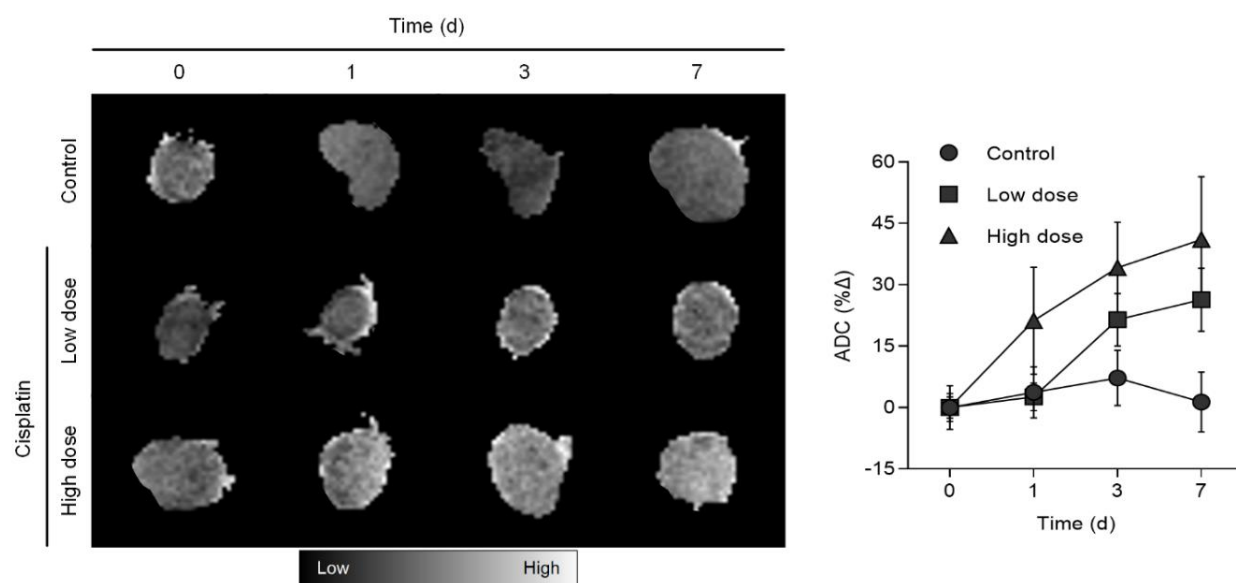


Figure 5.10. Representative diffusion-weighted magnetic resonance imaging (DW-MRI)-derived apparent diffusion coefficient (ADC) maps of breast cancer-bearing mice at baseline (day 0) and days 1, 3 and 7 after the start of control treatment or chemotherapy. A summary of ADC values reveals marked intratumoral changes in the drug dosed animals versus those treated with sham drug.

ADC maps were derived from DW-MRI data acquisitions. Inspection of the DW-MRI sequences presented in Figure 5.10 reveals progressive dose-related increases in intratumoral ADC values for animals undergoing chemotherapy. Relative to control group changes after 7 d, mean ADC values from the low and high dose cisplatin treated tumors were significantly increased, $1.3 \pm 7.3\%$, $26.4 \pm 7.7\%$, and $41.1 \pm 15.4\%$, respectively ($p < 0.01$). These observation were attributed to elevated water mobility following induced cancer cell apoptotic activity within the bulk tumor mass.

After US and MRI studies on day 7, animals were humanely euthanized and tissue was excised for histological processing. As illustrated in Figure 5.11, fluorescent microscopy imaging of DAPI stained tumor tissue sections allowed visualization of the spatial location and distribution pattern of cancer cell nuclei. Digitized DAPI images were then processed to compute measurements of cancer cell nuclear size. Specifically, mean nuclear size was found to be $17.2 \pm$

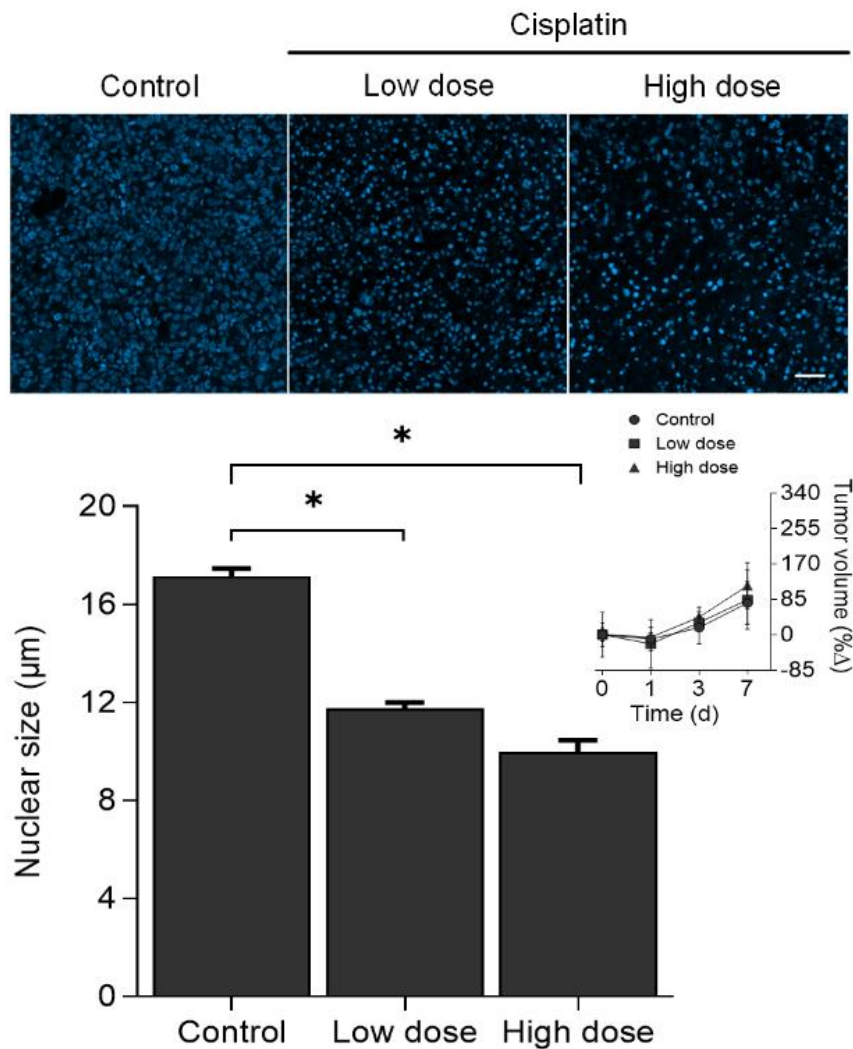


Figure 5.11. Example histological images after staining for nuclear location (DAPI, top). A summary of cancer cell nuclear size measurements are provided for tumors administered control treatment or chemotherapy using 3 mg/kg (low dose) or 25 mg/kg (high dose) of cisplatin (bottom). No changes in tumor size were noted during the experimental period. A * indicates a p-value less than 0.05 versus controls.

2.5 μm in control tumors versus 11.8 ± 2.1 and 9.9 ± 3.2 μm in tumors treated with low and high dose cisplatin, respectively ($p < 0.02$).

Previous research has shown that in highly cellular tissue like tumors, the cancer cell nucleus is up 10-times stiffer than the surrounding cytoplasm [12] and helps contribute to backscattered US signals. Likewise, our group has shown that the local H-scan US image intensity is linearly related to cancer cell nuclear size and spatial distancing [11], [13], [14]. It is not surprising that US-derived measurements reflective of scatterer spacing and organization have been used to differentiate normal from pathological tissue [15]. A number of preclinical studies have also shown that tissue characterization using various US techniques are effective resources for detecting tumor response to a variety of anticancer therapies including chemotherapy [16], [17]. This supports the findings of this present study and further highlights the potential of H-scan US imaging for assessing an early tumor response to apoptosis-inducing drugs.

5.2.4 Conclusion

3-D H-scan US imaging was implemented using a preclinical scanner and shown to be a promising approach for monitoring early cancer response to neoadjuvant chemotherapy. These US results were validated by independent findings from DW-MRI and histological analysis of excised tumor tissue samples.

5.2.5 Acknowledgements

This research was supported by the National Institutes of Health (NIH) grant R01CA269973 and R01EB025841, and Cancer Prevention and Research Institute of Texas (CPRIT) award RP180670.

5.2.6 References

- [1] R. L. Siegel, K. D. Miller, H. E. Fuchs, and A. Jemal, “Cancer statistics, 2022,” *CA Cancer J Clin*, vol. 72, no. 1, pp. 7–33, 2022.
- [2] H. Wang and X. Mao, “Evaluation of the efficacy of neoadjuvant chemotherapy for breast cancer,” *Drug Des. Devel. Ther.*, vol. 14, pp. 2423–2433, 2020.
- [3] M. L. Oelze and J. Mamou, “Review of quantitative ultrasound: Envelope statistics and backscatter coefficient imaging and contributions to diagnostic ultrasound,” *IEEE Trans. Ultrason. Ferroelectr. Freq. Control*, vol. 63, no. 2, pp. 336–351, 2016.
- [4] H. Tadayyon, A. Sadeghi-Naini, L. Wirtzfeld, F. C. Wright, and G. Czarnota, “Quantitative ultrasound characterization of locally advanced breast cancer by estimation of its scatterer properties,” *Med. Phys.*, vol. 41, no. 1, p. 012903, 2014.
- [5] K. J. Parker, “Scattering and reflection identification in H-scan images,” *Phys. Med. Biol.*, vol. 61, no. 12, pp. L20-28, 2016.
- [6] M. Khairalseed, K. Hoyt, J. Ormachea, A. Terrazas, and K. J. Parker, “H-scan sensitivity to scattering size,” *J. Med. Imaging*, vol. 4, no. 4, p. 043501, 2017.
- [7] M. Khairalseed, K. Brown, K. J. Parker, and K. Hoyt, “Real-time H-scan ultrasound imaging using a Verasonics research scanner,” *Ultrasonics*, vol. 94, pp. 28–36, 2019.
- [8] H. Tai, M. Khairalseed, and K. Hoyt, “Adaptive attenuation correction during H-scan ultrasound imaging using K-means clustering,” *Ultrasonics*, vol. 102, p. 105987, 2020.
- [9] M. Khairalseed, F. Xiong, J.-W. Kim, R. F. Mattrey, K. J. Parker, and K. Hoyt, “Spatial angular compounding technique for H-scan ultrasound imaging,” *Ultrasound Med. Biol.*, vol. 44, no. 1, pp. 267–277, 2018.
- [10] H. Tai, M. Khairalseed, and K. Hoyt, “3-D H-scan ultrasound imaging and use of a convolutional neural network for scatterer size estimation,” *Ultrasound Med. Biol.*, vol. 46, no. 10, pp. 2810–2818, 2020.
- [11] H. Tai, J. Song, J. Li, S. Reddy, M. Khairalseed, and K. Hoyt, “Three-dimensional H-scan ultrasound imaging of early breast cancer response to neoadjuvant therapy in a murine model,” *Invest. Radiol.*, vol. 57, no. 4, pp. 222–232, 2022.
- [12] J. Lammerding, “Mechanics of the nucleus,” *Compr. Physiol.*, vol. 1, no. 2, pp. 783–807, 2011.

- [13] M. Khairalseed, G. Rijal, and K. Hoyt, "Spatial comparison between the H-scan format for classification of ultrasound scatterers and histology - Preliminary results using an animal model of breast cancer," Proc IEEE Ultrason Symp, pp. 1–4, 2020.
- [14] M. Khairalseed, G. Rijal, and K. Hoyt, "H-scan format for classification of ultrasound scatterers and matched comparison to histology measurements," Proc IEEE Int Symp Biomed. Imaging, vol. 1, pp. 1820–1823, 2020.
- [15] M. Khairalseed et al., "Classification of thyroid nodules in H-scan ultrasound images using texture and principal component analysis," Proc IEEE Lat. Am Ultrason Symp, pp. 1–4, 2021.
- [16] M. Khairalseed, K. Javed, G. Jashkaran, J.-W. Kim, K. J. Parker, and K. Hoyt, "Monitoring early breast cancer response to neoadjuvant therapy using H-scan ultrasound imaging: Preliminary preclinical results," J. Ultrasound Med., vol. 38, no. 5, pp. 1259–1268, 2019.
- [17] A. Sadeghi-Naini et al., "Low-frequency quantitative ultrasound imaging of cell death in vivo," Med. Phys., vol. 40, no. 8, p. 082901, 2013.

CHAPTER 6

CONCLUSIONS AND FUTURE WORK

6.1 Conclusions

Preliminary preclinical findings using both *in vitro* and *in vivo* H-scan US have indicated this new quantitative US imaging technique may be useful for detecting apoptotic activity and acute response to neoadjuvant chemotherapy. The model was used to compare biological tissues, and the initial analyses of the H-scan US images revealed distinct color patterns related to the underlying scattering behavior. More specifically, experimental work performed by our group has shown visual changes in scatterer size on the order of 15 to 250 μm in phantom materials with H-scan US imaging. After the development of a real-time H-scan US imaging system and using a murine xenograft model, our group demonstrated this new and innovative imaging modality could detect early response to neoadjuvant treatment.

To make H-scan US a more robust and reliable modality for human imaging, the matched Gaussian-weighted Hermite polynomial functions must be properly set for the initial pulse sequence and then continuously readjusted at tissue depth as high-frequency spectral content is progressively attenuated. To compensate for frequency-dependent attenuation at tissue depth, we adaptively adjusted the two spectral windows using the K-means clustering technique, optimizing H-scan US results for data collected from heterogeneous tissue (Figure 3.5). Another challenge associated with translating current H-scan US research to clinical practice is cancer heterogeneity, which causes different drug sensitivities at varying tumor subregions. With that said, utilizing 3-D H-scan US imaging to capture data from the entire tumor burden can fundamentally improve any tissue characterization strategy and treatment response determination. Therefore, a real-time

3D H-scan US imaging system equipped with customized two-dimensional (2D) 1024-element (32 x 32) matrix array (chapter 2) and wobbler (chapter 4) US transducers was developed to produce more robust tumor statistical analyses. *In vitro* results indicate that 3D H-scan US imaging technique can detect acoustic scatterers of varying size ($p < 0.01$, Figure 2.8) and is independent of scatterer concentration ($p > 0.05$, Figure 4.3). Furthermore, the developed H-scan US shows a rapid change in image intensity with increased scatterer size ($> 200\%$) compared to a slight increase observed in the B-mode US images ($< 30\%$, Figure 4.5). This suggests H-scan US imaging is more sensitive than B-scan US to changes in scatterer size. Additionally, our preliminary *in vivo* study suggests acute changes in the H-scan US signal amplitude were shown to strongly correlate with apoptotic activity (Figure 5.7). With cell shrinkage, the cells are smaller in size, the cytoplasm is dense, and the organelles are more tightly packed, which was suggested to be due to fundamental differences in scatterer size distributions (Figure 5.6 and 5.8). Our repeated *in vivo* study found a strong linear relationship between nuclear size and H-scan US image intensity, indicating apoptosis is one of the important factors that contribute to US signal changes.

In Chapter 2, we developed a 3D H-scan US imaging system and method for voxel-level classification of US scattering. To investigate theoretical considerations supporting this new H-scan US technology, a detailed simulation program was developed. This simulation helps provide insight into existing US technology and can inform future developments. The overarching purpose of the research presented herein was to study and evaluate the sensitivity of 3D H-scan US to scatterer objects and compare to co-registered B-scan US findings. We investigated the feasibility of using US imaging to detect relative changes in scatterer size for a series of homogeneous

phantom materials in simulation and experimentation. Overall, our hypothesis was that H-scan US imaging would be more sensitive to variations in scatterer size than traditional B-scan US.

In Chapter 3, we developed a deep network for spatiotemporal filtering to be used with the H-scan US imaging method for tissue characterization across different organs in the lateral direction. A compensation strategy involving an adaptive K-means clustering algorithm was introduced in this chapter to adjust GH polynomials based on RF signal spectrum changes at different depths. The proposed method analyzed the RF signal to adjust the matched GH functions, accounting for frequency-dependent attenuation. This technique was initially validated *in vivo* via beef muscle tissue. Our hypothesis was that tissue attenuation could be addressed by using an adaptive K-means clustering algorithm, and the GH kernels could be adjusted via a calculated scaler to improve H-scan US image quality over the entire depth. Thus, this research may increase the ability of tissue characterization using H-scan US imaging and its clinical potential for imaging complex tissue structures and deep organs.

We extended the results from Chapter 3 in Chapter 4 by developing a 2D sparse array H-scan US imaging system and a method for voxel-level classification of US scattering. The overarching purpose was to study and evaluate the sensitivity of the sparse H-scan volumetric US imaging technique to scatterer objects and to compare with B-scan US findings. We investigated the feasibility of using US imaging to detect relative changes in scatterer size for a series of homogeneous phantom materials in experimentation. We hypothesized that 3D sparse array H-scan US imaging is more sensitive to variations in scatterer size than the traditional B-scan US approach. Then ML methodologies were introduced to make the scatterer size estimation in real-time possible. Overall, the hypothesis was that the proposed imaging technology could increase

the ability of US for scatterer size estimation, and the data throughout the selected volume space could highlight the heterogenous microenvironment to make size estimation at different sub-regions possible.

In Chapter 5, we designed a high-resolution 3D H-scan US imaging technique to distinguish subtle changes at the cellular level and evaluate its use for monitoring tumor apoptotic activity and acute response to neoadjuvant chemotherapy. Inspection of the segmented H-scan US volumes reveals subtle spatial heterogeneity around the tumor periphery. While no differences in image intensity were found at baseline ($p > 0.99$), H-scan US volumes revealed a progressive blue color (hue) shift for tumors undergoing chemotherapy, while the control group appears unchanged over the same time interval. A one-way ANOVA analysis found a statistically significant change in H-scan US image intensity for the low-dose and high-dose cisplatin-treated mice ($p = 0.04$ and $p = 0.03$, respectively) but not for the control group ($p = 0.92$). Compared to baseline measurements, there were $51.2 \pm 5.1\%$ and $68.4 \pm 2.6\%$ increases in H-scan US image intensity at day 10 for the low and high-dose treated groups, respectively. The image homogeneity analysis indicated a decrease associated with H-scan US image intensity. Analysis of image homogeneity found no significant differences in the control group by day 10 ($-0.63 \pm 0.36\%$; $p = 0.24$). However, animals administrated with low-dose ($-1.53 \pm 0.36\%$; $p < 0.01$) or high-dose cisplatin ($-2.51 \pm 0.22\%$; $p < 0.01$) showed significantly lower levels of homogeneity when compared to control tumors. Furthermore, an inspection of MRI images revealed a progressive increase in the average ADC value when mice were undergoing therapy. Specifically, when compared to the mean ADC value of the control group on day 10, changes were significantly higher in the low-dose cisplatin group (i.e., $-2.57 \pm 4.02\%$ versus $37.74 \pm 15.66\%$, $p < 0.01$). Additionally, the average

ADC value of the high-dose cisplatin-treatment group was significantly higher ($73.47 \pm 2.95\%$; $p < 0.001$) than that of the other two groups caused by progressive water accumulation due to apoptosis. After US imaging on day 10, animals were humanely euthanized, and tumor tissue was excised for histological processing. Reported as an entire tissue cross-section, proliferation activity was $79.3 \pm 0.8\%$ for the control group while for the low-and high-dose cisplatin-treated groups was found to be $51.5 \pm 2.6\%$ and $40.3 \pm 4.5\%$, respectively ($p < 0.01$). Using a similar metric, apoptotic activity was $20.7 \pm 0.9\%$, $48.5 \pm 2.6\%$ and $59.7 \pm 4.5\%$ for the control, low-and high-dose treatment groups, respectively ($p < 0.001$). Lastly, versus the calculated nuclei size in the control group, $17.6 \pm 6.5 \mu\text{m}$, mice administered with cisplatin had tumor tissue with significantly smaller nuclear sizes at 14.1 ± 4.5 and $8.9 \pm 8.8 \mu\text{m}$, respectively ($p < 0.02$). Overall, the *in vivo* volumetric H-scan US imaging technique was introduced and shown to be a promising methodology for monitoring acute tumor response to anticancer drug treatment in TNBC. Analysis of the H-scan US results indicated no significant difference at baseline ($p = 0.92$), whereas the apoptosis-inducing drug-treated tumors exhibited a progressive increase in signal intensity within days of treatment initiation (up to 49.4% by day 3). Validated by three independent studies (i.e., image homogeneity, DW-MRI and histological measures), the findings of this study provided preclinical insight into US scattering properties of TNBC after chemotherapy and have potential implications for patient care by translating this technique to clinic.

6.2 Future Work

The analysis of our simulated US in Chapter 2 suggested that the image resolution along the depth axis is high, whereas the lateral resolution is low. A more advantaged technique is needed to improve the image resolution. Additionally, a random distribution of the acoustic scatterers was

modeled in this study to represent the tissue microstructure; the results presented here are more representative of the *in vivo* tumor microenvironment. Even though there was a subtle intergroup difference among different imaging apodization techniques, an improvement in image SNR was found when imaging homogenous phantom materials. To obtain more reliable analysis results to represent human tissue and to evaluate the impact of imaging apodization on H-scan US, a more complicated phantom model will be designed for a future study to improve the robustness of the analysis.

The imaging of complex tissue structure, such as tumors, was not included in Chapter 3. Since analyzing RF signals reflected from complex tissue needs a large ROI window size or small ROI with more signal overlap to achieve high computational accuracy, this can increase the computational costs and reduce the efficiency of the adaptive attenuation correction algorithm. Hence, future work needs to focus on the improvement of the attenuation correction method (i.e., code excitation) to address the signal attenuation involved with imaging of deep complex tissue structures *in vivo*. This would further help to reduce the impact of other factors on color shift, such as the concentration of cells.

One limitation of the proposed technique in Chapter 5 is that it cannot quantitatively measure the acoustic scatterer (nuclear) size *in vivo*, which is one of the essential ways to evaluate the effect of chemotherapy agents on cancer cells [1]–[3]. The limitation was mainly due to the lack of matched histological data. It can introduce bias when studying correlations between imaging and histological data due to the significant mismatch between the imaging scan planes and the surgical sample [4], [5]. The ability to link microscopy data to tissue properties through spatial correspondence can be critical for validating H-scan US imaging techniques. Therefore, future

works (e.g., attenuation correction techniques) are planned to improve the ability of H-scan US imaging for tissue characterization when imaging complex tissues in a clinical setting.

6.3 References

- [1] M. C. Kolios, G. J. Czarnota, M. Lee, J. W. Hunt, and M. D. Sherar, “Ultrasonic spectral parameter characterization of apoptosis,” *Ultrasound Med. Biol.*, vol. 28, no. 5, pp. 589–597, May 2002.
- [2] A. G. Liddane, C. A. McNamara, M. C. Campbell, I. Mercier, and J. M. Holaska, “Defects in Emerin-nucleoskeleton binding disrupt nuclear structure and promote breast cancer cell motility and metastasis,” *Mol. Cancer Res. MCR*, vol. 19, no. 7, pp. 1196–1207, Jul. 2021.
- [3] F. T. D’Astous and F. S. Foster, “Frequency dependence of ultrasound attenuation and backscatter in breast tissue,” *Ultrasound Med. Biol.*, vol. 12, no. 10, pp. 795–808, Oct. 1986
- [4] M. Zhang *et al.*, “Quantitative characterization of viscoelastic properties of human prostate correlated with histology,” *Ultrasound Med. Biol.*, vol. 34, no. 7, pp. 1033–1042, 2008.
- [5] D. Baldi, M. Aiello, A. Duggento, M. Salvatore, and C. Cavaliere, “MR Imaging-Histology Correlation by Tailored 3D-Printed Slicer in Oncological Assessment,” *Contrast Media X26 Mol. Imaging*, vol. 2019, p. e1071453, May 2019.

BIOGRAPHICAL SKETCH

Haowei Tai was born in a small village in Linfen, China. He attended the North University of China (NUC), China where he majored in software engineering. During his undergraduate studies, he practiced programming skills by developing software projects in university-affiliated companies. Then he was invited to join the graduate program without taking the qualifying exam. He graduated with a BS in 2014 and continued his master's program in the Laboratory of Computational Intelligence and Information Processing to design sparse computed tomography (CT) reconstruction techniques to reduce radiation exposure. Then he started to learn more about medical imaging techniques and eventually decided to pursue research in developing imaging techniques to help cancer diagnosis and treatment. He started his PhD in 2017 and focused mainly on developing a robust ultrasound technique to monitor cancer response to neoadjuvant therapy early stage. Based on the success of his projects and the potential impact on cancer treatment strategy, he received the UTD dissertation research award (2021). He also received the IEEE International Ultrasonics Symposium (IUS) and Biomedical Engineering Society (BMES) travel awards to present his research to other researchers in the field.

CURRICULUM VITAE

HAOWEI TAI

Department of Electrical and Computer Engineering, 800 W. Campbell Road, BSB 13.915,
Richardson, TX, 75080
Haowei.Tai@utdallas.com

EDUCATION

Department of Electrical and Computer Engineering, University of Texas at Dallas, TX, US

- *PhD of Engineering* in Electrical Engineering (12/2017-)
- **Dissertation title:** *Tissue characterization using H-scan ultrasound imaging*

School of Computer and Control Engineering, North University of China, Taiyuan, China

- *Master of Science* in Computer Science and Technology (09/2014-07/2017)
- **Dissertation title:** *System matrix modeling methods in CT iterative image reconstruction algorithm and their comparison in total variation (TV)*

School of Software Engineering, North University of China, Taiyuan, China

- *Bachelor of Engineering* in Software Engineering (09/2010-06/2014)

JOURNAL PUBLICATION

- **Tai, H.**, Khairalseed, M. & Hoyt, K. Adaptive attenuation correction during H-scan ultrasound imaging using K-means clustering. *Ultrasonics* 102, 105987 (2020).
- **Tai, H.**, Khairalseed, M. & Hoyt, K. 3-D H-Scan Ultrasound Imaging and Use of a Convolutional Neural Network for Scatterer Size Estimation. *Ultrasound in Medicine & Biology* 46, 2810–2818 (2020).
- **Tai H.**, Song J, Li J, et al. Three-Dimensional H-Scan Ultrasound Imaging of Early Breast Cancer Response to Neoadjuvant Therapy in a Murine Model. *Investigative Radiology*. 2021 Oct 12.
- **Tai, H.**, Margolis, R., Li, J., Hoyt, K. H-scan ultrasound monitoring of breast cancer response to chemotherapy and validation with diffusion-weighted magnetic resonance imaging. *Journal of Ultrasound in Medicine* (accepted)
- Basavarajappa, L. Beak, J., Reddy, S., Song, J., **Tai, H.**, Rijal, G., Parker, K., Hoyt, K. Multiparametric ultrasound imaging for the assessment of normal versus steatotic livers. *Scientific Reports* 11, 2655 (2021).

- Baek J, Poul SS, Basavarajappa, L., Reddy, S., **Tai, H.**, Hoyt, K., Parker, KJ. Clusters of ultrasound scattering parameters for the classification of steatotic and normal livers. *Ultrasound in Medicine & Biology*. 2021 Oct 1;47(10):3014-27.
- **Tai, H.**, Basavarajappa, L., Hoyt K. Three-Dimensional Voxel-level Tissue Classification of Ultrasound Scattering using a Sparse Matrix Array Transducer. *Computers in biology and medicine* (under review)
- Qiao, Z., **Tai, H.**, Song, W. & Li, X. Investigation of Unmatched Projector/Backprojector Pairs in Adaptive-Steepest-Descent-Projection-Onto-Convex-Sets Algorithm. *Journal of Medical Imaging and Health Informatics* 7, 630–635 (2017).

CONFERENCE PUBLICATION

- **Tai, H.**, Khairalseed, M., Hoyt, K. 3D H-scan ultrasound imaging system and method for acoustic scatterer size estimation: Preliminary studies using phantom materials. 2019 IEEE International Ultrasonics Symposium (IUS) 1515–1518 (2019).
- **Tai, H.**, Dolui, S., Khairalseed, M., Hoyt, K. Three-Dimensional Voxel-Level Classification of Ultrasound Scattering. 2020 IEEE 17th International Symposium on Biomedical Imaging (ISBI) 1838–1841 (2020).
- **Tai, H.**, Reddy, S., Song, J., Khairalseed, M. Hoyt, K. Abstract PS3-28: Three-dimensional H- scan ultrasound imaging for acute detection of breast cancer response to neoadjuvant treatment - Initial results using a preclinical animal model. *Cancer Res.* 81, PS3-PS3-28 (2021).
- **Tai, H.**, Basavarajappa, L., Khairalseed, M., Hoyt, K. 3-D Voxel-level Tissue Classification of Ultrasound Scattering using a Sparse Matrix Array Transducer. 2021 IEEE International Ultrasonics Symposium (IUS) 1–4 (2021).
- **Tai, H.**, Khairalseed, M., Song, J., Reddy, S., Li, J., Hoyt, K. Assessing Early Breast Cancer Response to Chemotherapy Using 3-D H-scan Ultrasound Images and Texture Analysis. 2021 IEEE International Ultrasonics Symposium (IUS) 1–4 (2021).
- Dolui, S., **Tai, H.**, Khairalseed, M. Hoyt, K. Ultrasound pulse shaping for improved H -scan imaging and tissue classification. 2020 IEEE International Ultrasonics Symposium (IUS) 1–4 (2020).
- Basavarajappa, L., **Tai, H.**, Hoyt, K. Early assessment of nonalcoholic fatty liver disease using multiparametric ultrasound imaging. 2020 IEEE International Ultrasonics Symposium (IUS) 1–4 (2020).
- Dolui, S., Reddy, S., Pena, J., Song, J., **Tai, H.**, Campbell, Z., Hoyt, K. On the potential uses of ultrasound imaging for the detection of anesthesia-induced neuronal apoptosis in the developing brain. 2020 IEEE International Ultrasonics Symposium (IUS) 1–4 (2020).

CONFERENCE PRESENTATION

- **Tai, H.**, Khairalseed, M., Hoyt, K. Volumetric H-scan Ultrasound Imaging System and Method for Tissue Characterization. 2019 Biomedical Engineering Society (BMES)
- **Tai, H.**, Hoyt, K. 3D ultrasound system for classification of acoustic scatterers using a 1024-element matrix array transducer. 2020 178th Acoustical Society of America (ASA)
- **Tai, H.**, Song, J., Reddy, S., Li, J., Khairalseed, M., Hoyt, K. 3D H-scan ultrasound imaging of cancer cell death during response to drug treatment. 2021 World Molecular Imaging Society (WMIC)
- **Tai, H.**, Margolis, R., Li, J., Trinh, B., Song, J., Hoyt, K., Comparison of H-scan ultrasound and diffusion-weighted magnetic resonance imaging of head and neck cancer undergoing neoadjuvant chemotherapy. 2022 American Association for Cancer Research (AACR)
- **Tai, H.**, Margolis, R., Li, J., Hoyt, K., 3-D H-scan ultrasound imaging of relative scatterer size using a matrix array transducer – Preliminary *in vitro* and *in vivo* results. 2022 American Institute of Ultrasound in Medicine (AIUM)
- **Tai, H.**, Margolis, R., Trinh, B., Li, J., Hoyt, K., Monitoring breast cancer response to chemotherapy using H-scan ultrasound imaging and radiomics analysis. 2022 Gordon Research Conference (GRC)

EMPLOYMENT

Teaching Assistant, Department of Biomedical Engineering, University of Texas at Dallas
09/2017-03/2018

Research Assistant, Department of Biomedical Engineering, University of Texas at Dallas
09/2018-

HONOR & AWARD

UTD Dissertation Research Awards	2021
IEEE IUS Travel Award	2020
BMES Travel Award	2019
First-class Scholarship for Overall Performance	2016
First-class Scholarship for Academic Performance	2015
Lei Kesheng Scholarship (1/1000)	2014
Excellent Student Cadre of Shanxi Province (2/1000)	2014
Excellent Student Cadre of North University of China	2013
National Endeavor Fellowship	2011